Alma Mater Studiorum · Università di Bologna

Scuola di Scienze
Dipartimento di Fisica e Astronomia
Corso di Laurea in Astrofisica e Cosmologia

Shapes and density profiles of haloes in self-interacting dark matter cosmologies

Relatori:
Prof. Lauro Moscardini
Dott. Giulia Despali
Priv.-Doz.Dr. Matteo Maturi

Presentata da:
Claudio Mastromarino

Anno Accademico 2020/2021

Abstract

Self-interacting dark matter models (SIDM) have become attractive alternatives to the collisionless cold dark matter model (CDM) since they can alleviate tensions between the results of CDM-only simulations and observations (small scale crisis of CDM). The majority of prior research on these DM models has relied on SIDM-only simulations, ignoring the interplay of self-interactions and baryonic physics. However, even these results may not be adequate for making comparisons with observations. As in the CDM paradigm, baryons can have a strong impact on the distribution of SIDM. Therefore it becomes crucial to understand the role of baryonic physics on the halo properties also in these models.

In this thesis work, we use cosmological simulation to test the differences of halo properties on the mass range that goes from Milky-Way-like ($M = 10^{12}\,M_{\odot}/h$) to massive elliptical galaxies ($M = 10^{13.5}\,M_{\odot}/h$) in CDM and SIDM models. We use two distinct SIDM models, one with constant cross section ($\sigma/m_{\chi} = 1\,cm^2/g$) and one with a velocity-dependent cross section. The simulation set is made of 6 runs in total, which simulate the same volume of 50 Mpc^3, in CDM and the two SIDM models; moreover, for each of those a DM-only and a full-hydrodynamic version is available, allowing us to study the effect of baryons and alternative dark matter models at the same time. In particular, we focus on the analysis of density profiles and halo shapes at $z = 0$. We split our sample into three mass bins in order to compare and average the features of haloes of comparable mass.

From DM-only simulations we find: 1) both SIDM models produce a central core in density profiles regardless of the halo mass; 2) both SIDM models make DM haloes rounder than in CDM counterpart for each mass bin.

From full-hydrodynamic simulations, we find that the inclusion of baryonic effects can modify these properties. Both for the density profiles and the halo shapes the baryon effects make the differences between the DM models less pronounced than in the DM-only case. Moreover, we find that the average final properties of the density profiles in full-hydrodynamic simulations depend on the considered mass bin: the most massive shows a cored profile in the SIDM runs, while the less massive one shows a cuspier profile than in CDM. For the intermediate-mass bin we find no differences in the density profile between the models.

Regarding the halo shapes we find that the haloes in the SIDM models are more spherical than in the CDM counterpart also with the inclusion of the baryonic effects. However, while the differences between DM models in the density profiles are visible only at small radii ($r < 10\,kpc/h$), we show that SIDM haloes remain more spherical than in CDM even in more external regions ($r \sim 60 - 100\,kpc/h$).

Abstract

I modelli di self-interacting dark matter (SIDM) sono diventati una interessante alternativa al modello di cold dark matter (CDM) dato che possono attenuare le tensioni tra le predizioni da simulazioni in CDM-only e le osservazioni (small scale crisis of CDM). La maggior parte delle analisi su questi modelli di DM si sono basate su risultati provenienti da simulazioni in SIDM-only, dunque trascurando gli effetti dovuti alla presenza dei barioni. Tuttavia, anche tali risultati potrebbero non essere adeguati nel momento in cui bisogna confrontare le predizioni con le osservazioni. Infatti, come per il modello di CDM, i barioni possono avere un forte impatto sulla distribuzione delle particelle di SIDM. Per questo motivo è fondamentale capire il ruolo della fisica barionica sulle proprietà degli aloni, anche per questi modelli.
In questo progetto di tesi, utilizzando simulazioni cosmologiche abbiamo testato quali sono le principali differenze per le proprietà di aloni nei modelli di cold dark matter (CDM) e self-interacting dark matter (SIDM). Abbiamo selezionato aloni con massa compresa tra $M = 10^{12}\, M_{\odot}/h$ e $M = 10^{13.5}\, M_{\odot}/h$. Abbiamo usato due modelli differenti di SIDM, il primo con sezione d'urto costante ($\sigma/m_{\chi} = 1\, cm^2/g$), il secondo con sezione d'urto dipendendte dalla velocità relativa delle particelle di DM. Abbiamo in totale un set di 6 simulazioni che simulano lo stesso volume di 50 Mpc^3 in CDM e nei due modelli di SIDM. Per ognuno di questi modelli abbiamo a disposizione sia le simulazioni in DM-only sia la versione full-hydrodynamic, in modo tale da poter studiare simultaneamente gli effetti barionici ed i diversi modelli di DM. Nello specifico ci concentriamo sulla analisi dei profili di densità e sulle forme degli aloni a $z = 0$. Abbiamo diviso gli aloni selezionati in 3 bin di massa così da confrontare e mediare le caratteristiche di aloni con massa simile.
Dall'analisi di aloni nelle simulazioni DM-only, troviamo: 1) entrambi i modelli di SIDM producono un core centrale nei profili di densità indipendentemente dalla massa; 2) gli aloni nei modelli di SIDM sono più sferici che nel caso degli aloni in CDM.
Dallo studio degli aloni nelle simulazioni full-hydrodynamic mostriamo che l'inclusione dei barioni può modificare le proprietà sopra descritte. Sia per i profili di densità che per le forme degli aloni troviamo che gli effetti barionici rendono le differenze tra i diversi modelli di DM meno pronunciate rispetto a quanto trovato nel caso DM-only. Inoltre troviamo che le proprietà finali dei profili di densità nelle simulazioni full-hydrodynamic dipendono dal bin di massa considerato: il bin più massivo presenta densità più basse nelle parti centrali nei casi dei modelli SIDM rispetto al profilo in CDM, mentre per il bin a massa più bassa troviamo che i profili in SIDM hanno densità più elevata del profilo in CDM. Nel caso del bin di massa intermedio non troviamo differenze tra i modelli di DM.
Per quanto riguarda le forme degli aloni troviamo che anche con l'inclusione dei barioni,

gli aloni nei modelli SIDM sono più sferici rispetto alle controparti in CDM. Inoltre, mentre le differenze tra i modelli di DM nei profili di densità diventano visibili solo a piccoli raggi ($r < 10\,kpc/h$), gli aloni nei modelli di SIDM rimangono più sferici che nel caso in CDM anche per raggi più elevati ($r \sim 60 - 100\,kpc/h$).

Contents

Introduction

The dominant hypothesis for the formation and evolution of cosmic structure in our Universe is the Λ cold dark matter (Λ**CDM**) model, in which dark matter (DM) is thought to be non-relativistic and collisionless. It explains several fundamental features of galaxy formation and evolution (Frenk et al. 2012; Vogelsberger et al. 2014) and it predicts the spectrum of matter fluctuations in the early Universe with exceptional accuracy (Aghanim et al. 2020). However, the absence of experimental evidence of collisionless cold dark matter particles (Arcadi et al. 2018) and the fact that N-body simulations based on CDM models present some discrepancies with observed quantities (small-scale crisis of CDM) has led to interest in alternative DM models. Small-scale issues like as missing satellites (Klypin et al. 1999), core-cusp (Moore 1994), diversity (Oman et al. 2015) and Too-Big-To Fail (Boylan-Kolchin et al. 2011) problems seem to be troubling for the CDM paradigm. These inconsistencies in part come from comparing data to DM-only simulations, which neglect baryonic effects. As a result, several studies have been performed to determine if these discrepancies are due to an incomplete modelling of baryonic physics with the CDM paradigm. However, it is still uncertain if accurately including relevant astrophysical processes will be sufficient to bring the simulated CDM model completely in agreement with observations.
Another potential option is that these discrepancies tell us something about the nature of DM and it is the CDM model that needs to be revisited. The first possibility is that the DM is not cold, but it is warm, meaning that the DM particles are quasi-relativistic during kinetic decoupling (*Warm Dark Matter* models). The WDM models predict a damped linear power spectrum due to free-streaming leading to a reduction in the number of substructures and the formation of less concentrated haloes when compared to CDM. These properties suggest that WDM can provide a solution to two of the four main issues related to the CDM paradigm, respectively the missing satellites problem and the too-big-to-fail problem (Li et al. 2017; Diamanti et al. 2017). However, it has been shown that an unrealistic low value of the WDM mass is needed to create core sizes that match observations (Carucci et al. 2015) and solve the Core/Cusp problem.
Another of the proposed alternatives, first introduced by Spergel and Steinhardt (2000a), is that DM is not collisionless, but that the DM particles can scatter with each other. These are *Self-interacting dark matter* models. N-body simulations and analytical consid-

erations show that DM self-interactions can have an impact on the macroscopic characteristics of haloes, alleviating some of the issues that emerge in a collisionless CDM scenario, while leaving the properties on large scale unchanged. In particular, self-interactions can flatten the centrally peaked cusps in the inner regions of galaxies and can disturb the growth of dense satellite galaxies predicted by simulations, that are at the base of the core-cusp and Too-big-to-fail issues (Vogelsberger et al. 2012; Elbert et al. 2015b).
In general, it is possible to divide the SIDM models into two large families: constant cross-section where the probability of scattering is constant on all scales and depends only on the DM density and the velocity dependent cross-section where the probability of scattering depends, not only on the density, but also on the relative velocity of the DM particles. Moreover, the properties of each SIDM model depend on the strength of the self-interaction cross-section. Studies of the predicted SIDM effects in comparison to observations set constraints on the ratio of the dark matter self-interaction cross section to the dark matter mass: σ/m. The current constraints come from studies on different scales: to explain the distribution of DM in dwarf galaxies SIDM requires a cross-section $\sigma/m > 0.5\, cm^2 g/$ (Elbert et al. 2015a), from the ellipticity of the elliptical galaxies it was deduced that $\sigma/m \leq 1\, cm^2/g$ (Peter et al. 2013) while from strong lensing arc statistics in galaxy clusters the allowed cross-section should be $\sigma/m < 0.1\, cm^2/g$ (Meneghetti et al. 2001). Given these disparities on different scales, a cross-section compatible with cluster scale limitations is unable to appreciably lower the centeral density of dwarf galaxies (Fry et al. 2015). As a result, there has been a surge in interest in SIDM models with velocity-dependent cross-sections, i.e a cross-section that decreases with increasing relative velocity. The cross section on dwarf galaxies scale can be several orders of magnitude bigger than on cluster sizes, bringing in agreement constraints on different scales.
It is worth mentioning that the majority of prior research has relied on DM-only simulations, ignoring the interplay of self-interactions and baryonic physics. Sameie et al. (2018a) and Elbert et al. (2018) used simulations of isolated galaxies and showed that the cross talk between DM particles interactions and baryons produces a wide range of halo profiles, depending on how centrally concentrated the baryonic component is. Recently, Despali et al. (2019) studied the baryonic effects not in an isolated and idealized scenario, but in full-hydrodynamic zoom-in simulations. Focusing on zoomed simulations of 9 haloes in the mass range that goes from Milky-Way-like to massive elliptical galaxies, they showed that the combination of DM self-interaction and baryonic physics leads to a complicated evolution of halo properties, dependent on halo mass, morphological type, as well as the halo mass accretion history. These results show that as in the CDM paradigm, baryons can have a strong impact on the distribution of SIDM. Therefore it becomes crucial to understand the role of baryonic physics on the halo properties also in SIDM models.
In this thesis work, using full-hydrodynamic simulations we want to test what are the main differences between the CDM model and the SIDM models and how the baryonic

effects can have an impact on the properties of the simulated haloes. We use two distinct SIDM models, one with constant cross section ($\sigma/m_\chi = 1\, cm^2 g^{-1}$) and one with a velocity-dependent cross section. The simulation set is made of 6 runs in total, which simulate the same volume of 50 Mpc^3, in CDM and the two SIDM models; moreover, for each of those a DM-only and a full-hydrodynamic version is available, allowing us to study the effect of baryons and alternative dark matter at the same time. The simulations have been run with the cosmological parameters taken from the most recent Planck results (Aghanim et al. 2020) using the Gadget3 code and are part of the extended family of EAGLE simulations. In these simulations there are $N = 752^3$ DM particles and initially there is an equal number of baryonic particles. The dark matter mass resolution is $m_{DM} = 9.70 \cdot 10^6 M_\odot$, while the baryonic resolution is $m_g = 1.81 \cdot 10^6 M_\odot$.
We select haloes with masses M_{200} in the range between $10^{12}\, M_\odot h^{-1}$ and $10^{14}\, M_\odot h^{-1}$ at $z = 0$, for all 6 models available. However, given the volume of the boxes, we do not find haloes with mass $M_{200} > 10^{13.5}\, M_\odot h^{-1}$. The mass range is chosen to test and extend the results obtained by Sameie et al. (2018a) and Despali et al. (2019), not in isolated or zoom-in simulations of individual galaxies, but using a full cosmological box.
This thesis work is organised as follows:

- Chapter 1 provides the cosmological framework on which this thesis work is based, introducing the fundamental equations to describe the dynamics of the Universe and how to use them to build a cosmological model.

- Chapter 2 deals with the theory of structure formation and evolution in our Universe.

- Chapter 3: we introduce dark matter and its role in structure formation and evolution. We discuss the standard cosmological model (Λ**CDM**) and its main evidences.

- Chapter 4: we discuss in detail the main problems related to the CDM model, we introduce Self-Interacting Dark Matter models and their implementation in the Gadget3 code.

- Chapter 5: we present the key features of the simulations used in this work and we analyze the density profiles of the selected haloes using both DM-only and full-hydrodynamic simulation.

- Chapter 6: we analyze the halo shape properties for the considered DM models.

- Chapter 7 summarises the main results of this thesis project.

Chapter 1

Cosmological Models

In this Chapter we will present the cosmological framework on which this thesis work is based. We will present the fundamental equations describing the dynamics of the Universe and how to use them to build a cosmological model. In the last paragraphs we will define the scales useful for describing the process of structure formation. A more complete treatment can be found in *"Cosmology: The origin and evolution of cosmic structure"* (Coles et al. 2003).

1.1 Cosmological Principle

Cosmology is that branch of Physics that studies the Universe as a whole system using observational, physical and mathematical instruments to understand its origin and evolution in order to build a model that is descriptive, but above all predictive. One of the fundamental ingredients on which the large majority of the current models are based is the **Cosmological Principle** (CP) which states that the Universe is *isotropic* and *homogeneous* on large scale (larger than hundreds of Mpc). Isotropy implies that there are no differences when looking at the Universe in different directions, i.e. there are no privileged directions. Homogeneity implies that all observers, in any part of the Universe, will observe, on average, the same properties and the same matter distribution, that is, there are no privileged positions. A corollary to the cosmological principle is that the laws of physics are universal. The same physical laws and models that apply here on the Earth also work in all parts of the Universe and physical constants (such as the gravitational constant, mass of the electron, speed of light) do not change their values in space and time. The clearest modern observational evidence of this principle is the measurement of the cosmic microwave background (CMB) : a "thermal bath of photons" coming from the early universe, observable from any direction. It has been shown that the photons of this radiation, on large scale, have the same average temperature in every part of the Universe and this means that in any direction, for any observer, the same

average results are obtained (Aghanim et al. 2020).

1.2 Friedmann-Lemaître-Robertson-Walker metric

On large scales, the dominant force in the Universe is the gravitational force, that we assume to be described by Einstein's theory of General Relativity, in this way the geometric properties of space-time are related to the energy-matter content, that for the CP, we assume homogeneous and isotropic.
To study the dynamics of such a Universe, we need to find a suitable metric (distance between two events in space-time). Using Einstein's convention, we can define a general metric such as:

$$ds^2 = g_{\alpha\beta} dx^\alpha dx^\beta \,, \tag{1.1}$$

which in its explicit form reads:

$$ds^2 = g_{00} dt^2 + 2 g_{i0} dt dx^i + g_{ij} dx^i dx^j \,, \tag{1.2}$$

where $g_{\alpha\beta}$ is the metric tensor that describes the geometry of space-time, in our convention $g_{\alpha\beta} = diag(+1, -1, -1, -1)$. The metric can be simplified given two assumptions: the isotropy implies that the mixed terms of the tensor are null ($g_{i0} = 0$) and photons must follow null geodesics ($ds^2 = 0$ and $v = c$). Considering these assumptions the metric becomes:

$$ds^2 = c^2 dt^2 + g_{ij} dx^i dx^j = c^2 dt^2 - dl^2 \,, \tag{1.3}$$

where $dl^2 = g_{ij} dx^i dx^j$ describes the spatial metric part.
Considering a two-dimensional Universe, there are only 3 types of two-dimensional surfaces, i.e. 3 possible cases for the curvature :

1. **Cartesian plane** : Infinite curvature
   Using polar coordinates $[\rho, \varphi]$ the spatial metric part becomes:

   $$dl^2 = d\rho^2 + \rho^2 d\varphi^2 \,, \tag{1.4}$$

   defining $\rho = ar$, where r is a dimensionless parameter and a has the dimensions of a length (in general it is a time function $a(t)$), we can write the flat spatial metric:

   $$dl^2 = a^2 (dr^2 + r^2 d\varphi^2) \,. \tag{1.5}$$

2. **Spherical surface** : Positive curvature
   Using spherical coordinates $[R, \theta, \varphi]$, with R radius of the sphere :

   $$dl^2 = R^2 (\sin^2\theta \, d\varphi^2 + d\theta^2) \,, \tag{1.6}$$

   setting $R = a$, $\sin\theta = r$, we get the close spatial metric :

   $$dl^2 = a^2 \left[r^2 d\varphi^2 + \frac{dr^2}{1 - r^2} \right] . \tag{1.7}$$

3. **Hyperbolic surface** : Negative curvature
   Considering the equation (1.6), we can replace sin → sinh, getting :

$$dl^2 = R^2(\sinh^2\theta\, d\varphi^2 + d\theta^2)\,, \tag{1.8}$$

   setting $R = a$, $\sinh\theta = r$ and remembering that $\cosh^2\theta = 1 + \sinh^2\theta$, the open spatial metric becomes:

$$dl^2 = a^2\left[r^2 d\varphi^2 + \frac{dr^2}{1+r^2}\right]. \tag{1.9}$$

Looking at the equations (1.5),(1.7),(1.9), we note that it is possible to define the three geometries in a general form :

$$dl^2 = a^2\left[\frac{dr^2}{1-kr^2} + r^2 d\varphi^2\right], \tag{1.10}$$

where k, called *Curvature Parameter*, can take only 3 integer values, one for each geometry:

$$\begin{cases} k = 0 & \textit{Flat} \\ k = +1 & \textit{Closed} \\ k = -1 & \textit{Open} \end{cases} \tag{1.11}$$

Following the same steps, but in a three-dimensional Universe, adding the time metric part and and reinserting the time dependence of a, we get:

$$ds^2 = c^2dt^2 - a(t)^2\left[\frac{dr^2}{1-kr^2} + r^2(d\theta^2 + \sin^2\theta d\varphi^2)\right], \tag{1.12}$$

that defines the **Friedmann-Lemaître-Robertson-Walker metric** (FLRW metric). This is the best metric for studying an isotropic and homogeneous Universe, in which photons move at a fixed speed c. Moreover, using this metric, one can study the Universe without assuming a priori any geometry, since it is able to describe all of them.
The term $a(t)$, called *cosmic scale factor*, is a parameter that changes the scale of the spatial part, without changing the geometry, while it is the parameter k, dimensionless and discrete, that defines the geometry.
Related to the scale factor, we can define the Hubble parameter:

$$H(t) \doteq \frac{\dot{a}}{a}\,, \tag{1.13}$$

from which the **Hubble-Lemaître law** can be made explicit:

$$v_R = H d_{PR} \tag{1.14}$$

and states that there is a speed of recession in the radial direction (v_R) which is proportional to the distance (d_{PR}) and the Hubble parameter quantifies this proportionality. The Hubble constant, i.e. the current value of the Hubble parameter, is defined as

$$H_0 \doteq \frac{\dot{a_0}}{a_0}\,. \tag{1.15}$$

Because of the troubled history of the measurement of the value of this constant, it has become customary to express it in units of 100 $km/s\ Mpc^{-1}$. Present measurements (Aghanim et al. 2020) give:

$$h_0 = \frac{H_0}{100\ km/s\ Mpc^{-1}} = 0.6777 \pm 0.0770\,, \tag{1.16}$$

where h_0 measures the uncertainty with which the value of the Hubble constant is known. Through this constant we can fix the corresponding length and time scales :

$$l_{H_0} = \frac{c}{H_0} = 3000\, h_0^{-1}\, Mpc\,, \tag{1.17}$$

$$t_{H_0} = \frac{1}{H_0} = 9.8\, h_0^{-1}\, Gyr\,, \tag{1.18}$$

where t_{H_0} defines the age that the Universe would have if it had expanded linearly [1].

1.3 Friedmann Equations

Friedmann's cosmological models are based on 3 hypotheses:

- Cosmological Principle
- General Relativity applies
- Universe as a Perfect Fluid

In these hypotheses we can write the field equation:

$$R_{\mu\nu} - \frac{1}{2} g_{\mu\nu} R \;=\; \frac{8\pi G}{c^4} T_{\mu\nu}\,. \tag{1.19}$$

This equation (**Einstein's equation**) asserts that the space-time geometry of the Universe, expressed by the right-hand member, is determined by its mass-energetic content, represented by the energy-momentum tensor $T_{\mu\nu}$. $R_{\mu\nu}$ is the Ricci tensor, while R is the scalar of curvature. In general the $T_{\mu\nu}$ components physically mean the following: T^{00}

[1] This value is too low and is in tension with current age measurements of older globular clusters.

is the energy density; T^{0j} is the energy flux across the spatial surface x_j = constant; T^{i0} is the density of $i-th$ component of momentum; T^{ij} is the $i-th$ component of momentum flux across the spatial-surface x_j = constant, where if $i = j$ the momentum causes normal stress on the fluid element (Pressure), while if $i \neq j$ it causes shear stress. Since we are considering a perfect fluid $T^{0j} = 0$ (there is no conduction) and $T^{ij} = 0$, with $i \neq j$ (there is no viscosity). The CP implies that spatial components must be equal, then the tensor $T_{\mu\nu}$ can be expressed exclusively using pressure and density. Using the four-velocity u_μ:

$$T_{\mu\nu} = -Pg_{\mu\nu} + (P + \rho c^2)u_\mu u_\nu \,. \tag{1.20}$$

The Einstein's equation actually represents 16 equations, one for each combination of the indices. To solve it one must assume a metric (1.12) since CP holds and express the energy-momentum tensor (1.20). Under these conditions, only 2 of the Einstein equations do not become identities and these are the so-called **Friedmann equations**:

$$\ddot{a} = -\frac{4}{3}\pi G\left(\rho + \frac{3P}{c^2}\right)a \,, \tag{1.21}$$

$$\dot{a}^2 + kc^2 = \frac{8}{3}\pi G\rho a^2 \,. \tag{1.22}$$

By solving these two equations we can build a cosmological model. They are differential equations that need a value for the curvature k and an equation of state $P = P(T, \rho)$ to be solved. By definition, the Universe is an adiabatic system, so we can use the adiabatic condition to link the two Friedmann equations:

$$dU = -PdV \;\longrightarrow\; d(\rho c^2 a^3) = -Pda^3 \,, \tag{1.23}$$

thus only two of the three equations are independent.

1.3.1 Friedmann equations with a cosmological constant

Before the discovery of the Hubble expansion, the Universe was thought to be a static system. Taking the equation (1.21), to have static solutions (i.e. $\ddot{a} = \dot{a} = 0$) we must have :

$$\rho = -\frac{3P}{c^2} \,, \tag{1.24}$$

which means that either the pressure or the density must be negative, while these quantities are positive definite. To solve this problem, Einstein thought of adding a term Λ, the so called **Cosmological Constant**, to the field equation:

$$R_{\mu\nu} - \frac{1}{2}g_{\mu\nu}R - \Lambda g_{\mu\nu} \;=\; \frac{8\pi G}{c^4}T_{\mu\nu} \,. \tag{1.25}$$

In this way the covariant character of the equation is maintained, and it is possible to derive a static solution. When Hubble discovered the expansion of the Universe, Einstein

judged the introduction of Λ as "one of the biggest error of his life". Nevertheless, in the standard cosmological model, this constant has been reintroduced to describe the accelerated expansion of the Universe, due to the presence of Dark Energy. With the equation (1.25), the Friedmann equations can be obtained in the same analytical form:

$$\ddot{a} = -\frac{4}{3}\pi G\left(\tilde{\rho} + \frac{3\tilde{P}}{c^2}\right)a\,, \tag{1.26}$$

$$\dot{a}^2 + kc^2 = \frac{8}{3}\pi G\tilde{\rho}a^2\,, \tag{1.27}$$

where

$$\tilde{P} = P - \frac{\Lambda c^4}{8\pi G}\,, \tag{1.28}$$

$$\tilde{\rho} = \rho + \frac{\Lambda c^2}{8\pi G}\,. \tag{1.29}$$

Thus the cosmological constant contributes negatively to pressure and positively to density, i.e. has the effect of a source of repulsive gravitational force.

1.4 Components of the Universe

One of the most important cosmological parameters is the so-called density parameter: a dimensionless parameter useful for describing the geometry of the universe. To define it, we take the Friedmann equation (1.22) and divide it by a_0 (today's value of the scale factor):

$$\left(\frac{\dot{a}}{a_0}\right)^2 - \frac{8}{3}\pi G\rho\left(\frac{a}{a_0}\right)^2 = -\frac{kc^2}{a_0^2}\,, \tag{1.30}$$

where we know that $H = \frac{\dot{a}}{a}$ and $H_0 = \frac{\dot{a}_0}{a}$, so we can define the **critical density of the Universe**:

$$\rho_c \doteq \frac{3H^2}{8\pi G}\,, \tag{1.31}$$

and its value today:

$$\rho_{0,c} = \frac{3H_0^2}{8\pi G} = 1.19\cdot 10^{-29}\,h_0^2 \quad g/cm^3\,. \tag{1.32}$$

This means that $8/3\pi G = H_0^2/\rho_{c,0}$, replacing this relation in (1.30) calculated for $t = t_0$, we obtain:

$$H_0^2\left(1 - \frac{\rho_0}{\rho_{0,c}}\right) = -\frac{kc^2}{a_0^2}\,. \tag{1.33}$$

In this way, the geometry of the Universe is defined by the value of the round bracket that allows us to define the density parameter:

$$\Omega \equiv \frac{\rho}{\rho_c}\,, \qquad\qquad \Omega_0 \equiv \frac{\rho_0}{\rho_{0,c}}\,, \tag{1.34}$$

then

$$\begin{cases} \Omega_0 = 1 \rightarrow \rho_0 = \rho_{c,0} & \textit{Flat} \\ \Omega_0 > 1 \rightarrow \rho_0 > \rho_{c,0} & \textit{Closed} \\ \Omega_0 < 1 \rightarrow \rho_0 < \rho_{c,0} & \textit{Open} \end{cases} \tag{1.35}$$

Therefore, to know the geometry of Universe we have to know the current density ρ_0 of all the Universe components and compare that value with $\rho_{c,0}$. If we consider all the components that make up the Universe, equation (1.33) become :

$$H_0^2(1 - \Omega_{0,tot}) = -\frac{kc^2}{a_0^2}\,, \tag{1.36}$$

where

$$\Omega_{0,tot} = \sum_{ith-comp} \Omega_{0,i} = \Omega_{0,M} + \Omega_{0,R} + \Omega_{0,\Lambda}\,. \tag{1.37}$$

The last equation defines the current total density parameter, which specifies the three components that make up the Universe in the current cosmological model: Non-Relativistic Matter (Baryons + Dark Matter), Radiation and Cosmological Constant. For each of these components we can specify an equation of state which in adiabatic conditions can be represented as $P \equiv P(\rho)$. We can write a general form of this equation that includes all the components:

$$P = W\rho c^2 \quad \text{with } W = \textit{constant}\,, \tag{1.38}$$

where

$$\begin{cases} W = 0 & \textit{Non-relativistic Matter} \\ W = 1/3 & \textit{Radiation and Relativistic Matter} \\ W = -1 & \textit{Cosmological Constant} \end{cases} \tag{1.39}$$

If we now consider the adiabatic equation and substitute equation (1.38):

$$d(\rho a^3) = -W\rho da^3 \quad \longrightarrow \quad \frac{d\rho}{\rho} = -\frac{da^3}{a^3}(1+W)\,, \tag{1.40}$$

and integrating from t_0 to t:

$$\rho = \rho_0 \left(\frac{a}{a_0}\right)^{-3(1+W)} = \rho_0(1+z)^{3(1+W)}\,, \tag{1.41}$$

where $z = a_0/a - 1$ defines the cosmological redshift. We can use the equation (1.41) to study the density trends as a function of time, for each component substituting the respective values of W:

1. Non-Relativistic Matter $\rho_M \propto a^{-3} \propto (z+1)^3$;
2. Radiation $\rho_R \propto a^{-4} \propto (z+1)^4$;
3. Cosmological Constant $\rho_\Lambda \propto a^0 = (z+1)^0 = const$.

Therefore the density evolution depends on the considered component, i.e. the value of W. Moreover, as shown in Fig. 1.1, if we plot these dependencies, we can define three different epochs looking at which component dominates the others. To simplify the Friedmann equations, we could consider only the component prevailing over the others, depending on the cosmic epoch we are studying. In this way we can define two

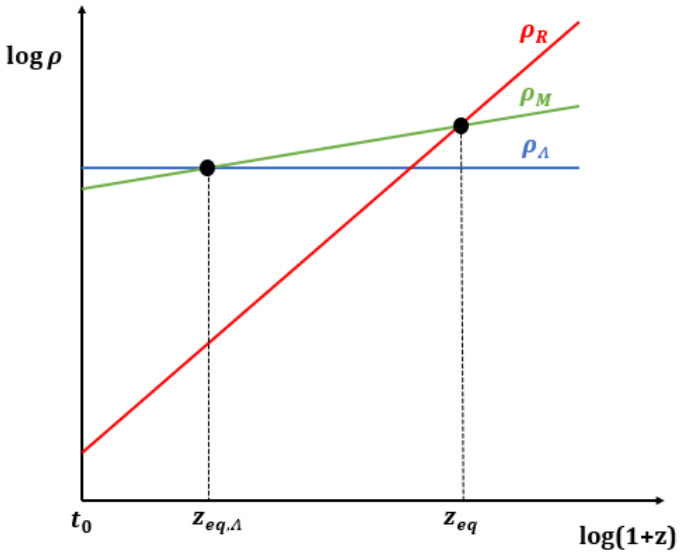

Figure 1.1: *Density of species in the Universe as a function of* $(1+z)$. *The dashed vertical lines indicate the two equivalence redshifts* $z_{eq,\Lambda}$ *and* z_{eq}.

equivalence redshifts at which the densities of two components cross:

1. **Matter-Radiation equality** z_{eq}

$$\rho_M(z_{eq}) = \rho_R(z_{eq}) \rightarrow \rho_{0,M}(1+z_{eq})^3 = \rho_{0,R}(1+z_{eq})^4$$

$$(1+z_{eq}) = \frac{\rho_{0,M}}{\rho_{0,R}} \quad \rightarrow \quad (1+z_{eq}) = \frac{\Omega_{0,M}}{\Omega_{0,R}} \, ; \tag{1.42}$$

2. **Matter-Cosmological Constant equality** $z_{eq,\Lambda}$

$$\rho_M(z_{eq,\Lambda}) = \rho_\Lambda(z_{eq,\Lambda}) \rightarrow \rho_{0,M}(1+z_{eq,\Lambda})^3 = \rho_{0,\Lambda}$$

$$(1+z_{eq,\Lambda}) = \left(\frac{\rho_{0,\Lambda}}{\rho_{0,M}}\right)^{1/3} \quad \rightarrow \quad (1+z_{eq,\Lambda}) = \left(\frac{\Omega_{0,\Lambda}}{\Omega_{0,M}}\right)^{1/3} . \tag{1.43}$$

Using the current density value for each component (Planck Collaboration: Aghanim et al. (2020)):

$$\begin{cases} \Omega_{0,M} \approx 0.307 \\ \Omega_{0,R} \approx 10^{-5} \\ \Omega_{0,\Lambda} \approx 0.693 \end{cases} \tag{1.44}$$

we get:

$$z_{eq} \approx 6 \cdot 10^3 \qquad \text{and} \qquad z_{eq,\Lambda} \approx 0.3\,. \tag{1.45}$$

If $z > z_{eq}$ we are studying the Radiation Era and we can neglect the other components, if $z_{eq,\Lambda} < z < z_{eq}$ we are studying the Matter Era, while if $z < z_{eq,\Lambda}$ we call it Dark Energy Era.

1.5 Einstein-de Sitter model

The Einstein-de Sitter (EdS) Universes are flat Universes ($k = 0\,, \Omega_0 = 1$) that play an important role in cosmology. It can be shown that they are valid for a large part of the history of our Universe (a possible curvature only becomes important at low z). To describe them we consider a single component with equation of state: $P = W\rho c^2$. We rewrite the Friedmann equation (1.22) as a function of the parameter W

$$\left(\frac{\dot{a}}{a_0}\right)^2 = H_0^2 \left[1 - \Omega_0 + \Omega_0 \left(\frac{a_0}{a}\right)^{1+3W}\right] . \tag{1.46}$$

If $\Omega_0 = 1$ this equation becomes

$$\left(\frac{\dot{a}}{a_0}\right)^2 = H_0^2 \left(\frac{a_0}{a}\right)^{1+3W} \rightarrow \left(\frac{\dot{a}}{a_0}\right) = H_0 \left(\frac{a_0}{a}\right)^{\frac{1+3W}{2}}$$

$$\dot{a} = a_0 H_0 \left(\frac{a_0}{a}\right)^{\frac{1+3W}{2}} \rightarrow \frac{da}{dt} = H_0 a_0^2\, a^{-\frac{1+3W}{2}} ,$$

separating the variables and integrating we obtain

$$a(t) = a_0 \left(\frac{t}{t_0}\right)^{\frac{2}{3(1+W)}} . \tag{1.47}$$

But we have seen that

$$\rho(t) = \rho_0 \left(\frac{a_0}{a}\right)^{3(1+W)} . \tag{1.48}$$

Then substituting (1.47) into (1.48) we obtain

$$\rho(t) = \rho_0 \left(\frac{t}{t_0}\right)^{-2} \longrightarrow \rho(t) \propto t^{-2} . \tag{1.49}$$

To summarize, the Eds model is a Universe in increasing monotonous expansion, which decelerates in a constant and infinite way.

1.6 Decoupling redshift

The history of the Universe is a history of cooling. The actual temperature of the Universe is $T_0 = 2.73K$, that is the mean temperature of the CMB radiation. Going backwards in time, what is called early Universe, temperature was higher than today. However, the Universe is made of multiple species and it is not certain that they all have the same temperature for the entire life of the Universe.
Two or more species of the Universe maintain the same temperature as long as the interactions between them are efficient enough to maintain an equilibrium condition. So to know if two components are at equilibrium, we can compare two scale times:

- **Collisional scale time**
  $\tau_{coll} = \frac{1}{Nc\sigma}$
- **Expansion scale time**
  $\tau_{exp} = \frac{1}{H}$

where N represents the density number, c is the speed of light, σ is the cross-section and H is the Hubble parameter. If $\tau_{coll} < \tau_{exp}$ they are in equilibrium.
To know if Matter and Radiation are currently in equilibrium, we take $N = \rho_{0,M}/m_p$ and $\sigma = \sigma_H$ since, today much of the matter is in neutral form and we get:

$$\tau_{coll,0} \gg \tau_{exp,0} . \tag{1.50}$$

Meaning that the interactions are not efficient for maintaining a state of equilibrium and

$$T_{M,0} \neq T_{R,0} , \tag{1.51}$$

therefore, we can consider them as separate components. Using the adiabaticity equation it is possible to study the trends of the two temperatures with the redshift and it is possible to prove that

$$T_M \propto (1+z)^2 , \qquad T_R \propto (1+z) . \tag{1.52}$$

Matter and radiation, when they are decoupled, follow different adiabatics. All this applies to $t = t_0$, but we must ask ourselves if it is also valid at earlier times. If we look at the definition of the collisional scale time we have that $\tau_{coll} \propto \rho_M^{-1}$, but $\rho_M \propto (1+z)^3$ so $\tau_{coll} \propto (1+z)^{-3}$: going back in time, the density of matter increases and the collisional time decreases. Furthermore, at higher temperatures, the cross section changes ($\sigma_H \to \sigma_T$) and the Thomson cross section is much more efficient. It can be shown that there is a value of z, called the decoupling redshift (z_{dec}), before which the two components are coupled. This means that for $z > z_{dec}$ matter and radiation are in equilibrium and follow the same adiabatic, that can be shown to be:

$$T \propto a^{-1} \propto (1+z)^1 \,. \tag{1.53}$$

1.7 Cosmological Horizon

Another scale length that will be useful for the next chapter is the so-called Cosmological Horizon R_H. It represents the finite region of the Universe in causal connection. To have causal connection, the regions considered must be able to communicate and the maximum communication speed is the speed of light. However, the Universe is expanding and thus we define R_H as

$$R_H(t) = a(t) \int_0^t \frac{c dt'}{a(t')} \,. \tag{1.54}$$

It can be shown that the cosmological horizon is finite and grows over time due to the expansion of the Universe, hence the causally connected region is finite and grows faster than the speed of light. This means that larger and larger regions of the Universe come into causal contact with the observer.

Chapter 2

Theory of structure formation

The Cosmological Principle tells us that on large scales the Universe is isotropic and homogeneous, but we know that this is no longer true on small scales as we observe galaxies, clusters etc. In this Chapter we will discuss the theories of structure formation and evolution. We will also go through the major characteristics of the power spectrum, which are helpful for figuring out how to distinguish between different Dark Matter models.

2.1 Jeans Scale

Once the thermodynamic properties of a halo $(T, \rho, P, ...)$ have been fixed, the Jeans scale represents the minimum scale that a perturbation must have in order for it to increase. To derive its definition, we use the Jeans theory's main premise, which states that the collapse is governed by two opposing processes: gravity collapse and pressure inside collapsing haloes caused by thermal movements of the particles. For a spherical collapse of a cloud of radius R, mass M and with particles moving with speed v we can derive the Jeans scale R_J through different approaches, For example, we can consider the balance between kinetic energy and potential energy:

$$E_K = \frac{1}{2}Mv^2\,, \qquad\qquad E_p = -\frac{GM^2}{R}\,.$$

For the cloud to collapse, the potential energy must be greater than the kinetic energy, so to find the minimum scale we equal the two components

$$E_K = E_p \rightarrow \frac{v^2}{2} = \frac{GM}{R_J} = \frac{G\rho R_J^3}{R_J} = G\rho R_J^2$$

and derive the Jeans scale as

$$R_J = \frac{v}{\sqrt{2G\rho}}\,. \tag{2.1}$$

Then, if $R > R_J$, $E_p > E_K$, the perturbation can collapse and grow.

2.2 Classic Jeans Theory

The classic Jeans theory is a linear theory of gravitational instabilities in a static Universe. To describe our system we need the hydrodynamic equations :

1. **Mass Conservation Equation**

$$\frac{\partial \rho}{\partial t} + \vec{\nabla} \cdot (\rho \vec{v}) = 0 \,; \tag{2.2}$$

2. **Euler's Equation**

$$\frac{\partial \vec{v}}{\partial t} + (\vec{v} \cdot \vec{\nabla})\vec{v} = -\frac{1}{\rho}\vec{\nabla} P - \vec{\nabla}\Phi \,; \tag{2.3}$$

3. **Poisson's Equation**

$$\nabla^2 \Phi = 4\pi G \rho \,; \tag{2.4}$$

4. **Equation of State**

$$P = P(\rho, S) \,. \tag{2.5}$$

where P, Φ and S represent pressure, potential and entropy respectively.
We have a system with 5 variables (ρ, v, P, Φ, S) and 4 equations, but by definition the Universe is adiabatic ($dS = 0$), thus we can consider a barotropic equation of state $P = P(\rho)$. We obtain a system of 4 variables and 4 equations. The state of equilibrium is introduced through the so-called background conditions:

$$\begin{cases} \rho_B = const \\ P_B = const \\ \Phi_B = const \\ \vec{v} = 0 \end{cases} \tag{2.6}$$

Then we apply small perturbations to each of the background conditions, to study how the system evolves:

$$\begin{cases} \rho = \rho_B + \delta\rho \\ P = P_B + \delta P \\ \Phi = \Phi_B + \delta\Phi \\ \vec{v} = \delta\vec{v} \end{cases} \tag{2.7}$$

Since these perturbations are small, we can neglect the second-order terms, linearizing the equations. Using equations (2.2), (2.3), (2.4), the perturbed solutions (2.7) and neglecting the second-order terms, we get:

$$\begin{cases} \frac{\partial \delta\rho}{\partial t} + \rho_B \vec{\nabla} \cdot \delta\vec{v} = 0 \\ \\ \frac{\partial \delta\vec{v}}{\partial t} = -v_s^2 \vec{\nabla}(\frac{\delta\rho}{\rho_B}) - \vec{\nabla}\delta\Phi \\ \\ \nabla^2 \delta\Phi = 4\pi G \delta\rho \end{cases} \tag{2.8}$$

where in the second equation we defined the speed of sound:

$$v_s^2 \doteq \left(\frac{\partial P}{\partial \rho}\right)_S . \tag{2.9}$$

The system solutions will tell us how small perturbations evolve in a static Universe. It is convenient to study these solutions in Fourier space, so that the differential equations are transformed into algebraic equations. We define the solutions in the following way:

$$\begin{cases} \delta\rho = \delta\rho_k \, e^{i(\vec{k}\cdot\vec{r}+\omega t)} \\ \delta\Phi = \delta\Phi_k \, e^{i(\vec{k}\cdot\vec{r}+\omega t)} \\ \delta v = \delta v_k \, e^{i(\vec{k}\cdot\vec{r}+\omega t)} \end{cases} \tag{2.10}$$

with $\vec{r}$ the spatial vector, $(\delta\rho_k, \delta\Phi_k, \delta v_k)$ the amplitudes of the waves and $\vec{k} = \frac{2\pi}{\lambda}\hat{k}$ the wave vector. Defining the so-called density contrast $\delta \doteq \delta\rho/\rho_B$ and substituting equations (2.10) in (2.8), we obtain the hydrodynamic equations of the perturbations in algebraic form :

$$\begin{cases} \omega\delta_k + k\delta v_k = 0 \\ \\ \omega\delta v_k = -k(v_s^2\delta_k + \delta\Phi_k) \\ \\ \delta\Phi_k = -\frac{4\pi G}{k^2}\rho_B\delta_k \end{cases} \tag{2.11}$$

The solutions are derived by setting the Jacobian J of the system to zero :

$$\begin{bmatrix} \omega & k & 0 \\ \\ kv_s^2 & \omega & k \\ \\ \frac{4\pi G\rho_B}{k^2} & 0 & 1 \end{bmatrix} = \quad 0 \, . \tag{2.12}$$

Obtaining the so-called **dispersion equation**

$$\omega^2 = k^2 v_s^2 - 4\pi G \rho_B \,, \tag{2.13}$$

which links the pulsation of plane waves to the speed of sound and to the wave vector. This equation has two possible solutions, depending on the sign of ω^2 , that discriminates between real ($\omega^2 > 0$) and imaginary values ($\omega^2 < 0$). The value that discriminates the two cases is $\omega^2 = 0$ and defines the Jeans wave number:

$$k_J = \frac{\sqrt{4\pi G \rho_B}}{v_s} \,. \tag{2.14}$$

In the real space we find the definition of Jeans scale:

$$\lambda_J = \frac{2\pi}{k_J} = v_s \sqrt{\frac{\pi}{G\rho_B}} \,. \tag{2.15}$$

Then we can write the dispersion equation

$$\omega^2 = k^2 v_s^2 \left(1 - \frac{k_J^2}{k^s}\right) = k^2 v_s^2 \left[1 - \left(\frac{\lambda}{\lambda_J}\right)^2\right] \,. \tag{2.16}$$

Depending on the values of λ, we will have two kinds of solutions:

- **Physically small scales** if $\lambda < \lambda_J$, where $\omega^2 > 0$ and the pulsation is real. We have two waves of small amplitude that propagate in opposite directions. In this case the perturbations cannot grow.
- **Physically big scales** if $\lambda > \lambda_J$, where $\omega^2 > 0$ and the pulsation is imaginary. Substituting these pulsations in equations (2.10), we obtain stationary waves with amplitude increasing over time:

$$\delta_\pm = \delta_k \, e^{\pm|\omega|t} \, e^{i\vec{k}\cdot\vec{r}} \,. \tag{2.17}$$

Equation (2.17) represents the solutions for the evolution of perturbations in a static Universe, valid only in a linear regime, i.e. until $\delta \ll 1$.

2.3 Cosmological Jeans Theory

The Classic Jeans theory holds for a static Universe, but in reality our Universe is expanding, and the expansion tends to contrast the collapse of matter. The background solutions in this situation will no longer be constant, but instead functions of time. We must examine several fundamental scales in order to understand how to use Jeans theory in an expanding Universe:

1. **Horizon scale** $R_H(t)$, defined in equation (1.54), which represents the scale under which there is causal connection and microphysical phenomena must be taken into account. On scales greater than the horizon, the only interaction to consider is gravity: all the perturbations can collapse and grow.

2. **Jeans scale** R_J, this scale only makes sense within the horizon, since it depends on the interactions between the components, and represents the scale that discriminates what can grow ($R > R_J$) from what cannot grow ($R < R_J$) and propagates as a wave.

3. **Dissipation scale** R_D. It represents the scale under which the wave propagation causes the wave to dissipate, canceling the perturbation.

4. **Equivalence time** t_{eq}. It represents the moment in which matter begins to dominate the radiation. For $t > t_{eq}$ we will be in the radiative era, where the radiation pressure dominates and opposes gravity.

5. **Decoupling time** t_{de}. It represents the moment in which matter decouples from the radiation. The different components of matter decouple at different times, changing the behavior of the collapse.

6. **Non-relativistic time** t_{NR}. It represents the time beyond which a component stops being relativistic and depends on the mass of the particles.

Having defined these fundamental scales, we can study the evolution of perturbations in an expanding Universe on different scales.

2.3.1 Outside the cosmological horizon

We consider scales $R > R_H$ where only gravity acts. The idea is to consider a perturbation as a small closed Universe ($\Omega_{tot} > 1$, $k = +1$) immersed in a flat Universe ($\Omega_{tot} = 1$, $k = 0$). From the Friedmann equation (1.22) divided by a^2, we have

$$\frac{\dot{a}^2}{a^2} = \frac{8}{3}\pi G\rho\frac{a^2}{a^2} - \frac{kc^2}{a^2} \longrightarrow H^2 = \frac{8}{3}\pi G\rho - \frac{kc^2}{a^2}\,, \tag{2.18}$$

we can consider separately the perturbation (H_P) and the background Universe (H_B):

$$H_B^2 = \frac{8}{3}\pi G\rho_B\,, \qquad\qquad H_P^2 = \frac{8}{3}\pi G\rho_P - \frac{c^2}{a^2}\,. \tag{2.19}$$

We look for solutions that are synchronized, so the two equations must be equal:

$$H_B^2 = H_P^2 \rightarrow \frac{8}{3}\pi G\rho_B = \frac{8}{3}\pi G\rho_P - \frac{c^2}{a^2}$$

$$\frac{8}{3}\pi G(\rho_P - \rho_B) = \frac{c^2}{a^2}$$

$$\frac{8}{3}\pi G\delta = \frac{c^2}{a^2}\frac{1}{\rho_B} \rightarrow \delta = \frac{3c^2}{8\pi G}\frac{1}{\rho_B a^2}\,. \tag{2.20}$$

We defined $\delta \doteq (\rho_P - \rho_B)/\rho_B$ and from equation (2.20) we notice:

$$\delta \propto \frac{1}{\rho_B\, a^2}\,. \tag{2.21}$$

If $z > z_{eq}$, we are in the Radiative Era and $\rho_B = \rho_R \propto a^{-4}$, so $\delta = \delta_R \propto a^{-2}a^4$ then $\delta \propto a^2$. Being outside the horizon, the only force to consider is the gravitational force, then all the other components will follow the trend of the dominant component as well $\delta_{DM} \propto \delta_b \propto \delta_R \propto a^2$. Conversely, if $z < z_{eq}$, $\rho_B = \rho_M \propto a^{-3}$, so $\delta = \delta_M \propto a^{-2}a^3$ then $\delta \propto a$ and again all the other components will follow this trend.
To summarize, if we are outside the horizon $R > R_H$ the perturbations always grow, but with a trend that changes at the time of equivalence:

$$\begin{cases} \delta \propto a^2 & z > z_{eq} \\ \delta \propto a & z < z_{eq} \end{cases} \tag{2.22}$$

2.3.2 Inside the cosmological horizon

To find solutions within the horizon, the expansion of the Universe must be taken into account. In this case it is more convenient to work with co-moving coordinates and we will call $\vec{r}$ the physical coordinates and $\vec{x}$ the co-moving ones, where $\vec{r} = a\vec{x}$. In this case

$$\dot{\vec{r}} = \frac{d\vec{r}}{dt} = \dot{a}\vec{x} + a\dot{\vec{x}} = H\vec{r} + a\dot{\vec{x}}\,. \tag{2.23}$$

The physical variation of a body's position, that depends on the Hubble flux ($H\vec{r}$) plus a perturbative term $a\dot{\vec{x}}$. We define the velocity in physical coordinates:

$$\vec{u} = H\vec{r} + \delta\vec{v}\,. \tag{2.24}$$

We take the hydrodynamic equations (2.2), (2.3), (2.4) and write them in physical coordinates

$$\frac{\partial}{\partial f}\Big|_{\vec{r}}\rho + \vec{\nabla}_{\vec{r}}\cdot(\rho\vec{u}) = 0\,; \tag{2.25}$$

$$\frac{\partial}{\partial f}\Big|_{\vec{r}}\,\vec{u} + (\vec{u}\cdot\vec{\nabla}_{\vec{r}})\vec{u} = -\frac{1}{\rho}\vec{\nabla}_{\vec{r}}P - \vec{\nabla}_{\vec{r}}\Phi\,; \tag{2.26}$$

$$\nabla^2_{\vec{r}}\Phi = 4\pi G\rho\,. \tag{2.27}$$

To study the solutions of Jeans theory in an expanding Universe, we follow the same procedure used for a static Universe. Now the background solutions derived from a Friedmann Universe and are not static, but are functions of time. Moreover, $\vec{v} \neq 0$. As before, we take the background solutions, add small perturbations, replace these perturbations in the hydrodynamic equations and neglect the second-order terms. Using the relation $\vec{r} = a\vec{x}$ we transform the equations into co-moving coordinates and we look for solutions in Fourier space (the amplitude of fluctuations are not constant over time). The differential equations become algebraic equations. Using this system of equations it is possible to obtain the dispersion relation :

$$\ddot{\delta}_k + 2\frac{\dot{a}}{a}\dot{\delta}_k + \delta_k\Big[k^2v_s^2 - 4\pi G\rho_B\Big] = 0\,, \tag{2.28}$$

which describes the time evolution of the density field in an expanding Universe. This equation tells us that the density field is controlled by a term related to the expansion ($H = \dot{a}/a$) that opposes the collapse, while in the second term we have a competition between velocity dispersion and the gravitational field.

2.4 Perturbations evolution in an EdS Universe

Considering an EdS Universe of matter only: $\Omega_{tot} = \Omega_M = 1$ and $W = 0$. We start at $t > t_{eq}$ and $R < R_H$. Under these conditions we have:

$$a \propto t^{2/3}\,, \qquad H = \frac{2}{3}\frac{1}{t}\,, \qquad \rho_B = \frac{1}{6\pi G t^2}\,. \tag{2.29}$$

The dispersion relation (2.28) becomes:

$$\ddot{\delta}_k + \frac{4}{3}\frac{1}{t}\dot{\delta}_k + \frac{2}{3}\,\delta_k\,\frac{1}{t^2}\,\left[\frac{k^2v_s^2}{4\pi G\rho_B} - 1\right] = 0\,. \tag{2.30}$$

We are looking for solutions such as $\delta_k \propto t^\alpha$, to make explicit the dependence on time. In terms of α the dispersion relation is

$$3\alpha^2 + \alpha + 2\left(\frac{k^2v_s^2}{4\pi G\rho_B} - 1\right) = 0\,, \tag{2.31}$$

which is a second-order equation (two real solutions or two imaginary solutions). In order for the perturbations to grow, we need the solutions to be real and this happens if

$\Delta > 0$. The discriminating value, that allows us to derive the Jeans scale is $\Delta = 0$ and we get

$$\lambda_J = v_s \sqrt{\frac{24\pi}{25 G \rho_B}} \,. \tag{2.32}$$

If $\Delta > 0$ and $\lambda \gg \lambda_J$ we can solve the equation (2.31). We get $\alpha_- = -1$ and $\alpha_+ = 2/3$, then the increasing perturbations is:

$$\delta_+ \propto t^{2/3} \propto a \,. \tag{2.33}$$

All the perturbations of matter in the EdS Universes in linear regime, for $\lambda \gg \lambda_J$, grow as the expansion factor.

2.5 Perturbation evolution in a Radiative Universe

In the radiative era, the contribution of the radiation pressure must be taken into account. Then we take the hydrodynamic equations and substitute $\rho \to \rho + 3P/c^2$:

$$\begin{cases} \frac{\partial \rho}{\partial t} + \vec{\nabla}\left(\rho + \frac{P}{c^2}\right)\vec{v} = 0 \\ \left(\rho + \frac{P}{c^2}\right)\left[\frac{\partial \vec{v}}{\partial t} + \vec{v}\,\vec{\nabla}\,\vec{v}\right] + \vec{\nabla} P + \left(\rho + \frac{P}{c^2}\right)\vec{\nabla}\Phi \\ \nabla^2 \delta\Phi = 4\pi G\left(\rho + \frac{3P}{c^2}\right) \end{cases} \tag{2.34}$$

Following the same procedure used in the previous cases, we find the dispersion relation in a Radiative Universe:

$$\ddot{\delta}_k + 2\frac{\dot{a}}{a}\dot{\delta}_k + \delta_k \left[k^2 v_s^2 - \frac{32}{3}\pi G \rho_B\right] = 0 \,. \tag{2.35}$$

Being $z > z_{eq}$, we can consider the Universe EdS, but we are in the Radiative era then $W = \frac{1}{3}$, then the dispersion equation becomes

$$\ddot{\delta}_k + \frac{\dot{\delta}_k}{t} + \delta_k \left[k^2 v_s^2 - \frac{1}{t^2}\right] = 0 \,. \tag{2.36}$$

Now we write the dispersion equation as a function of α ($\delta_k \propto t^\alpha$):

$$\alpha^2 = 1 - k^2 v_s^2 t^2 \,. \tag{2.37}$$

We find that the Jeans scale for $t < t_{eq}$ is

$$\lambda_J = v_s \sqrt{\frac{3\pi}{8 G \rho}} \,. \tag{2.38}$$

For $\lambda \gg \lambda_J$ we can solve the equation (2.37) and we get $\alpha_{+/-} = \pm 1$. The increasing solution is:

$$\delta_+ \propto t \propto a^2 \,. \tag{2.39}$$

These equations hold for $R > R_H$, but we want to know how big the Jeans scale is relative to the horizon. From the dispersion relation:

$$\alpha^2 = 1 - k^2 v_s^2 t^2 = 0 \rightarrow k_J = \frac{1}{v_s t} \rightarrow \lambda_J = 2\pi v_s t \rightarrow \lambda_J = \frac{2\pi c t}{\sqrt{3}} \,. \tag{2.40}$$

This scale only makes sense within the horizon, because outside any perturbation can grow. If we calculate the radius of the horizon at this time:

$$R_H(t) = a(t) \int_0^t \frac{c dt'}{a(t')} \,, \tag{2.41}$$

in an Eds Universe with $W = 1/3$, we have $a(t) = a_0 (t/t_0)^{1/2}$, then the horizon becomes

$$R_H(t) = 2\, c\, t \,. \tag{2.42}$$

In the Radiative era $\lambda_J > R_H$, and this means that this Jeans scale has no physical sense: in this era it is not possible to make the radiative perturbations grow inside the horizon. Thus, $\rho_R = 0$ and as long as matter is coupled to radiation, matter perturbations will also not grow due to radiation pressure. This phenomena is one of the proofs of the presence of dark matter. Since baryonic perturbations do not grow until decoupling, there must be another component of matter that acts differently to produce the perturbations that we see today. Dark Matter decouples sooner than baryons, and its perturbations might begin to develop shortly after the period of equivalence. After decoupling, baryonic perturbations develop faster because they can take advantage of the potential wells left by dark matter after it has grown.

2.6 Statistical treatment of perturbations

According to inflation theories, statistical fluctuations in the metric (spiraling in the inflaton phase space) produce the perturbation field in the last phases of inflation, and the perturbations are generated with a stochastic and quasi-Gaussian distribution. We can assume that the perturbations in the early Universe follow a Gaussian distribution so the probability to have a perturbation $\delta(\vec{x})$ is:

$$P(\delta(\vec{x})) = \frac{1}{2\pi\sigma^2} \exp\left[\frac{-(\delta(\vec{x}) - <\delta>)^2}{2\sigma^2}\right] \,, \tag{2.43}$$

where the perturbations are defined as

$$\delta = \frac{\delta\rho}{<\rho>} = \frac{\rho - <\rho>}{<\rho>} \,. \tag{2.44}$$

Being $P(\delta)$ Gaussian, it is defined only by its average $< \delta >$ and variance $< \delta^2 >$, but by definition $< \delta >= 0$, then the only value that defines this field is the variance.
To apply a statistical method, we require a suitably big sample, which means we wish to witness the occurrence several times. This is not possible in the case of the Universe because the sample consists of just one element: the Universe itself. To overcome the difficulty, we may use the ergodic hypothesis (for a Gaussian field it becomes a theorem), which states that while we can not create averages on many different realizations of the Universe, we must make them on sufficiently vast and distinct sub-spaces. This hypothesis states that, because of the CP, we may think of our Universe as a collection of statistically independent sub-Universes.
To perform a statistical analysis, we go to Fourier space and consider a perturbation as a superposition of plane waves. Then in the Fourier space a perturbation $\delta(\vec{x})$ becomes:

$$\delta(\vec{k}) = \frac{1}{(2\pi)^3} \int \delta(\vec{x})\, e^{-i\vec{k}\cdot\vec{x}}\, dx^3 \,. \tag{2.45}$$

2.6.1 Power Spectrum

One of the most effective tools for studying perturbations from a statistical point of view is the so-called Power Spectrum $P(\vec{k})$. It tells us how important a fluctuation is on a given length-scale $L = 2\pi/|\vec{k}|$: the larger $P(\vec{k})$, the larger the amplitude of the fluctuations on this length-scale. Since we have decomposed a perturbation as the sum of plane waves with wave vector $\vec{k}$, we can say that the Power spectrum describes the distribution of amplitudes with equal $k = |\vec{k}|$. We can define the power spectrum analytically, through another quantity called Two-point correlation function

$$\xi(\vec{r}) = < \delta(\vec{x})\delta(\vec{x} + \vec{r}) > \ . \tag{2.46}$$

It is the average of the product between two values of the field of fluctuations, taken between two points at co-moving distance $r = |\vec{r}|$. Given this definition, it can be shown that the correlation function and the power spectrum represent a Fourier pair:

$$\xi(\vec{r}) = \frac{1}{(2\pi)^3} \int P(k)\, e^{i\vec{k}\cdot\vec{r}}\, d^3k \,. \tag{2.47}$$

The correlation function, defined in real space, is the inverse transform of the power spectrum, defined in Fourier space. From equation (2.47) it is possible to prove that

$$P(k) \propto < \delta^2(\vec{k}) > \ . \tag{2.48}$$

The power spectrum is proportional to the variance of the amplitude of a perturbation with wave number $\vec{k}$.

2.6.2 The Initial Power Spectrum

At early times, the expansion of the Universe follows a power law, in the radiation-dominated era and at that time, no natural length-scale existed to which one might compare a wavelength. The only mathematical function that depends on a length but does not contain any characteristic scale is a power law; hence for very early times one should expect

$$P(k) = A\,k^n\,, \tag{2.49}$$

where A is the amplitude, and n is called spectral index. However, primordial perturbations are the result of a stochastic process due to the oscillation of the so called inflaton and therefore we expect these fluctuations not to have privileged scales. Oscillating, the inflaton creates fluctuations in the metric, i.e. fluctuations in the gravitational potential $\delta\Phi$. Assuming a power spectrum with a power law (2.49), it is possible to prove that

$$\delta\Phi \propto M^{\frac{1-n}{6}}\,. \tag{2.50}$$

To get a scale free relationship, we must assume $n = 1$, then the primordial power spectrum (called the Zeldovich spectrum) becomes

$$P(k) = A\,k\,. \tag{2.51}$$

This trend is valid only in primordial epochs, while its shape and its evolution will depend on cosmology. For a complete discussion see Zeldovich (1972).

Chapter 3

Dark Matter

The first hints of the existence of dark matter come from the 1930s when Zwicky discovered dynamical evidence that the Coma cluster has ten to one hundred times more mass than luminous matter in galaxies (Zwicky 1933). However, it was not until the early 1980s that astronomers realized that the majority of the mass keeping galaxies and clusters of galaxies together is invisible. According to astronomical measurements, baryonic matter makes up just around 16% of the total quantity of matter in the Universe. The remaining 84% is attributed to a new type of matter that cannot be observed by the light it emits, called *Dark Matter* (DM). In this scenario, gravitational DM interactions are the only ones that matter for structure formation. Given the importance of DM role, determining what it is has become one of the greatest challenge of this century. The evidence for dark matter's existence is vast and compelling. It comes from cosmic structures on all scales and across all epochs, from the faintest dark-matter-dominated dwarf galaxies to the largest clusters of galaxies, the large-scale structure of the Universe, and back to the very seeds of cosmic background radiation. This collection of data may be explained by a coherent theory of structure formation in which dark matter gravity amplifies primordial density perturbations imprinted during an early era of cosmic inflation. In this chapter we will look at the role of dark matter in the structure formation and evolution discussing over the the main detection methods and probable candidates.

3.1 Dark Matter Perturbation evolution

Accurate observations of the temperature anisotropies and polarization of cosmic microwave background (CMB) in principle allow us to derive the parameters of the Standard Cosmological Model with very high accuracy. For this reason, these observations are one of the greatest proofs of the existence of dark matter. Although the isotropic microwave background suggests that the Universe was once quite homogeneous, we know that today it is far from homogeneity: we observe galaxies, clusters, empty regions and

superclusters. In the current model of structure formation, these structures form from extremely small primordial inhomogeneities that grew in size over time due to gravitational instability. These inhomogeneities leave a mark (anisotropy in temperature) in the microwave background. First discovered by COBE in 1992, and more recently investigated in much more detail by the Planck mission (see Fig. 3.1), these fluctuations, linked to the density perturbations, have an amplitude of the order of 10^{-5} at the last scattering surface ($z \sim 1100$). Therefore, a theory of structure formation must explain

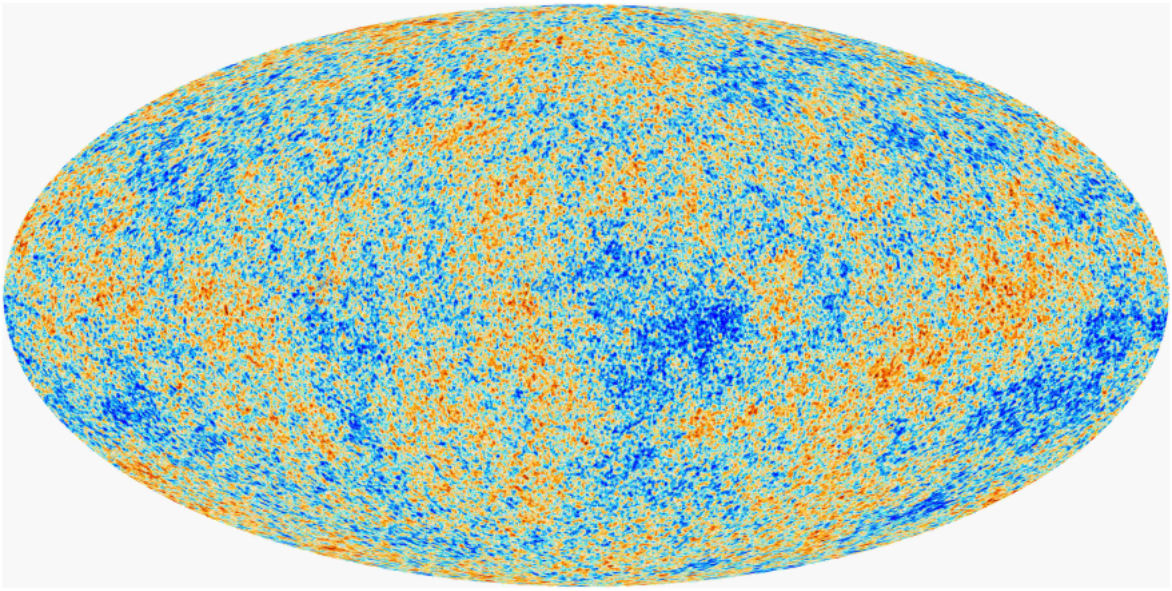

Figure 3.1: *The anisotropies of the microwave background measured by the Planck satellite with 4 arcminute resolution. It shows tiny temperature fluctuations* ($\Delta T \sim 10^{-5}$) *that correspond to regions of slightly different densities, representing the seeds of all future structure: the today large scale structure of the Universe. In this map the galactic foreground has been properly subtracted. Credits: Aghanim et al. (2020)*

the evolution of the Universe from a nearly homogeneous initial state, with small matter density perturbations, $\delta \sim 10^{-5}$ at $z \sim 1100$, up to density contrasts larger then 10^3 for galaxies at $z << 1$. The most common hypothesis to explain this rapid growth of density perturbations, which is not possible in a Universe made up of baryons only, is the existence of an invisible type of matter: the Dark Matter.
Another strong direct evidence for the presence of a large quantity of dark matter is the flat rotation curves of spiral galaxies. Spiral galaxies have a central bulge and a very narrow disk that are supported by angular momentum and surrounded by a dark matter halo that is roughly spherical. The Doppler shifts of spectral lines can be used to calculate the orbital velocities of objects orbiting around the disk as a function of radius. Babcock (1939) estimated the Andromeda galaxy's rotation curve from the stars in the

disk for the first time in 1939. Later, it became feasible to measure galactic rotation curves far out in to the disk, and a trend was discovered: the orbital velocity increases linearly from the center outward until it reaches a peak, then flattens out to the greatest recorded radii (see Fig. 3.2). This was completely unexpected since the observed surface luminosity of the disk falls off exponentially with radius. Thousands of galaxy rotation curves are now known, and all the results point to the fact that dark matter must be present as a hidden underlying component, to explain the shape of rotation curves.

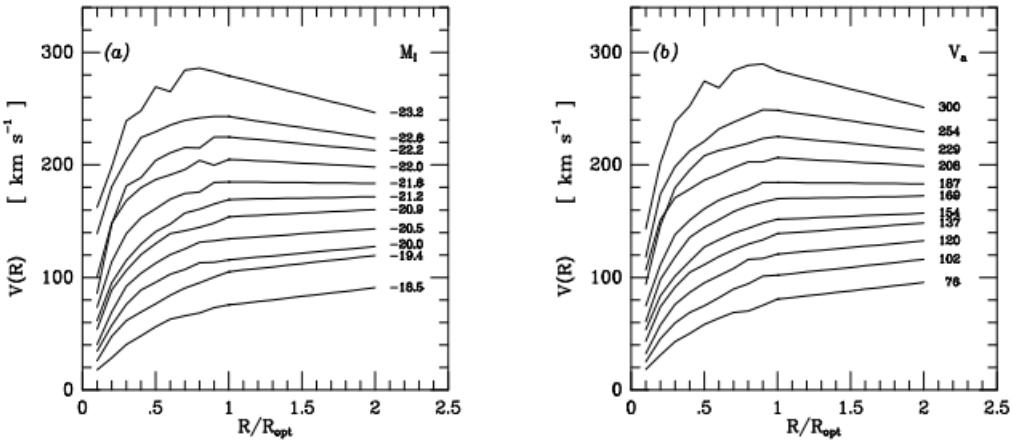

Figure 3.2: *The rotation curves of several spiral galaxies. Galactocentric radii are normalized to R_{opt}, the radius encompassing 83% of the total $I-$band luminosity. Credits: Persic, Salucci, and Stel (1996).*

3.1.1 Primordial Power Spectrum

As we saw in section 2.6.2, the starting point of structure formation is the end of cosmic inflation when dark matter perturbations are predicted to have a nearly scale-invariant power spectrum: $P(k) \propto k^n$, with a spectral index $n = 0.965$, derived by the Plank collaboration (Aghanim et al. 2020). Then, self-gravity drives the growth of dark matter perturbations in the expanding Universe and in the linear regime ($\delta << 1$) this growth can be described by the linear perturbation theory seen in Chapter 2. The dispersion relation (equation (2.28)), for a DM perturbation $\delta_{k,DM}$, becomes [1].

$$\ddot{\delta}_{k,DM} + 2\frac{\dot{a}}{a}\dot{\delta}_{k,DM} - \delta_{k,DM} 4\pi G \rho_{b,DM} = 0 \tag{3.1}$$

[1] during the radiative era $\delta_{k,R} \sim \delta_{k,B} \sim 0$, therefore there is only the contribution of the DM

and it is possible to show that in a linear regime this equation has the following increasing solution:

$$\delta^{+}_{k,DM} = 1 + \frac{3}{2}x\,, \tag{3.2}$$

where $x = a/a_{eq}$. In this regime, two key events occur that alter the primordial power spectrum. The first, known as Meszaros effect or stagnation, is active for $z < z_{eq}$: the growth of dark matter perturbations on scale lower than the horizon stagnates, while super-horizon scales continue to expand. When matter becomes the main component of the energy density ($z > z_{eq}$), all perturbations grow at the same rate. The transition introduces a characteristic scale in the power spectrum, the size of the horizon at the time of matter-radiation equality: $R_H(t_{eq})$.
The cut-off in the power spectrum, which reflects the nature of the DM particle, is the second crucial effect. This cutoff is imposed by a physical process that is model dependent. The mechanism for collisionless DM is free-streaming, a type of damping whose scale is determined by the horizon size at the time when dark matter particles become non-relativistic; the more massive the particle, the earlier this epoch, and hence the smaller the free-streaming scale. (for more details about Meszaros effect and Free-streaming see Appendix A). To understand how the two effects modify the primordial power spectrum, we can introduce the mass of the horizon $M_H \propto \rho_M R_H^3$, where

$$M_H \propto \begin{cases} a^3 & if \quad a < a_{eq} \\ a^{\frac{3}{2}} & if \quad a > a_{eq} \end{cases} \tag{3.3}$$

Then we will have two different situations:

- Scales entering the horizon before equivalence $a_H < a_{eq}$ experience stagnation. Such scales will only grow up to a_H, then at the time of equivalence we will have

$$\delta_k(t_{eq}) = \delta_k(t_i)\left(\frac{a_H}{a_i}\right)^2 \propto \delta_k(t_i)a_H^2 \tag{3.4}$$

, but before equivalence $M_H \propto a^3 \to a^2 \propto M_H^{2/3}$, then

$$\delta_k(t_{eq}) \propto \delta_k(t_i)M_H^{\frac{2}{3}} \propto \delta_k(t_i)k^{-2}\,, \tag{3.5}$$

therefore the power spectrum

$$P(k, t_{eq}) \propto \delta_k^2(t_{eq}) \propto \delta_k^2(t_i)k^{-4} \propto P(k, t_i)k^{-4} \propto k^{n-4}\,. \tag{3.6}$$

The effect of stagnation is a loss of power at the scales that enter the horizon before equivalence.

- Scales entering the horizon after equivalence $a_H > a_{eq}$ do not experience stagnation, then for these scales

$$\delta_k(t_{eq}) = \delta_k(t_i) \left(\frac{a_{eq}}{a_i}\right)^2 \propto \delta_k(t_i) a_{eq}^2 \,, \tag{3.7}$$

therefore the power spectrum

$$P(k, t_{eq}) \propto \delta_k^2(t_{eq}) \propto \delta_k^2(t_i) a_{eq}^4 \propto P(k, t_i) a_{eq}^4 \propto k^n \,. \tag{3.8}$$

For these scales the shape of the spectrum remains the same as the primordial one.

The trend of the power spectrum at the time of equivalence $P(k, t_{eq})$ is schematically plotted in Fig. 3.3. The peak distinguishes the scales that have faced the phenomenon of stagnation, from those that have instead grown while remaining outside the horizon; it represents the size of the horizon at the moment of equivalence, i.e. $k_{eq} = 2\pi/R_H(t_{eq})$. The free-streaming scale, on the other hand, is model dependent: the scale on which we

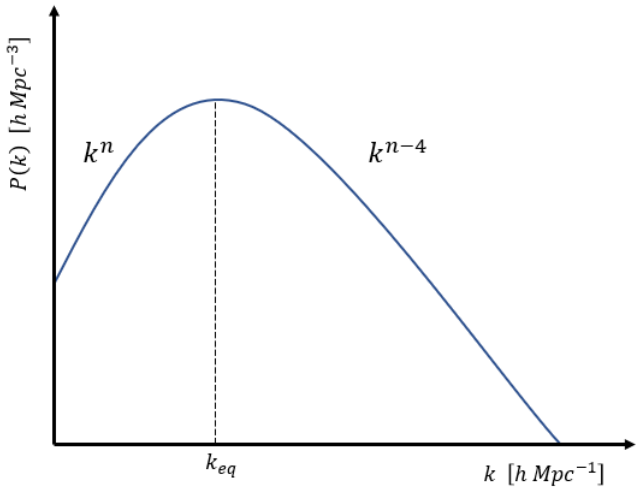

Figure 3.3: *Power spectrum at the time of equivalence. The vertical dashed line corresponds to the scale of the horizon radius at the time of equivalence* $k_{eq} = 2\pi/R_H(t_{eq})$*. The scales with* $k > k_{eq}$ *have undergone the phenomenon of stagnation, then* $P(k) \propto k^{n-4}$*, while scales with* $k < k_{eq}$ *will enter the horizon after equivalence, then* $P(k) \propto k^n$*.*

have the power spectrum cutoff depends on the dark matter model. This means that we can use the point where the spectrum becomes zero $P(k) = 0 = P(k_{FS})$ to discriminate between DM particle models. Fig. 3.4. shows an example of power spectrum for CDM model and different WDM models. For WDM the free-streaming scale shifts to smaller k, which means that in these models we lose power to the small masses. For a more detailed description of the relation between different DM models and particle mass see Appendix A.

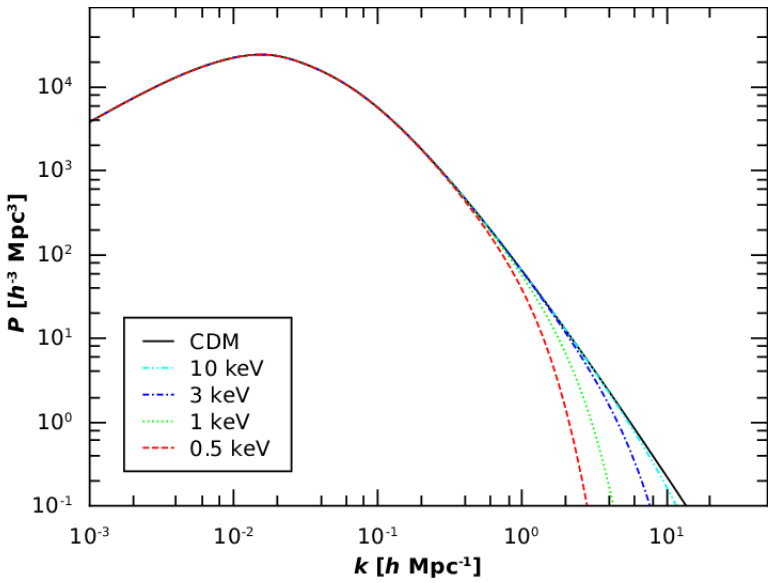

Figure 3.4: *Power spectrum for different DM models. The less massive the DM particles, the smaller the scale for which $P(k_{FS}) = 0$. Credits: Dunstan et al. (2011).*

3.2 The standard cosmological model: ΛCDM

Cosmological and astrophysical data have converged upon the ΛCDM paradigm as the standard model of cosmology which brings together the Big Bang and inflation theories to describe and study the evolutionary history of our Universe. The standard model makes a specific assumption about the nature of dark matter: dark matter consists of non-relativistic, collisionless particles which had negligible thermal velocities at early times (Cold dark matter). In this picture, of the total mass-energy content of the Universe, approximately 26% is cold dark matter (CDM), 5% is baryonic matter and $\sim 69\%$ is in the form of the cosmological constant Λ. This constant generates a negative contribution to pressure (see section 1.3), which explains the current accelerating expansion of space against the attractive forces of gravity.

The **ΛCDM** model has had tremendous success, since it can predict various empirical evidences in our Universe. Fig. 3.5 shows the remarkable agreement between the observed matter power spectrum, obtained from a variety of cosmological probes on different scales, and the **ΛCDM** cosmology. In this scenario, structures in the Universe, formed as primordial overdensities, collapse under the influence of gravity. Thus, since DM dominates and collapses before than baryonic matter, it provides the gravitational potential underlying the distribution of visible matter in the Universe.

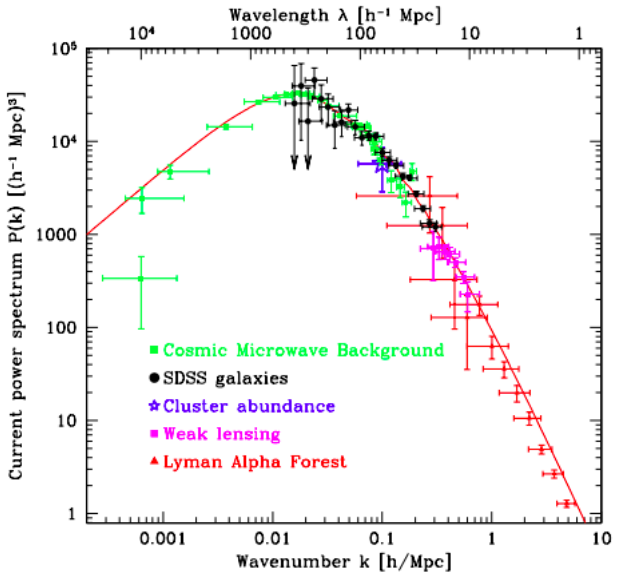

Figure 3.5: *Matter power spectrum inferred through cosmological measurements of the Sloan Digital Sky Survey. Red line shows the best fit for* Λ***CDM*** *cosmology for a simplified five-parameter model, assuming a flat spatial geometry and a scale-invariant primordial spectrum. Credits: Tegmark et al. (2004).*

3.2.1 CDM haloes and NFW profile

The small primordial density perturbations grow in time as a result of gravitational clustering and form self-gravitating bound structures known as dark matter haloes. The basic spherical collapse model may be used to explain how virialised haloes originate (for a more complete discussion of the spherical collapse see Appendix B), but the definition of halo's boundary and its mass it is not unique and several different definitions are in common use, each having different advantages (White 2001). The most common ones, derived in simulations, are:

- **Friends-of-Friends mass**: the mass of a group of particles connected by a percolation scale and characterized by a linking length, b given in units of mean interparticle separation
- **Spherical overdensity mass**: the mass M_Δ contained within a sphere centered on the halo (with the center placed at the halo gravitational potential minimum), with a radius determined by the spherical collapse model, in which the collapsed region that defines a halo contains an average density $\Delta(z)$ times the critical density.
- **Virial mass**: the spherical overdensity mass with $\Delta = 200$, which simulations found as the radius r_{200} that separates the halo dynamical equilibrium region from

the still contracting surrounding region. This is effectively a subset of the previous definition.

According to N-body simulations and observations, regardless the definition of the halo, the spherically averaged mass density profiles of dark matter haloes in dynamical equilibrium have a nearly universal shape that is independent of halo mass, initial conditions, and cosmological parameters (see Fig. 3.6). This is the so-called Navarro-Frenk-White (NFW) profile (Navarro et al. 1997):

$$\rho(r) = \frac{\rho_c \delta_c}{(r/r_s)(1 + r/r_s)^2} \,. \tag{3.9}$$

This profile is described by only two parameters: r_s is the scale length at which the logarithmic slope of the profile is equal to -2 and δ_c defined as

$$\delta_c = \frac{\Delta c^3}{3K_c(c)} \,, \tag{3.10}$$

where $K_c(c) = \ln(1+c) - c/(1+c)$ and $c \doteq r_{vir}/r_s$ is the halo's concentration. The slope

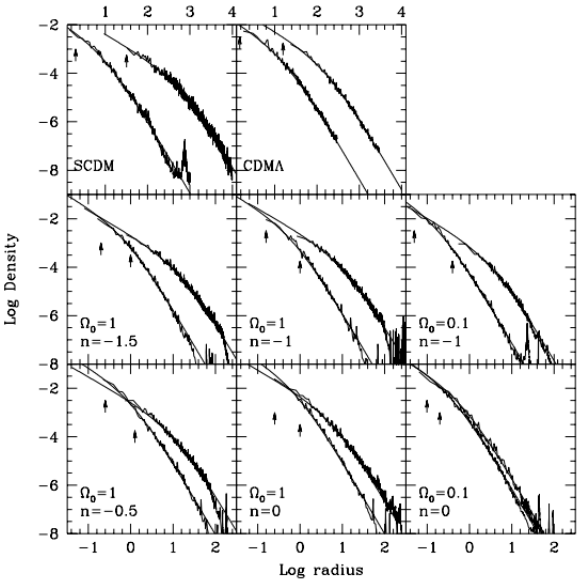

Figure 3.6: *Density profiles of CDM haloes for different masses and cosmological parameter. Radii are given in kpc (scale at top), and densities are in units of* $10^{10} M_\odot\, kpc^{-3}$. *Credits: Navarro et al. (1997).*

of this density profile changes from the central to the outer regions: $\rho(r) \propto r^{-1}$ in the inner regions of the halo and $\rho(r) \propto r^{-3}$ in the outer part, hence an increase in density in the central parts of the DM halos, known as cusp.

3.2.2 Halo mass function

The mass function of dark matter haloes provides the number density of haloes of different mass per unit of volume. The abundance of haloes across cosmic epochs was investigated since the early work of Press and Schechter (1974), based on the properties of the initial Gaussian density field (described by the power spectrum) and the gravitational collapse of density perturbations into virialised haloes as modelled by the spherical collapse model. More recently, the same analyses have been repeated by Sheth and Tormen (2002) extending the P&S formalism with the assumption that the spherical symmetry is replaced by the assumption of ellipsoidal collapse. In the last couple of decades, the halo mass function has been characterised more precisely using the result of N-body simulations over the full range of masses, from dwarf-size haloes to cluster-size haloes. The number density of haloes per unit mass is a decreasing function of the halo mass and scales as:

$$\frac{dn}{dM} \propto M^{\alpha}\,, \tag{3.11}$$

where $\alpha \sim -1.9$ and the normalisation is related to the large scale environment with denser environments having a larger halo abundance. Fig. 3.7 shows an example of halo mass functions built from **ΛCDM** N-body simulations for different redshifts. The solid lines represent the Sheth&Tormen prediction.

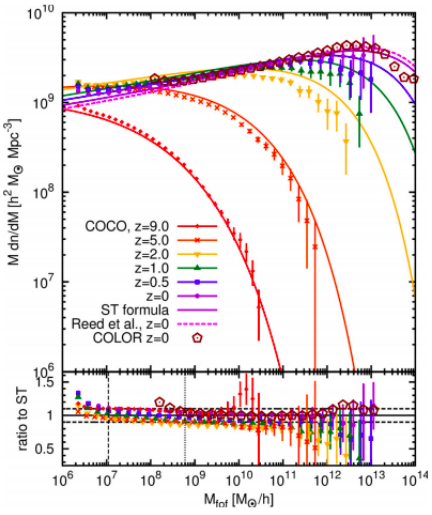

Figure 3.7: *Top: FOF mass functions for the COCO and the COLOR simulations from $z = 9$, to $z = 0$, on which are superimpose the S&T prediction (solid lines). The vertical bars indicate Poisson errors. Bottom: the COCO and COLOR mass functions normalized by the S&T prediction at the corresponding redshift. Credits: Hellwing et al. (2016).*

3.3 Dark Matter detection

Given the large-scale agreement between **ΛCDM** model predictions and observations, understanding the nature of DM is now a significant objective not just for the astrophysics community, but also for the particle physics community. Astronomical evidence for non-baryonic DM is one of the greatest pieces of evidence for physics beyond the Standard Model (SM), driving experimental innovation to discover its existence. The most plausible candidate for the CDM particle is the so-called weakly-interacting massive-particle (WIMP), a massive particle ($m_{DM} \sim 1 - 100\,GeV$) interacting through weak interaction. This model is successful for two reasons: there is high agreement between the predicted and observed abundances of DM (a phenomena known as the WIMP miracle); and this DM candidate occurs naturally in popular extensions of the SM, known as super-symmetry. As a result, all attempts to determine the nature of DM rely on the assumption that DM particles interact with SM particles, i.e. DM is related to SM particles by a force other than gravity. In this framework there are three ways to proceed in detecting DM:

- **Indirect detection**
  The goal of this research is to look at the products of dark matter particle annihilation or decay. The density of DM haloes has a peak in the inner part, thus the annihilation process is supposed to increase there, allowing us to identify the results of these events. Usually, in the case of WIMP annihilation, the end products are expected to be photons in the gamma-ray band;

- **Direct detection**
  The goal is to detect dark matter elastic scatterings from atomic nuclei in a laboratory setting, where the momentum transfer causes a nuclear recoil that may be detected in a variety of ways depending on the detector.

- **Colliders searches**
  Using particle scattering in a collider, try to create dark matter particles during high-energy collisions at particle colliders. Any DM generated would not be detected by particle detectors, but it would subtract energy and momentum. The amount of energy and momentum left over after a collision may thus be used to infer the existence of such particles. In this direction, many experiments are carried out at the Large Hadron Collider (LHC), with different approaches (for a review see Kahlhoefer (2017)).

For now, all these experiments remain unsuccessful and dark matter remains a hypothesis, albeit one with strong empirical support.

3.4 Revealing the nature of Dark matter

Given the failure of experiments presented in the last section and given some discrepancies between CDM model predictions and small-scale observations (see section 4.1), the field is still open to the possibility of different DM models. Several methods have been developed to solve this puzzle and to determine the properties and the nature of DM. In this section we analyze the main ones.

3.4.1 Strong gravitational lensing

Strong gravitational lensing occurs when the light from a background galaxy is deflected by the gravitational potential of another object. As a result, one observes multiple images of the background galaxy that are highly distorted and magnified. Additional perturbations to the lensed images can be caused by substructures inside the foreground lensing galaxy and low-mass haloes along the line of sight to the background object, the intensity of which is dependent on the mass and the number of these (sub)haloes. As a result, gravitational lensing allows us to directly constrain the halo and subhalo mass functions, which depend on the content and type of dark matter. Various techniques have been developed in order to use gravitational lensing to obtain information on the (sub)halo mass function. Fig. 3.8 shows one such method, in which a lens model is used to reconstruct the observed lensing effects. Subsequently, by analyzing the residual map between model and observation, it is possible to trace the number and/or mass of any sub-structure present in the field.

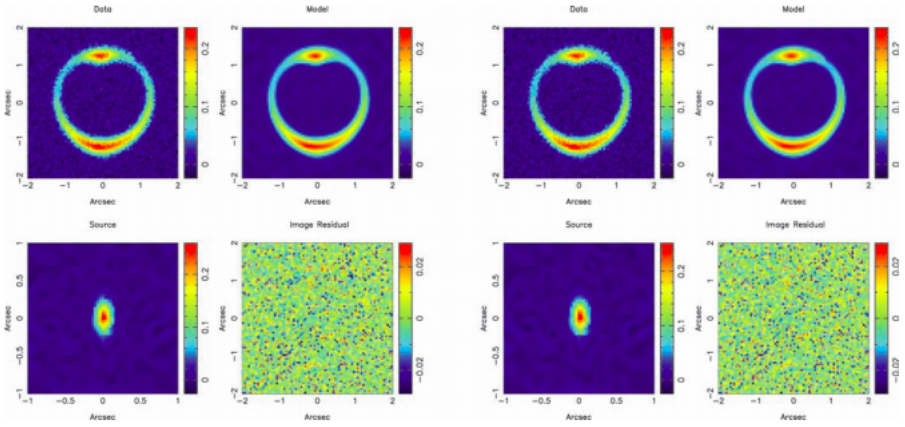

Figure 3.8: *Results of two methods of the non-linear reconstruction for the smooth component of a the perturbed lens. The top right-hand panel shows the original mock data, while the top left-hand panel shows the final reconstruction. On the second row, the source reconstruction (left-hand panel) and the image residuals (right-hand panel). Credits: Vegetti and Koopmans (2009).*

3.4.2 Lyman-α Forest

The study of high-quality optical spectra from Lyman-emitting high-redshift quasars is another astrophysical probe for the nature of DM. At different redshifts, the spectrum of the quasar becomes related to the matter power spectrum as it travels across the Universe. The quasar light, in particular, is redshifted as the Universe expands, thus Lyman-α absorption from neutral hydrogen clouds along the line of sight suppresses portions of the original quasar spectrum. Since the matter power spectrum is dependent on the DM model (see section 3.1.1), the comparison of mock spectra generated from hydrodynamic simulations and those collected from spectroscopic observations can constrain the nature of DM. Murgia et al. (2018) used a Monte Carlo Markov Chain (MCMC) analysis of the entire parameter space impacting the power spectrum reconstructed from high-redshift Lyman-forest data. They used a parametric transfer function

$$T^2(k) = \left[\frac{P(k)_{nCDM}}{P(k)_{CDM}}\right] = [1 + (\alpha k)^{\beta}]^{\gamma}\,, \tag{3.12}$$

where the subscript nCDM indicates non-CDM models. The parameters $\{\alpha, \beta, \gamma\}$ depend on the DM mass. Therefore, it is possible to compare the transfer function predicted by the simulations with the one constructed by observations to have constraints on the nature of the DM (see Fig. 3.9).

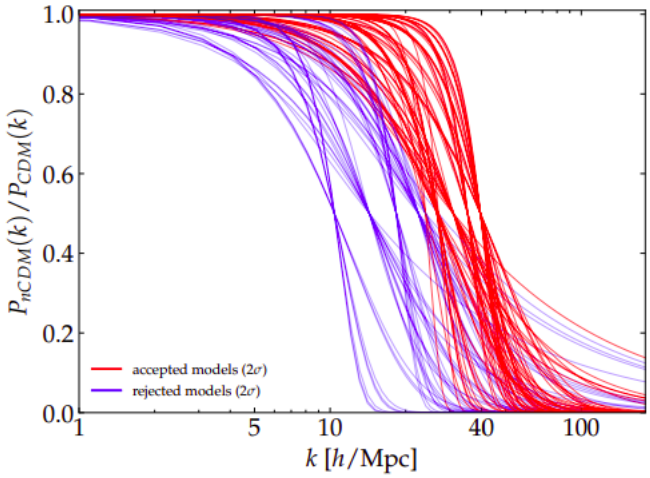

Figure 3.9: *Squared transfer functions associated to the 109 $\{\alpha, \beta, \gamma\}$-combinations, each of them corresponding to a different nCDM model. In red the accepted models by the reference MCMC analysis at 2σ. In blue the rejected ones. Credits: Murgia et al. (2018).*

3.4.3 Milky Way satellites

The Milky Way's (MW) satellite galaxies are effective probes of the underlying dark matter distribution, which is sensitive to the DM particle's mass. In section 3.1.1, we saw that the small-scale cut-off of the power spectrum depends on the DM model. If a DM model has a cut-off on the mass scale of dwarf galaxies, we expect to find only a few structures below the cut-off mass. This makes the MW satellite systems a good candidate for constraining the DM properties: plausible models must create enough substructure to accommodate the number of observable Galactic satellites. Fig. 3.10 shows an example of a simulated luminosity function for MW-type galaxies, in CDM and in a WDM model. Since WDM models have a cut-off at larger physical scales, fewer low-mass structures are expected.

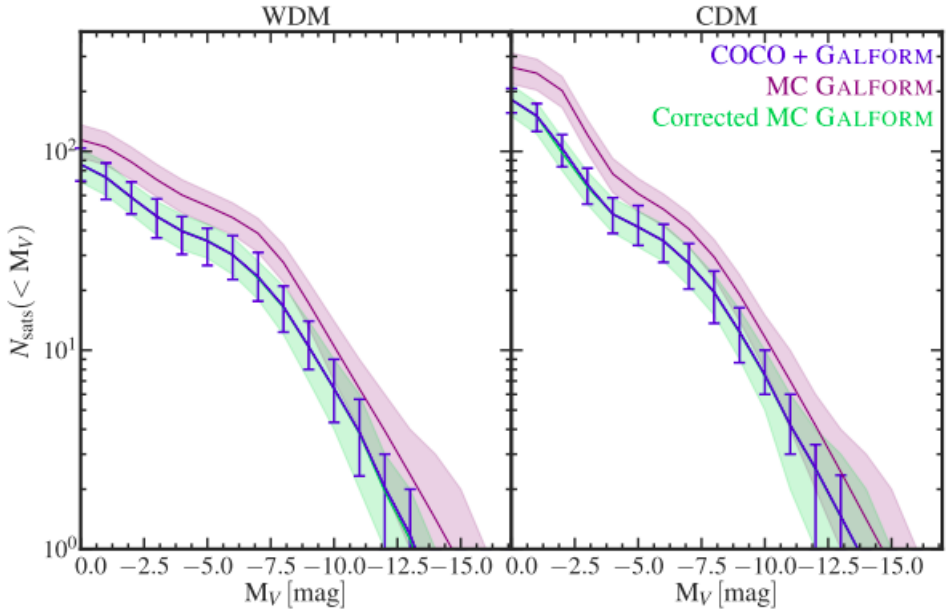

Figure 3.10: *Cumulative satellite galaxy luminosity functions for haloes with masses in the range* $M_{200} = [1, 1.5] \cdot 10^{12} M_\odot$. *Right: 3.3 keV thermal relic WDM model. Left: CDM model. Credits: Newton et al. (2021).*

All these methods are used to put constraints on possible DM models. Recently, Enzi et al. (2021), focusing on WDM models (DM particles that were quasi-relativistic during kinetic decoupling), show how to employ these techniques together to get constraints on the mass of DM particles and therefore rule out some models rather than others (see Fig 3.11). From the analysis of the joint posterior they found an upper limit of $m_{th} = 2.552\, keV^{-1}$, mostly determined by the analysis of MW satellites. The second strongest constraint comes from the Lyman-α forest analysis with an upper limit of $m_{th} = 1.197\, keV^{-1}$. While, for the lensing probes only the SLACS sample (red) puts an

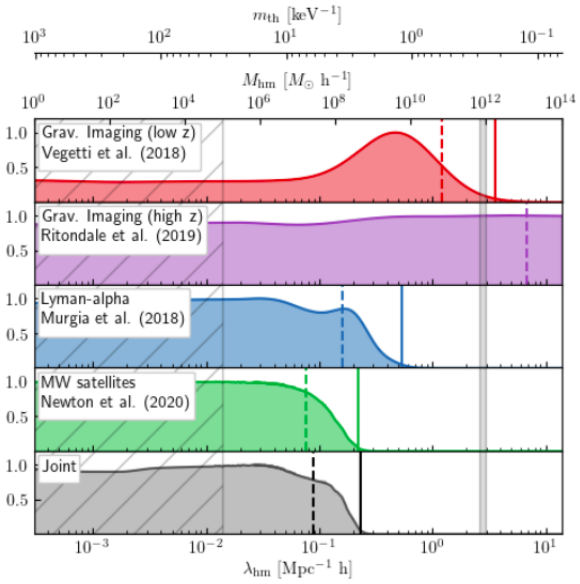

Figure 3.11: *Posterior probability distributions for the analysis of the gravitational lensing (red and purple), the Lyman-α forest data (blue), the luminous satellites of the MW (green) and joint probability (gray). The upper limits from each analysis are represented by vertical solid lines. Credits: Enzi et al. (2021)*

upper limit of $m_{th} = 0.216\, keV^{-1}$, even if it is weaker than the other methods.
The WDM models have been proposed as possible solutions to discrepancies between CDM N-body simulations and observations. In fact, WDM predicts a damped linear power spectrum due to free-streaming leading in a reduction in the number of substructures and forming less concentrated haloes when compared to CDM. These properties suggest that WDM can provide a solution to two of the four main issues related to the CDM paradigm, respectively the missing satellites problem (see section 4.1.1) and the too-big-to-fail problem (see section 4.1.4). However, even if WDM haloes have constant density cores, it has been shown that an unrealistic low value of the WDM mass is needed to create core sizes that match observations (Carucci et al. 2015) and solve the Core/Cusp problem (see section 4.1.2).

Chapter 4

A new Dark Matter model: SIDM

In the standard **ΛCDM** model dark matter is composed by CDM particles, in which gravity is the only dark matter interaction. In fact the success of the CDM model in explaining the observed large-scale structure of the Universe established the current paradigm of structure formation and, as a result, most of our understanding of cosmic structure comes from studies that assume the CDM model. However, significant small-scale discrepancies between the CDM N-body simulations and observations on galactic and sub-galactic scales remain: the so called "CDM small-scale crisis", leading to the hunt for new DM candidates. In this chapter we will discuss the main problems related to the CDM model and we will introduce a new DM model often proposed as a solution: the Self-Interacting Dark Matter models (SIDM).

4.1 CDM small-scale crisis

The standard CDM model has been scrutinized extensively thanks to high-resolution N-body simulations. The model two most crucial predictions are the existence of a large population of DM haloes and subhaloes, and the presence of a sharp cusp in the density profile of dark matter haloes of all masses. These two predictions are linked to four of the CDM model well-known issues: (i) missing satellites; (ii) core/cusp problems; (iii) diversity problem and (iv) too-big-to-fail. We will now describe these in more detail, together with the effect of SIDM on each prediction

4.1.1 Missing satellites

The first issue lies in the number of satellites predicted by N-body simulations for Milky Way-like galaxies. Kauffmann et al. (1993) showed, using CDM-only simulations, that CDM haloes should contain a large number of subhaloes. Similar work was published by Klypin et al. (1999), under the title "Where are the Missing Galactic Satellites?" (from

whence the missing satellites problem gets its name), showed that according to CDM predictions, the MW should have several hundred subhaloes with within its virial radius, each in principle hosting a satellite. However, at the time, only 11 dwarf satellite galaxies were known in the MW. Various solutions to this problem were then offered. One possibility is that the CDM's small subhaloes are ineffective at retaining gas: the ultraviolet photoionizing background can heat the gas, preventing the collapse into DM haloes and reducing the gas cooling rate (Thoul and Weinberg 1995). Moreover, effects due to supernova feedback can also be considered: after an initial star formation episode, supernovae winds could push the remaining gas out of the shallow potential wells of these DM low mass haloes (Dekel and Silk 1986). These two effects could suppress star formation and galaxy evolution, making these sub-haloes invisible to current surveys and thus lessening the missing satellites problem. In fact, it appears that when sophisticated baryon physics is included in simulations (Hopkins et al. 2014; Trujillo-Gomez et al. 2015), the projected number of small satellites drops: supernova feedback and reionization deplete baryons in low mass halos and only a subset of them can form galaxies, reducing the disparity.
As an alternative, Spergel and Steinhardt (2000b) showed that in SIDM cosmology, the sub-halo abundance can be modified for large enough cross-sections. However, the cross-sections required for this to happen are seemingly too large ($\sim 10 cm^2/g$) on galactic scales (at least in DM-only simulations), above the most recent constraints. Although DM self-collisions are not strong enough to impact the power spectrum on galactic scales, another possibility is that the interplay between DM interactions with relativistic particles in the early Universe and DM collisions due to DM self-scattering can create a cutoff in the power spectrum on scales larger than the CDM model (Vogelsberger et al. 2016). This effect can suppress the formation of subhaloes (see section 3.4.3).
In reality, the number of observed faint satellite galaxies has risen considerably since this problem was originally addressed. Due to faintness, luminosity bias, and restricted sky coverage, the finding of numerous faint new satellites in the Sloan Digital Sky Survey suggests that up to a factor of $5-20$ more dwarf galaxies may yet be found. Given these factors, the issue of lost satellites no longer appears to be a major concern.

4.1.2 The core/cusp problem

This second problem is related to the different behavior of the density profiles of some cosmic structures. As explained in section 3.2.1, CDM-only simulations predict haloes with cuspy DM density profiles well-described by NFW profile. However, observational studies have measured the density profiles of structures, ranging in size from dwarf galaxies to galaxy clusters. It has been found that some of these structures have a lower slope in the central regions with respect to predictions with the NFW profile, sometimes leading to a constant density profile in these areas, known as cored system. Solutions to this discrepancy within a CDM framework typically invoke baryonic feedback processes that can alter the DM profile in the inner regions: core formation, for example, might

be driven by sufficiently strong supernova feedback. DM particles can migrate out to larger orbits when a substantial percentage of baryons is rapidly removed from the inner halo. In this way, through a purely gravitational interaction between DM and baryons, recurrent bursts of star formation and outflows might lower the core halo density (Navarro et al. 1996; Ocvirk et al. 2014; T. Sawala et al. 2016).
Another solution is to assume that DM is not collisionless, but it is self-interacting: the interactions between DM particles can form isothermal cores in the central parts of the haloes, as we will discuss in detail in section 4.2 (see also Fig. 4.1).

4.1.3 Diversity problem (of rotation curves)

This issue occurs as a result of the fact that not all observed galaxies appear to have cores: while some systems have large cores, there are galaxies which are consistent with a cuspy CDM halo (Oman et al. 2015). This is in contrast with **ΛCDM** model in which the development of hierarchical structures results in self-similar halos that are well-described by NFW profiles. Because the halo parameters are correlated, specifying a halo with just one parameter is sufficient. For example, the halo density profile is entirely defined at all radii, including the inner density cusp, once the maximum circular velocity V_{max} is fixed, but observed galaxies with similar V_{max} can have significant variation in their central densities. In other dark matter models, the diversity of observed rotation curves is similarly expected, because changing the nature of dark matter may generate cores in DM haloes, but such cores would all be similar at a given mass scale, contrary to what rotation curves suggest.
A solution to this problem can be found if both baryon effects and another DM model are considered. In the presence of baryons, SIDM has been shown to both increase and reduce the central density of DM, depending on how centrally concentrated the baryonic component is, solving both the core/cusp problem and the diversity problem. These results will be discussed in more detail in the next section.

4.1.4 Too-big-to-fail

The presence of large, dense galactic subhaloes whose kinematics looks incongruous with those of the brightest Milky Way satellites in CDM N-body simulations, is commonly referred to as the "too-big-to-fail" (TBTF) problem. Boylan-Kolchin et al. (2011) showed that CDM simulations predict the majority of the Milky Way's most massive sub-haloes to be too dense to host any of the Milky Way's bright satellites. The problem is that these sub-haloes are much more massive than the estimated dwarf galaxy masses based on line-of-sight velocity measurements, hence, these substructures should be too big to fail to form stars. This problem, like the preceding ones, has a slew of proposed solutions inside the **ΛCDM** model that incorporates baryon physics. For example, the loss of baryons due to reionisation, as well as environmental factors like as ram pressure,

gas stripping, and tidal stripping of DM, can reduce the mass of haloes containing dwarf satellite galaxies, yielding conclusions that are compatible with observations. These environmental processes, on the other hand, should not be significant for field galaxies, where a TBTF issue has also been identified (Garrison-Kimmel et al. 2014).
Also in this case SIDM models have been proposed to solve this problem: the reduced central densities in SIDM haloes lower the circular velocity profiles in the inner regions and bring simulated SIDM DM-only systems into better agreement with stellar velocity dispersion measurements, than CDM DM-only simulations.

4.2 Self-Interacting Dark Matter

The **ΛCDM** model assumes that the DM is non-relativistic at decoupling and effectively collisionless, although it is weakly interacting with other particles within the standard model. As discussed in section 3.2, the standard model is in remarkable agreement with a variety of cosmological data on large scales, but its consistency with observations on small-scale is less clear: the **ΛCDM** model has to face the small-scale challenges discussed above. These discrepancies come from comparing data with DM-only simulations, which ignore baryonic effects. As a result, a lot of researches have been conducted to understand whether these differences are due to an incomplete modelling of baryonic physics with the CDM paradigm. However, it is still unclear whether accurately including relevant astrophysics phenomena will be enough to place simulated CDM model in line with observations. Another intriguing possibility is that these differences are revealing something about the nature of DM and it is the CDM model that needs to be revisited. One of the proposed alternatives, first introduced by Spergel and Steinhardt (2000a), is that DM is not collisionless, but that the DM particles can scatter with each other: these models are referred to as *Self-interacting dark matter* models. In comparison to the collisionless case, SIDM models assume a non-zero DM cross-section, that can modify the distribution of DM. These models are expected to produce a wider range of configurations that could solve the small-scale CDM problems, leaving the properties on large scale unchanged. We summarize the expectations for SIDM haloes as follows (see Fig. 4.1):

- **Reduced central density**: The central density is lowered in the presence of self-interaction as low entropy particles are heated within the dense inner halo, transforming the NFW cusp into a core.

- **Spherical halo shape**: While CDM halos are usually triaxial, self-interaction can isotropize DM particle velocities and erase or reduce ellipticity. In comparison to CDM halos, the minor-to-major axis ratio c/a is expected to be closer to unity in the central regions of SIDM haloes.

- **Isothermal velocity dispersion**: Even for virialised CDM haloes, the DM velocity dispersion, which indicates the "temperature" of DM particles, is not constant and decreases towards the center of the halo. Self-interactions transport heat from the DM halo's hotter outer area to its cooler inner region, thermalizing the inner halo and causing the velocity dispersion to be uniform with radius.

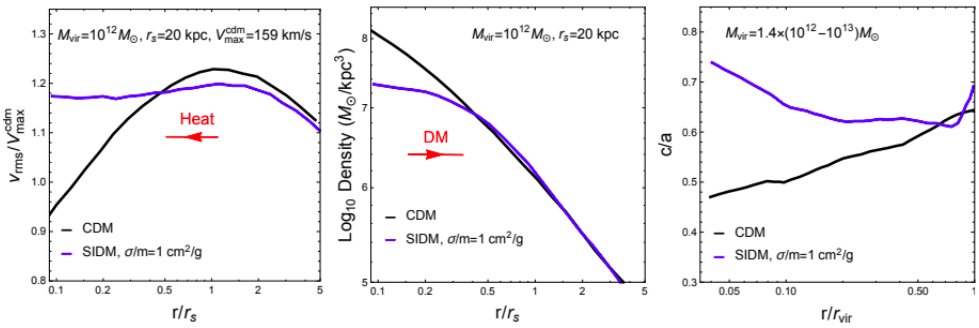

Figure 4.1: *Summary of the main effects of SIDM on halo properties: density profiles (left), dispersion profiles (center), and median halo shapes (right) for SIDM with* $\sigma/m = 1\,cm^2/g$ *and its CDM counterpart. Credit: Tulin and Yu (2018).*

In principle, many models based on SIDM can be built based on strength of the self-interactions and in recent years, simulations and semi-analytical models have been used to place constraints on the allowed SIDM cross-section. The SIDM models can be divided into two large families:

- **Constant cross-section**: the probability of scattering is constant on all scales and depends only on the DM density.
- **Velocity dependent cross-section**: the probability of scattering depends, not only on the density, but also on the relative velocity of the DM particles.

We will now discuss the main evidence in favor of the SIDM model on different scales and the current constraints on the cross-section values.

4.2.1 Dwarf galaxies

It is precisely to solve the Core/Cusp problem in dwarf galaxies that the SIDM model was introduced for the first time. As shown in Fig. 4.2, initial excitement about SIDM model was related to its ability to produce constant density cores in dwarf galaxies: with a cross-section $\sigma/m_\chi \sim 1\,cm^2/g$, the DM interactions produce an isothermal core with a $\mathcal{O}(1kpc)$ size in low-mass galaxies, close to what is apparently observed. As discussed in

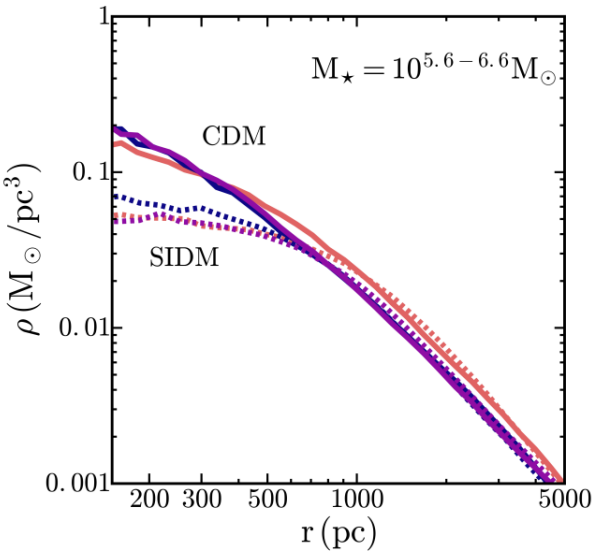

Figure 4.2: *Density profiles of dwarf galaxies in CDM (solid lines) and SIDM (dashed lines). At the center of the CDM galaxies, the densities continue to rise steeply, whereas in SIDM model, the density profiles in central regions flatten to lower densities. Credit: Robles et al. (2017).*

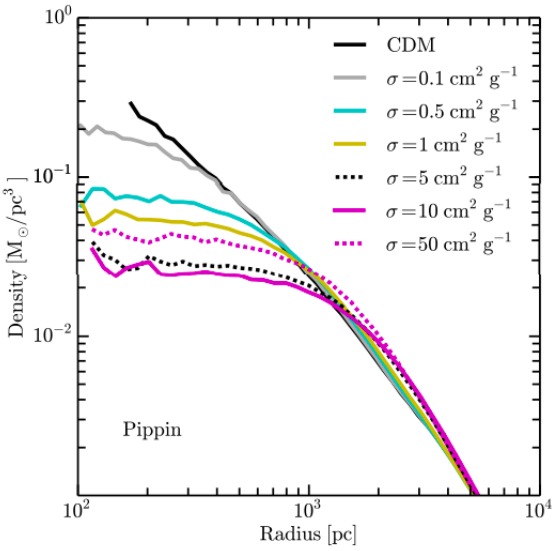

Figure 4.3: *Density profiles of dwarf galaxies in CDM (black line) and different SIDM models. The extent of the core depends on the self-interaction cross section: the larger this value, the larger the core. Credits: Elbert et al. (2015a).*

section 4.1.4, the production of constant density cores also naturally solves the too-big-to-fail problem (Elbert et al. 2015a). The typical core size for SIDM models depends on the cross section: the larger this value, the larger the core (see Fig. 4.3). This relation is not linear, meaning that a cross-sections spanning at least two orders of magnitude ($\sigma/m = 0.5 - 50\,cm^2/g$) can alleviate TBTF problem. They show that, to explain the distribution of DM in dwarf and low-surface-brightness galaxy haloes the cross section must be: $\sigma/m \geq 0.5 cm^2/g$.

4.2.2 Disk and elliptical galaxies

Unlike dwarf galaxies, disk or elliptical galaxies are baryon dominated systems in the central areas. This makes these objects excellent systems for studying the interplay between baryon physics and DM properties. Kaplinghat et al. (2014a) derived an equilibrium solution in SIDM models for the dark matter halo density profile including the gravitational potential of both baryons and dark matter. They showed that the presence of baryons can have a dramatic effect on the predictions for SIDM halo profile with the inner halo shape following the baryonic potential. Small changes in the baryonic component might result in significant changes in the total density profile due to interactions between a baryonic disk and the SIDM halo in which it lives. Sameie et al. (2018a) used isolated N-body simulations to study the response of SIDM haloes ($M \sim 10^{12} M_\odot$) to the presence of baryonic potentials. They showed (see Fig 4.4) that in the presence of baryons, SIDM can both increase and reduce the central density of DM, depending on how centrally concentrated the baryonic component is. SIDM changes the DM density profile in the presence of an extended baryonic disk in the same manner it does for a DM-only scenario, generating a constant density core and lowering the mass in the halo's center (CORED systems). A compact baryonic disk, on the other hand, can contract the DM halo (CUSPY sistems). This contraction increases the rate of scattering, which can become efficient and can transport energy away from the centre of the halo, producing a very dense halo cores (Balberg et al. 2002; Koda et al. 2011). In agreement with these results, Despali et al. (2019) have studied the baryonic effects not in an isolated and idealized scenario, but in full-hydrodynamic zoom-in simulations. They showed that the final properties, such as the density profile, also correlated with the mass accretion history of the halo (these results will be discussed in section 5.3). Moreover, they used mock lensed images created from their simulated haloes in SIDM with $\sigma/m = 1\,cm^2/g$ and in CDM to estimate the Einstein radius r_E. They showed (see Fig 4.5) that in SIDM the median Einstein radius of cored and cuspy systems, once baryonic effects are included, are in practice identical so the bi-modality seen in CDM is in general lost in the SIDM run. As discussed in section 3.4.1, observed properties of lens galaxies can offer a way to discriminate between DM models. Moreover, the shape of elliptical galaxies offers the opportunity to constrain self-interactions in haloes on $10^{12} - 10^{13} M_\odot$. In comparison to triaxial CDM haloes, self-interactions are predicted to make DM haloes more spherical,

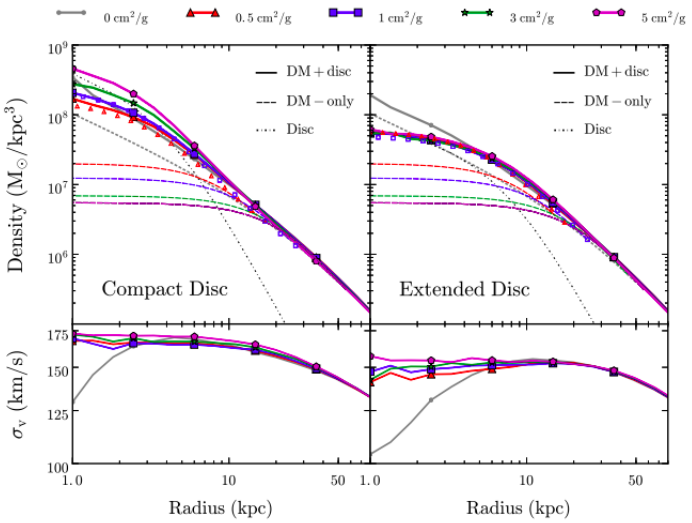

Figure 4.4: *Top: DM density profiles for σ/m = 0 (CDM), 0.5, 1, 3, and 5 cm^2/g in the presence of compact (left) and extended (right) discs. For comparison the profiles in the various models for DM-only simulations are also plotted (dashed lines). Bottom: velocity dispersion profiles for the same models. Credits: Sameie et al. (2018a).*

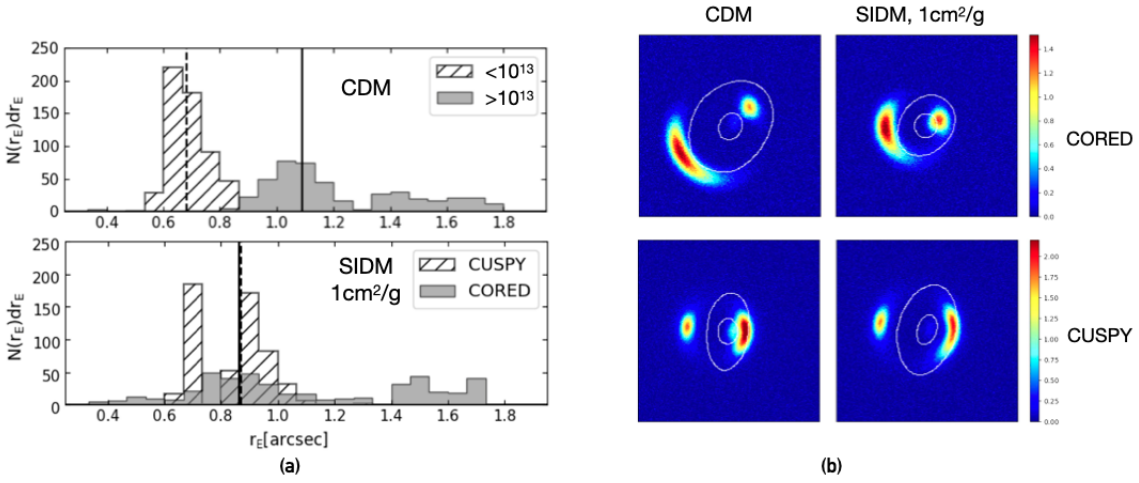

Figure 4.5: *a) Einstein radii distribution in the CDM and SIDM. The vertical lines show the medians for the cuspy and cored haloes and in SIDM these values are superposed. (b) Mock lensed images created from two of the simulated haloes ($z_L = 0.2$), the critical lines (white) are superposed to the surface brightness distribution of the lensed simulated source ($z_S = 1$) Credits: Despali et al. (2019).*

at least in the inner regions where the scattering rate is highest. Studies in this direction have focused on the isolated elliptical galaxy NGC720 ($M_{halo} \sim 7 \cdot 10^{12} M_{\odot}$), based on X-ray shape measurements from the Chandra telescope with the the assumption that one scattering per particle is sufficient to substantially affect the ellipticity of a halo. Buote et al. (2002) showed that the X-ray isophotes remain elliptical at least down to projected radii $\sim 5kpc$ with ellipticity $\epsilon \approx 0.4$. To have constraints on SIDM models from these observations, Peter et al. (2013) showed that the distribution of ellipticities, based on their sample of simulated SIDM haloes with mass $3 - 10 \cdot 10^{12} M_{\odot}$ and with $\sigma/m = 0.1\, cm^2/g$, is precisely consistent with $\epsilon \approx 0.4$ and that even a cross-section $\sim 1\, cm^2/g$ is marginally allowed. However, these results are based on SIDM DM-only simulations, while Sameie et al. (2018a) showed that the baryonic physics can have a strong impact also on the shape and the ellipticities of the halo and are part of the motivation for the work done in this thesis (these results will be discussed in section 6.2).

4.2.3 Galaxy clusters

The rate of DM self-interactions scales with the local DM density and DM particle velocity-dispersion. As a result, more larger systems, like galaxy clusters, also have the potential to be used as probes of DM particle characteristics. The first cosmological simulations at these scales were performed by Yoshida et al. (2000), which studied a single halo ($M = 10^{15} M_{\odot}$) for $\sigma/m = 0.1,\, 1,\, 10\, cm^2/g$. Rocha et al. (2013) more recently ran simulations for $\sigma/m = 0.1,\, 1\, cm^2/g$ at similar sizes but across a significantly larger cosmic region. In terms of volume, the best-resolved halos are between $10^{12} M_{\odot}$ and $10^{14} M_{\odot}$. Both works showed that SIDM haloes with a cross-section $\sigma/m = 1.0\, cm^2/g$, have $\mathcal{O}(100 - 200kpc)$ radius cores and central densities of $\rho_0 \sim 10^{-3} M_{\odot}/pc^3$ on cluster sizes (see top panels in Fig. 4.6).
Strong gravitational lensing data have been used to constrain the core size and density in clusters relevant for SIDM. In this direction, Meneghetti et al. (2001) examined the ability of SIDM haloes to create "extreme" strong lensing arcs, i.e. radial arcs or large tangential arcs, imposing strong constraints on cluster cores. Since these do not occur for SIDM haloes with $\sigma/m = 0.1\, cm^2/g$ or for larger values, they obtained that on cluster scale the cross section must be $< 0.1\, cm^2/g$. This earlier constraint relied on SIDM-only simulations, while Robertson et al. (2019) provided observable quantities of cluster from full-hydrodynamic simulations, producing strong gravitational lensing maps (see Fig. 4.7). They compared the results of their simulations with 19 clusters from the CLASH survey (Postman et al. 2012). They concluded that $\sigma/m < 1\, cm^2/g$ on clusters scale, highlighting the importance of including baryons in simulations with SIDM, both because of the direct effect of the baryonic distribution on observable quantities, and of their indirect effect influencing the structure of DM haloes.

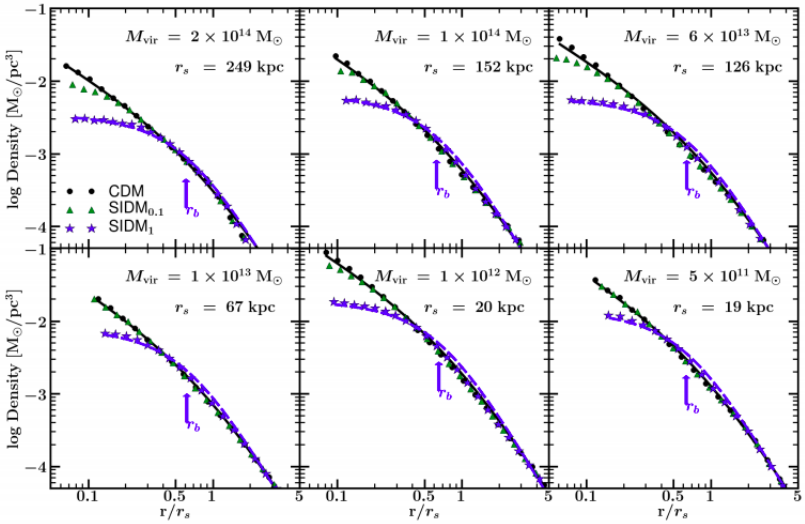

Figure 4.6: *Density profiles of six haloes from SIDM1 (blue stars) and SIDM0.1 (green triangles) simulations and their CDM counterparts. Top: Cluster scales. Bottom : galaxy scales. Credits: Rocha et al. (2013).*

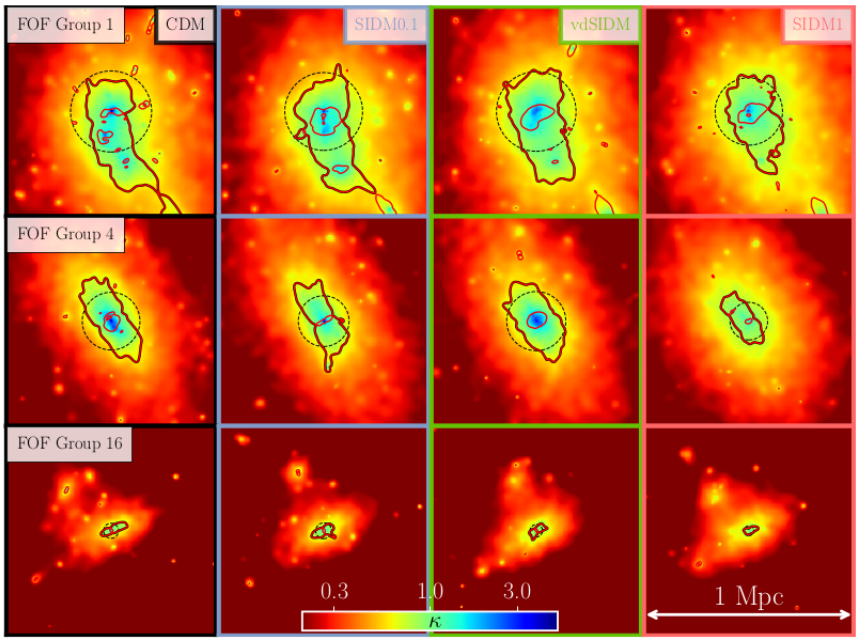

Figure 4.7: *Convergence maps of four FOF groups in the BAHAMAS simulations, with different SIDM cross-sections (with a lens redshift of $z_L = 0.375$ and a source redshift $z_S = 2$). The critical curves are given in red. The dashed circles represent the effective Einstein radius. The scale of each panel covers a field of view of* 1 *Mpc in the lens plane, corresponding to approximately* 3.2 *arcmin. Credits: Robertson et al. (2019).*

4.2.4 Velocity dependent cross-section

If the literature's constraints on σ/m are taken at face value, the door to a velocity-independent cross-section that can address CDM's "small-scale crisis" has been shut. Fry et al. (2015) discovered that cross-sections compatible with cluster scale limitations were unable to appreciably lower the central density of haloes with peak circular velocities less than 30 km/s. As a result, there has been a surge in interest in SIDM models with velocity-dependent cross-sections, i.e a cross-section that decreases with increasing relative velocity. The velocity dependency that emerges in SIDM particle models is analogous to scattering in a Coulomb potential, where the cross-section is $\propto 1/v^4$. Because of this, dwarf galaxies' cross sections can be several orders of magnitude bigger than on cluster sizes. As a result, these models may easily create effects in dwarf galaxies while satisfying all existing galaxy cluster constraints.
Recently, Robertson et al. (2019) run simulations with a SIDM model with a velocity dependent cross-section. This model corresponds to DM particles scattering though a Yukawa potential and is described by 3 parameters: the DM mass m_χ, the mediator mass m_ϕ , and a coupling strength α_χ, so the differential cross-section becomes:

$$\frac{d\sigma}{d\Omega} = \frac{\alpha_\chi^2}{m_\chi^2(m_\phi^2/m_\chi^2 + v^2 \sin\frac{\theta}{2})^2}\,, \tag{4.1}$$

where v is the relative velocity between two DM particles, and θ is the polar scattering angle. Fig. 4.8 shows the trend of the momentum transfer cross-section just defined, compared with other velocity independent cross-section. They show that for this cross-section, the halo density profiles can be approximately reproduced using a velocity-independent and isotropic cross-section.

4.3 N-body simulations

Cosmological simulations are commonly used to simulate the evolution of cosmic structures and assess the impact of dark matter particle phenomenology. N-body codes are used to simulate the development of N gravitationally interacting bodies (stars orbiting in a globular cluster or DM particles) by directly computing the gravitational force on each body from the N-1 other bodies. The simulation progresses by making tiny time leaps, or 'time-steps,' during which the velocities and the positions of particles change depending on the gravitational forces. The starting point to integrate a particle distribution forward in time is an initial state, the initial conditions, which are typically assumed to be in the linear regime defined by perturbation theory. The procedure for creating generic initial conditions may be divided into 4 phases:

1. **Homogeneous N-particles realization**: create a realization of an unperturbed cubic volume of side L by distributing N particles homogeneously in a lattice or

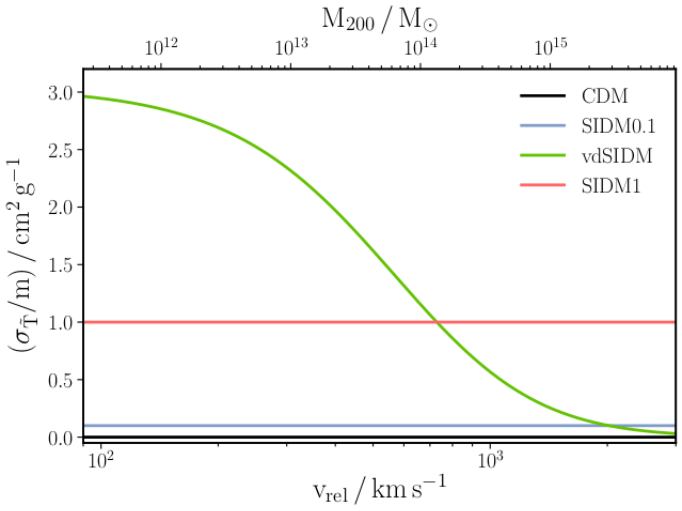

Figure 4.8: *The momentum transfer cross-section for four simulated DM models, as a function of the relative velocity between DM particles. At a velocity scale characteristic to the considered halo $M \sim 10^{14}$, the velocity-independent cross-section is equal to the momentum transfer cross-section of the velocity-dependent one. Credits: Robertson et al. (2019).*

a glass-like configuration, in which the particles are initially placed at random in the simulation cube and then left to evolve under a repulsive force by reversing the sign of the gravitational force until they reach an equilibrium configuration.

2. **Select the power spectrum**: As we have seen (Fig. 3.4), different cosmological models predict differences in the primordial power spectra. So we must choose the desired one.

3. **Add perturbations**: perturbations of wavelength λ down to the Nyquist frequency of the particle distribution are represented by plane waves of spatial frequency in Fourier space, $k = 2\pi/\lambda$. A Gaussian distribution with variance proportionate to the desired linear power spectrum is used to generate amplitudes of these plane waves.

4. **Create the initial density field**: an inverse Fourier transform is then used to get the density field and associated gravitational potential in real space. These fields are used to determine the displacements needed to convert the uniform N-particle distribution (point 1 in this list) into a distribution with the appropriate power spectrum.

Fig. 4.9 shows an illustration of the end results of this procedure. Once the initial conditions are generated, an N-body simulation is performed to follow the evolution of

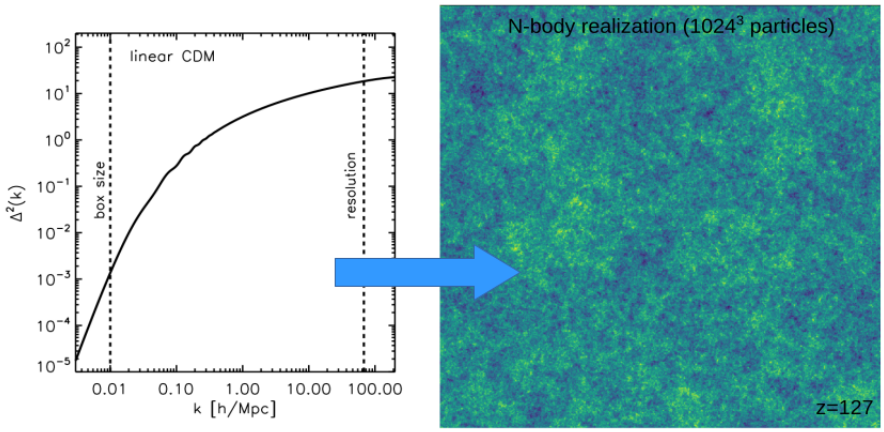

Figure 4.9: *Initial conditions for an N-body CDM simulation. Left: the dimensionless linear CDM power spectrum; the vertical dashed lines show the greatest and smallest scales that may be represented in the initial conditions. Right: dark matter density field generated from the power spectrum on the left at* $z = 127$*, with* $N = 1024^3$ *particles in a cosmological cube of co-moving side,* $L = 40\,Mpc\,h^{-1}$*. Credits: Jesús Zavala and C. S. Frenk (2019).*

the density and velocity fields across all resolved scales. Fig. 4.10 shows an example of the evolution with redshift of the projected CDM dark matter density distribution, in Millennium II simulation (M. Boylan-Kolchin et al. 2009). The evolution follows the hierarchical clustering: structures start to form around density peaks in the initial conditions and become bigger and denser with time.
Due to the different nature of CDM and SIDM, gravity and the interactions between particles are modeled differently in the two cases. Now, we will discuss the equations underlying these implementations: the Collisionless Boltzmann Equation and the Collisional Boltzmann Equation.

4.3.1 The Collisionless Boltzmann Equation

In the case of non-relativistic and collisionless particles, i.e. CDM, N-body simulations follow the evolution of the dark matter phase-space distribution function, $f(\vec{r}, \vec{v}, t)$, given by the collisionless Boltzmann equation (CBE) coupled with the Poisson equation for the gravitational field: $\Phi(\vec{x})$. To define CBE, we introduce the mass of DM contained in a volume d^3r centered in $\vec{r}$, with velocity in the velocity-space element d^3v centred on $\vec{v}$ as :

$$dM = f(\vec{r}, \vec{v}, t) d^3r d^3v \,, \tag{4.2}$$

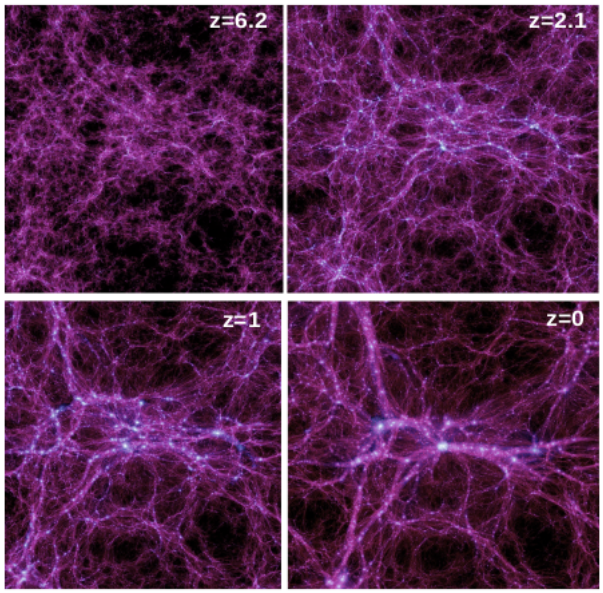

Figure 4.10: *Evolution of the projected dark matter density field in a box of side length $L = 100 Mpc\, h^{-1}$ from the Millennium II simulation. The redshift corresponding to each snapshot is shown on the top right. Credits: M. Boylan-Kolchin et al. (2009).*

where $f(\vec{r}, \vec{v}, t)$ is the DM's distribution function in the phase space. Considering the non-collisional case, from the Liouville's Theorem

$$\frac{df}{dt} = 0\,, \tag{4.3}$$

where the derivative in this case represents the Lagrangian derivative, then

$$\frac{df}{dt} = \frac{\partial f}{\partial t} + \frac{\partial f}{\partial \vec{r}} \cdot \frac{d\vec{r}}{dt} + \frac{\partial f}{\partial \vec{v}} \cdot \frac{d\vec{v}}{dt} = 0\,, \tag{4.4}$$

but $d\vec{r}/dt = \vec{v}$ and $d\vec{v}/dt = -\nabla\Phi$, so

$$\frac{\partial f}{\partial t} = -\vec{v} \cdot \nabla f + \nabla\Phi \frac{\partial f}{\partial \vec{v}}\,. \tag{4.5}$$

This is known as the Collisionless Boltzmann equation, which is coupled with the Poisson equation

$$\nabla^2\Phi = 4\pi G \int f d^3v\,. \tag{4.6}$$

Assuming that DM is the only species, and thus makes the only contribution to the gravitational potential, equations (4.5) and (4.6) describe the evolution of the DM fluid. However this method would be highly inefficient, so N-body simulations use a Monte

Carlo technique: the smooth distribution function $f(\vec{r}, \vec{v}, t)$ is discretized as an ensemble of N phase-space elements or "particles", $\{\vec{r}_i\ ,\ \vec{v}_i\}$, with $i = 1, ..., N$, each with its own mass m_i, position $\vec{r}_i$, and velocity $\vec{v}_i$. Then over any phase-space volume V

$$\int_V f(\vec{r}, \vec{v}, t)\, d^3r d^3v = \left\langle \sum_{(\vec{r}_i, \vec{v}_i) \in V} m_i \right\rangle . \tag{4.7}$$

With this discretization, calculating the development of the phase-space distribution in an N-body simulation is reduced to tracking the dynamics of a system of N particles according to the potential obtained from the particle distribution.
Moreover, using the Poisson equation, it is possible to calculate the potential from the masses and locations of the N particles. The linearity of the equation means that the potential at $\vec{r}_i$ is just the sum of the potentials at $\vec{r}_i$ from all other particles in the system :

$$\Phi(\vec{r}_i) = -\sum_{j \neq i} \frac{G m_j}{|\vec{r}_i - \vec{r}_j|} . \tag{4.8}$$

As particles approach one another, this potential diverges, resulting in high gradients, and therefore enormous accelerations. As a result, it is standard practice to 'soften' the gravitational potential, such that the force between two particles decreases as the distance between them approaches zero. Then defining ϵ, the 'gravitational softening length', equation (4.8) becomes

$$\Phi(\vec{r}_i) = -\sum_{j \neq i} \frac{G m_j}{(|\vec{r}_i - \vec{r}_j|^2 + \epsilon^2)^{1/2}} . \tag{4.9}$$

Softening decreases the forces in near contacts, allowing for longer time steps than a potential that has not been softened. It also gives a better estimate of the forces that would exist if the matter distribution were smooth instead of being discretized in N particles.

4.3.2 Collisional Boltzmann Equation

The collisionless Boltzmann equation (CBE) explains the development of a collisionless fluid like CDM. However, if dark matter cannot be treated as CDM, the fundamental equations need to be modified. In case of non-relativistic but no longer collisionless dark matter, as in SIDM, the collisionless Boltzmann equation must be replaced with the full collisional Boltzmann equation. It includes an extra term (the collisional operator) in the right-hand side to account for the effect of dark matter collisions according to a self-scattering cross-section. We can write the collisional Boltzmann equation, adding a term that describes these collisions :

$$\frac{df(\vec{r}, \vec{v}, t)}{dt} = \Gamma_{in} - \Gamma_{out} , \tag{4.10}$$

where the term Γ_{out} accounts collisions in which a particle at location $\vec{r}$ and velocity $\vec{v}$ scatters from another particle and so changes its velocity, whereas the term Γ_{in} accounts collisions that result in a particle with velocity $\vec{v}$ when it previously had another velocity. If the interacting particles are spherical rigid bodies of radius r, they will interact if they are within $d = 2r$ of one other. As a result, the cross-section for particle interactions is $\sigma = \pi(2r)^2$. A particle traveling at $\vec{v}$ across a stationary background of similar particles will scatter at a rate of

$$\Gamma = n\sigma v\,, \tag{4.11}$$

where n is the particle number density. Now if we consider the case where the background particles have a certain velocity distribution $f_v(\vec{r}, \vec{v})$, then a particle at $\vec{r}_i$ with velocity $\vec{v}_i$ will scatter at a rate

$$\Gamma_i(\vec{r}_i, \vec{v}_i) = \int f_v(\vec{r}_i, \vec{v})\rho(\vec{r}_i)\frac{\sigma}{m}|\vec{v}_i - \vec{v}|\, d^3v\,. \tag{4.12}$$

This relation gives the rate of scattering for individual particles, where σ/m is the cross-section per unit mass, rather than the cross-section of individual particles. The aim, however, is to include scattering into an N-body code, where the scattering rate per particle is already a valuable statistic. As a result, to calculate scattering probabilities within an N -body simulation, f_v and ρ are estimated from the volume within a distance h_{SI} of a particle's position. Where h_{SI} is called scatter search radius. Then, to estimate the scattering rate from particles encompassed in the search region, all neighboring particles must contribute equally to the estimation of f_v and ρ, regardless their position inside the search region. The number of particles inside the search zone will be $N = 4/3\pi h_{SI}^3 n$ for a local number density n. Then it is possible to compute the scatter rate as a sum over the N neighbor particles:

$$\Gamma_i = \sum_{j=1}^{N} \frac{\sigma|\vec{v}_i - \vec{v}_j|}{(4/3)\pi h_{SI}^3}\,. \tag{4.13}$$

Therefore the probability of two particles, i and j, separated by a distance $d < h_{SI}$, scattering within a time step Δt, may be calculated as follows:

$$P_{ij} = \frac{\sigma|\vec{v}_i - \vec{v}_j|}{(4/3)\pi h_{SI}^3}\Delta t\,. \tag{4.14}$$

4.4 The GADGET code

In this section we will describe the main algorithms for the calculation of gravitational forces and for the implementation of the SIDM models, used in the GADGET software. This is a software for N-body cosmological simulations written by Volker Springel at the Max Planck Institute for Astrophysics. A more complete description can be found in

Robertson (2017) and Springel (2005).
To compute the effective gravitational force, a direct sum of the forces operating on all particle pairs in a simulation with N particles, would need $N(N-1)/2$ individual force computations. This is not feasible in a reasonable period of time for simulations with billions of particles, thus alternatives to direct summation are used. A tree or a particle mesh are two typical solutions to this problem. GADGET makes use of both, so we will go through them both here.

- **Particle mesh**: This algorithm begins by computing a gridded density field, which is created by assigning the mass of the particles on to a grid. Then in this case, the Poisson equation can be solved in Fourier space:

$$-|\vec{k}|^2\Phi(\vec{k}) = 4\pi G\rho(\vec{k})\,. \tag{4.15}$$

  The gravitational forces are calculated in Fourier space converting the gridded density and solving equation (4.15) before conducting an inverse Fourier transform. From the gradient of Φ, it is possible to calculate the gravitational forces. This technique is quick, and it also includes periodic boundary constraints, which are necessary for cosmological simulations. One drawback is that the resolution is restricted by the size of the grid used to calculate density and potential.

- **Tree**: This hierarchical method divides the simulation box into sub-regions, which are then divided into sub-regions, and so on, until each region has one or no particles. This division is done in GADGET using an octree, see Fig. 4.11, which divides each cubic area into eight equal-sized octants. When calculating the forces on a particle, close particles can have their forces computed directly, while sets of more distant particles included in a sub-region can have their forces estimated using the mass within the sub-region at the centre-of-mass of the sub-region itself. The algorithm starts at the root node and works the way up the tree to compute the force on a particle. If a node's centre of mass is sufficiently enough away from the particle for which the forces are being calculated, all particles inside the associated cell are considered as a single particle with mass equal to the total mass within the cell and located at the cell's centre of mass. While the algorithm continues to descend the tree, if the node is not sufficiently far away.

GADGET, as previously stated, employs both techniques, dividing the force computation into a long and short-range component. A tree is used to compute short-range forces, while a mesh with a set cell size is used to calculate long-range forces. In this way the computation remains fast without losing in terms of resolution.

4.4.1 Velocity dependent cross-section

These simulations employ the SIDM model with a velocity dependent cross-section defined in M. Vogelsberger and Jesus Zavala (2013). These models are well-motivated by

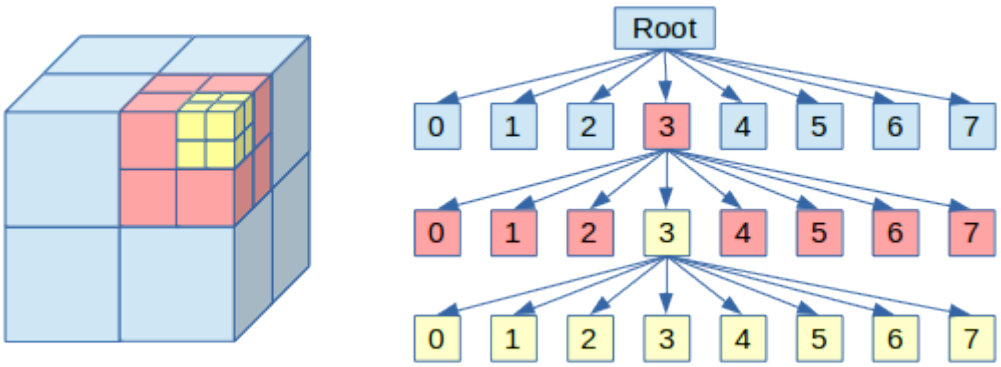

Figure 4.11: *On the left, a graphic of an octree shows how the physical simulation volume is split into octants, and on the right, how this may be stored in a tree structure. The mass within the simulation box and the box's center of mass are contained in the root node of the tree, which is followed by eight connections to its daughter nodes. Credits: David (2017)*

particle physics, and they represent the elastic scattering transfer cross-section mediated by a new gauge boson with mass m_Φ. As a result, an attractive Yukawa potential with coupling strength α_c emerges. For these interactions, the the momentum-transfer cross-section can be approximated by

$$\frac{\sigma_T}{\sigma_T^{max}} \propto \begin{cases} \beta^2 \ln(1+\beta^{-1}) & \beta < 0.1 \\ \beta^2(1+1.5\beta^{1.65})^{-1} & 0.1 < \beta < 10^3 \\ (\ln\beta + 1 - 1/2(\ln\beta)^{-1})^2 & \beta > 10^3 \end{cases} \tag{4.16}$$

where $\beta = \pi v_{max}^2/v^2$, and v_{max}^2 is the velocity at which $\sigma_T v$ peaks. As the velocity v approaches zero, this cross-section diverges, enhancing scattering in low mass haloes (with average velocities smaller than v_{max}) over the constant cross-section scenario, while for $v >> v_{max} \rightarrow \sigma_T \propto v^{-4}$ so the scattering rate in these DM haloes is strongly suppressed. These simulations adopt the values of σ_T^{max} and v_{max} to maximize the self-interaction rate at the typical velocity dispersion of Milky Way dwarf spheroidals:

$$\begin{cases} v_{max} = 30\,km/s \\ \sigma_T^{max}/m = 3.5\,cm^2/g \end{cases} \quad DM-only \tag{4.17}$$

$$\begin{cases} v_{max} = 10\,km/s \\ \sigma_T^{max}/m = 35\,cm^2/g \end{cases} \quad DM + baryons \tag{4.18}$$

4.4.2 GADGET system of units

GADGET employs comoving coordinates in cosmological simulations, as well as velocities and time intervals that differ from those used in non-cosmological simulations. The comoving coordinates $\vec{x}$, are related to the physical coordinates $\vec{r}$ through the following relation

$$\vec{r} = a(t)\vec{x}\,. \tag{4.19}$$

From this, we can define the physical velocity,$\vec{v}$, and peculiar velocity, v_p

$$\vec{v} = \dot{\vec{r}} = \dot{a}\vec{x} + a\dot{\vec{x}} = \dot{a}\vec{x} + \vec{v}_p\,. \tag{4.20}$$

The internal positions in GADGET are comoving, so it is possible to define

$$Pos \equiv \vec{x}\,, \tag{4.21}$$

$$Vel \equiv a^2\dot{\vec{x}}\,. \tag{4.22}$$

The units used in GADGET are set in the parameter file, with default values:

$$U_M = 10^{10} M_\odot = 1.989 \cdot 10^{33} g = \hat{U}_M\, g\,, \tag{4.23}$$

$$U_L = 1kpc = 3.085 \cdot 10^{21} cm = \hat{U}_L\, cm\,, \tag{4.24}$$

$$U_V = 1km\, s^{-1} = 10^5 cm\, s^{-1} = \hat{U}_V\, cm\, s^{-1} \tag{4.25}$$

and the unit of time

$$U_T = U_L U_V^{-1} = 3.085 \cdot 10^{16} s = 0.979 Gyr\,. \tag{4.26}$$

GADGET uses also the following definitions

$$Hubble \equiv 100\, km\, s^{-1}\, Mpc^{-1}\, U_T\,, \tag{4.27}$$

$$E(a) \equiv \sqrt{\Omega_M a^{-3} + \Omega_\Lambda + (1 - \Omega_M - \Omega_\Lambda) a^{-2}}\,, \tag{4.28}$$

then

$$H(a) = h\, U_T^{-1}\, Hubble\, E(a)\,. \tag{4.29}$$

Chapter 5

Density Profiles

In the previous chapter, we described the main properties of SIDM models and their implementation in simulations. SIDM models can address both the too-big-to-fail and the core-cusp problems at the scale of dwarf galaxies if the self-scattering cross-section is $\sim 1\,cm^2\,g^{-1}$ (Zavala et al. 2013). Furthermore, it has been demonstrated that SIDM with a constant cross section $\sim 3\,cm^2\,g^{-1}$ can explain a wide range of galaxy rotation curve morphologies while being compatible with observations of galaxy clusters (Kamada et al. 2017)[1]. However, it is worth mentioning that the majority of prior research was based on dark-matter-only simulations, ignoring the interplay of self-interactions and baryonic physics. Kaplinghat et al. (2014b) discovered through analytic calculations that thermalization may considerably enhance the SIDM central density in baryon-dominated systems, with the inner halo shape matching the baryonic potential. This is not surprising, since even in the context of CDM, the inclusion of baryons can significantly alter the halo properties. Thus, in this chapter we will calculate and analyze the density profiles of haloes using both DM-only and full-hydrodynamic simulations to test what are the main differences between the CDM model and SIDM models, and how baryon physics impacts the properties of these profiles. Previous work, on the impact of baryonic effects on these models, focused on zoomed simulations of individual haloes, while the aim of this project is to extend and test their results using a full cosmological box.

5.1 Simulation

The simulations used in this work have been run with the Gadget3 code and are part of the extended family of EAGLE simulations. The EAGLE simulations are cosmological hydrodynamic simulations of galaxy formation, that include sub-grid physics models for gas cooling, star formation, and feedback from both stars and active galactic nuclei.

[1]They found that even a cross-section $\sigma/m = 1\,cm^2\,g^{-1}$ is in good agreement with the brightest galaxies.

The simulations are run with the cosmological parameters taken from the most recent Planck results (Aghanim et al. 2020), listed in Tab. 5.1. Different box sizes are available,

Cosmological parameters	**Value**
Ω_M	0.307
Ω_Λ	0.693
Ω_b	0.0482
σ_8	0.8288
n_s	0.9611
h	0.6777
Y	0.248

Table 5.1: *Cosmological parameters used in the EAGLE simulations: Ω_M, Ω_Λ and Ω_b are the average densities of total matter, dark energy, and baryonic matter in units of the critical density at $z = 0$; σ_8 is the square root of the linear variance of the matter fluctuations; n_s is the scalar power-law index of the power spectrum of primordial adiabatic perturbations and Y is the primordial abundance of helium.*

each with a different resolution, and Tab. 5.2 highlights the key features of each box. For details on these simulations and baryon physics implementations see Schaye et al. (2015).

Name	$L(cMpc)$	N	$m_g(M_\odot)$	$m_{DM}(M_\odot)$	$\epsilon(kpc)$
L025N0376	25	376^3	$1.81 \cdot 10^6$	$9.70 \cdot 10^6$	0.70
L025N0752	25	752^3	$2.26 \cdot 10^5$	$1.21 \cdot 10^6$	0.35
L050N0752	50	752^3	$1.81 \cdot 10^6$	$9.70 \cdot 10^6$	0.70
L100N1504	100	1504^3	$1.81 \cdot 10^6$	$9.70 \cdot 10^6$	0.70

Table 5.2: *The main characteristics of EAGLE simulations. The columns from left to right show: simulation name; comoving box size; number of dark matter particles (there are originally an equal number of baryonic particles); initial baryonic particle mass; dark matter particle mass; Plummer-equivalent gravitational softening length. Particle properties were recorded for 29 snapshots between $z = 20$ and $z = 0$.*
Credits: Schaye et al. (2015)

We will work with a simulation set made of 6 runs in total, which simulate the same volume of $V = 50\,cMpc^3$ (L050N0752), in CDM and two SIDM models: one with constant cross section $\sigma/m = 1\ cm^2g^{-1}$ (SIDM1) and one with a velocity- dependent cross section (vdSIDM); moreover, for each of those both a DM-only and a full-hydro version are available, allowing us to study the effect of baryons and alternative dark matter at the same time. From now on, we will label the full-hydrodynamic simulation run with a 'b', so we will have: CDMb, SIDM1b and vdSIDMb; together with their DM-only counterpart. These models have already been used in Robertson et al. (2018) to look at the density profiles of clusters of galaxies in CDM and SIDM models and in Bondarenko et al. (2021) to analyze how the predictions in SIDM scale in different mass ranges.

5.2 Halo identification

Haloes are identified by the Friends-of-Friends (FOF) algorithm using all dark matter particles and adopting a dimensionless linking length, $b = 0.2$ (Davis et al. 1985). We have selected haloes with masses M_{200} in the range between $10^{12}\,M_\odot h^{-1}$ and $10^{14}\,M_\odot h^{-1}$, at $z = 0$, for all 6 models available; M_{200} is defined by counting the mass within a sphere of radius, R_{200} , for which

$$\frac{3M_{200}}{4\pi R_{200}^3} = 200\rho_c(z)\,, \tag{5.1}$$

where $\rho_c(z) = 3H^2(z)/8\pi G$. Thus the halo boundary is defined by the radius at which the density drops below $200\rho_c(z)$.
We have chosen this mass range for two reasons:

1. to resemble and to have a direct comparison with observed elliptical galaxies that are the main systems for studying the effects of strong gravitational lensing: it has been shown in previous works that this regime might be especially influenced by the inclusion of baryons and that this could influence the lensing signal in terms of Einstein radius distribution (Despali et al. 2019).

2. the mass of the DM particles in these simulations is $m_{DM} = 9.70 \cdot 10^6 M_\odot$, thus this resolution does not allow us to study small systems such as dwarf galaxies.

In Fig. 5.1 we plot the halo mass distribution for each simulation. From these histograms we immediately notice that in none of the 6 cases there are haloes with $\log(M_{200}/M_\odot h^{-1}) > 13.5$, because of the box size of $50\,Mpc$ and that the distributions of the halos follow the same trend: the number of halos decreases as the virial mass increases, as predicted by hierarchical clustering. We split our sample into mass bins in order to compare and average the features of halos of comparable mass. To have a sufficient number of haloes for each bin, we divide our sample into 3 groups:

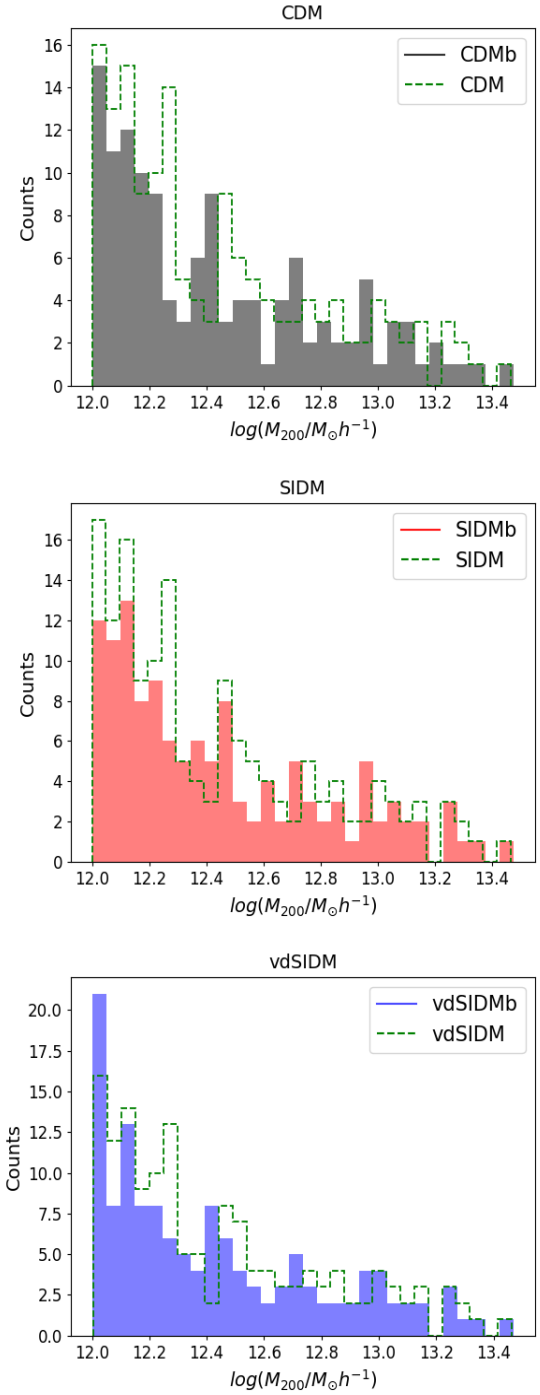

Figure 5.1: *Distributions of the number of halos as a function of virial mass at $z = 0$ for our 6 runs. The filled histograms are the distributions in full-hydrodynamic simulations. The empty histograms refer to DM-only simulations*

$12.0 < \log(M_{200}/M_{\odot}h^{-1}) < 12.5$ (Group 1), $12.5 < \log(M_{200}/M_{\odot}h^{-1}) < 13.0$ (Group 2) and $13.0 < \log(M_{200}/M_{\odot}h^{-1}) < 13.5$ (Group 3). Tab. 5.3 shows the relative number of haloes for each bin and for each model.

	Total	**Group 1**	**Group 2**	**Group 3**
CDM	153	99	37	17
CDMb	129	83	32	14
SIDM1	154	99	38	17
SIDM1b	128	83	32	13
vdSIDM	149	94	38	17
vdSIDMb	133	87	31	15

Table 5.3: *Number of halos for the 3 bins in mass and the 6 simulations used (both DM-only and full-hydrodynamic simulations).*

5.2.1 Impact of baryon feedback on the total halo mass

Looking at the total number of halos for each simulation in Tab. 5.3, we note that in all cases the number of halos in hydrodynamic simulations is lower than the counterpart in DM-only. This phenomenon can be attributed to baryon feedback effects: previous work has revealed that feedback has a substantial impact on low and intermediate halo masses compared to the corresponding haloes in DM-only simulations. Cui et al. (2012) and Sawala et al. (2013) found that baryonic effects can suppress halo masses by up to 25% for halo masses below $10^{13}M_{\odot}$ (in DM-only simulations). Schaller et al. (2015) conducted similar analysis using EAGLE simulations: they built the halo mass function for DM-only simulations and for full-hydrodynamic simulations, shown in Fig. 5.2. Thus they showed that, in the mass range that we are considering in this work, the number of haloes in full-hydrodynamic simulations is about 15%-20% lower than the number of haloes in DM-only simulations. These results are in agreement with what we find: the suppression is 16% and 17% for CDM and SIDM1 respectively, while for vdSIDM we find that this percentage drops to 11% (still within the errors found by M. Schaller). At these masses AGN feedback can still expel baryons, leading to a decrease in the total mass of the haloes, especially for the less massive ones, bringing these haloes out of the range that we selected. Thus the change in the halo mass functions due to baryon effects are similar in all the considered models, consistently with the fact that all simulations were run with the same baryonic physics model calibrated on CDM.

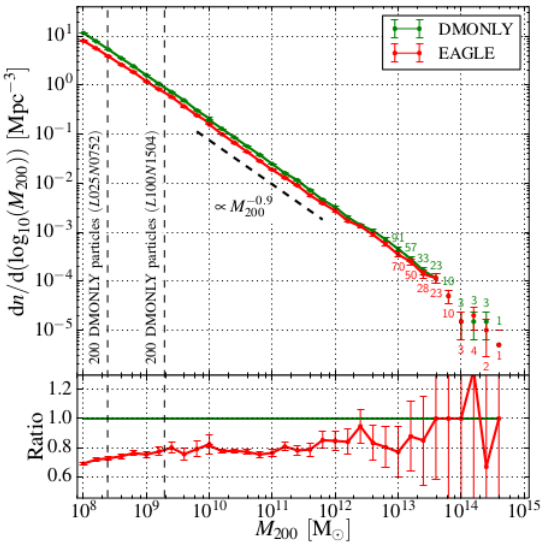

Figure 5.2: *Top: the abundance of haloes at $z = 0$ as a function of the mass, in the full-hydrodynamic (red curve) and DM-only (green curve) simulations. The vertical dashed lines on the left represent the resolution limits for both simulations, and the number of halos in sparsely populated bins is provided above the Poisson error bars. Bottom: ratio of the mass functions in the full and DM-only simulations. Credits: Schaller et al. (2015)*

5.3 Constant cross-section

The influence of self-interactions on DM density profiles has been the driving force behind the idea of SIDM. The primary effect is a decrease in the DM density in the central regions of a halo when compared to its CDM equivalent (see section 4.2, Fig. 4.1 and Fig.4.2). This effect can be reversed in the presence of a dense baryonic component by slowing down the timescale on which haloes undergo core-collapse, also known as 'gravothermal collapse' or the 'gravothermal catastrophe' (Sameie et al. 2018b). For this reason in this section, we will focus on comparing the results in the CDM and SIDM1 models and analyzing what happens when the baryons are also considered.
We start by calculating the spherically-averaged density profiles of the individual haloes for each of the 4 runs here considered. We divide the halo into logarithmically-spaced spherical shells, calculate the number of particles present in each shell and multiply this number by the mass of a DM particle, thus finding the total mass of each shell $M_{tot}(sh)$; therefore the density in each shell becomes $\rho(sh) = M_{tot}(sh)/V(sh)$. In the case of CDMb and SIDMb, in addition to the contribution of dark matter, gas and star particles are also considered. From the profiles for each halo, we calculate the average profile in every mass Groups described in the previous section. We use the Einasto profile

(Einasto 1965) to fit the mean radial density distribution, defined as

$$\rho(r) = \rho_{-2} \ \exp\left\{-\frac{2}{\alpha}\left[\left(\frac{r}{r_{-2}}\right)^{\alpha} - 1\right]\right\}, \tag{5.2}$$

where r_{-2} and ρ_{-2} are the radius and the density at which $\rho(r) \propto r^{-2}$ and α defines the steepness of the power law. Because it can produce varied inner slopes, the Einasto profile is a suitable match for both the CDM and SIDM haloes. Both the NFW and Einasto profiles are reasonable fits for CDM haloes, but the NFW profile is not a good match for cored SIDM haloes; self-interaction creates a wider range of profile configurations, necessitating a more flexible model for the profile. For a meaningful comparison, we use the Einasto profile for all our 4 models. Tab. 5.4 shows the best fit parameters for these models. In Fig. 5.3 we plot the $z = 0$ spherically-averaged density profiles fitted

		Group 1	**Group 2**	**Group 3**
CDM	ρ_{-2}	$(4.34 \pm 0.66) \cdot 10^6$	$(3.90 \pm 0.72) \cdot 10^6$	$(2.32 \pm 0.34) \cdot 10^6$
	r_{-2}	19.96 ± 1.51	30.73 ± 2.68	51.68 ± 3.23
	α	0.26 ± 0.02	0.28 ± 0.03	0.23 ± 0.02
CDMb	ρ_{-2}	$(1.31 \pm 0.39) \cdot 10^7$	$(7.44 \pm 2.36) \cdot 10^6$	$(3.60 \pm 1.06) \cdot 10^6$
	r_{-2}	11.18 ± 1.75	20.51 ± 3.32	38.01 ± 5.29
	α	0.15 ± 0.02	0.14 ± 0.03	0.12 ± 0.02
SIDM1	ρ_{-2}	$(2.42 \pm 0.33) \cdot 10^6$	$(1.87 \pm 0.27) \cdot 10^6$	$(1.21 \pm 0.14) \cdot 10^6$
	r_{-2}	28.13 ± 1.75	47.85 ± 2.80	81.58 ± 3.52
	α	0.39 ± 0.03	0.46 ± 0.04	0.47 ± 0.03
SIDM1b	ρ_{-2}	$(1.89 \pm 0.67) \cdot 10^7$	$(7.35 \pm 2.18) \cdot 10^6$	$(2.41 \pm 0.70) \cdot 10^6$
	r_{-2}	9.56 ± 1.75	20.97 ± 3.18	46.34 ± 6.21
	α	0.14 ± 0.02	0.15 ± 0.02	0.13 ± 0.02

Table 5.4: *Best fit parameters with Einasto profile for the 3 mass Groups for each simulation, where ρ_{-2} is expressed in $M_\odot h^{-1}/(kpc/h)^3$, r_{-2} in kpc/h and α is dimensionless. The errors represent 1 standard deviation.*

with the Einasto profile for all models. For all three Groups, looking at the simulated profiles in DM-only CDM and SIDM (black and red dotted lines respectively), we note that in SIDM, haloes form a core in the central parts, as expected. Also looking at the ρ_{SIDM}/ρ_{CDM} ratio for DM-only (bottom panels), we see that for radii $r \leq 10\,kpc/h$ this ratio is always less than unity: the density in the central areas of the SIDM profiles is lower by more than 50% compared to the CDM profiles.
However, if we want to compare the predictions from simulations with observations, we also need to take into account baryon effects. In all three cases the addition of baryons

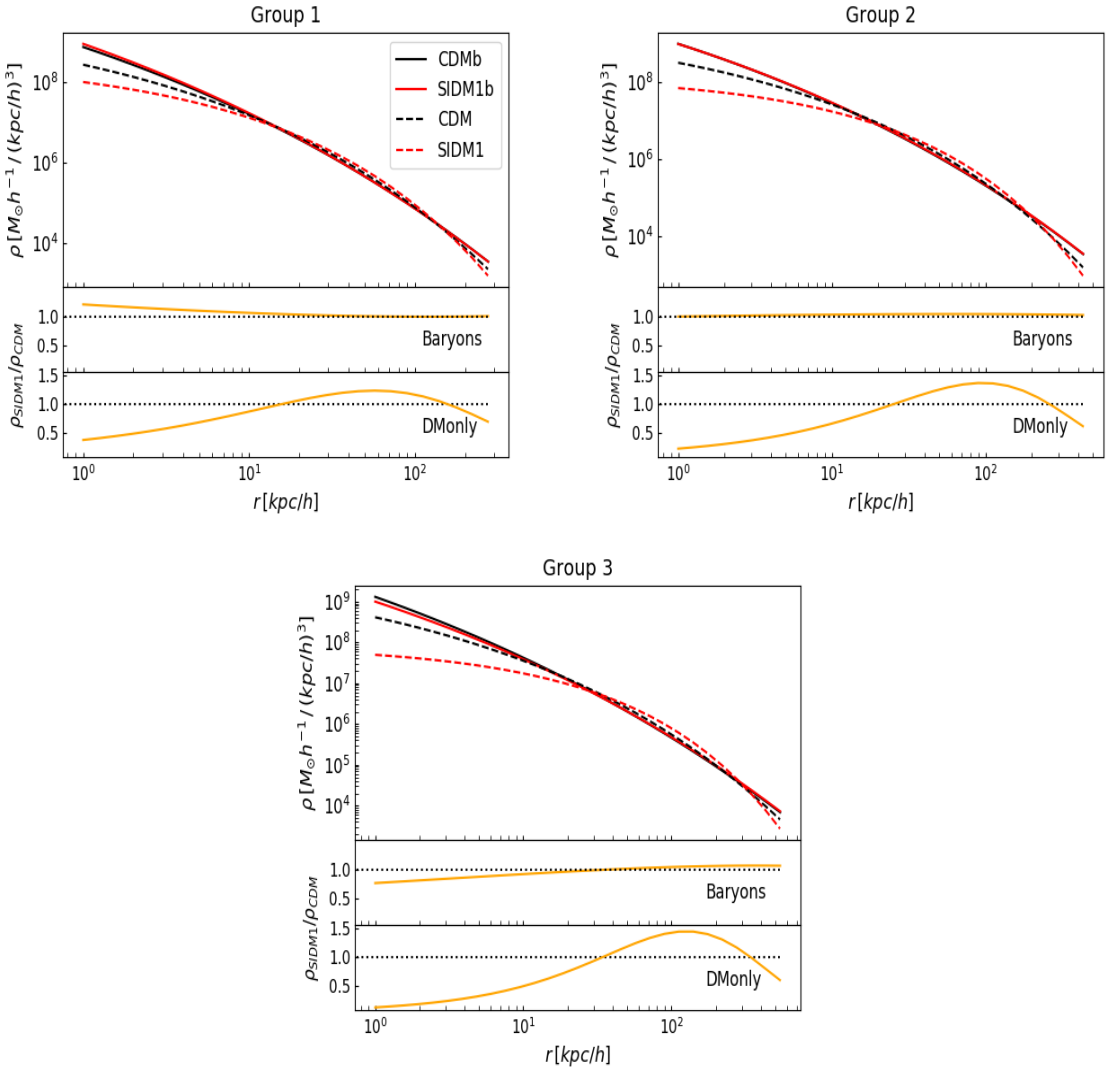

Figure 5.3: *Top: Density profiles with CDM and SIDM models for both DM-only (dashed lines) and full-hydrodynamic (solid lines) simulations, at $z = 0$. Bottom: ratio between the total and the DM-only profiles in the two models: ρ_{SIDM}/ρ_{CDM}. The first density value is calculated at $r = 1\,kpc/h$, therefore above the spatial resolution (softening length $\epsilon = 0.7\,kpc/h$), for this reason this scale is not represented in these plots. Group 1:* $\log(M_{200}/M_{\odot}h^{-1}) \in [12.0, 12.5]$*, Group 2:* $\log(M_{200}/M_{\odot}h^{-1}) \in [12.5, 13.0]$ *and Group 3:* $\log(M_{200}/M_{\odot}h^{-1}) \in [13.0, 13.5]$.

increases the density in the central regions of the haloes compared to DM-only runs. This effect is higher for SIDM, implying that baryons reduce the differences between the two DM models: in fact, in simulations with baryons, the ρ_{SIDM}/ρ_{CDM} ratio (middle

panels) approaches 1, implying that the profiles in the two models become more similar, even though not identical. Moreover, we observe differences in the trends of the profiles in SIDM for the three Groups:

- **Group 1**: In the central regions the SIDM1b profile has a higher density than that of CDMb, with $\rho_{SIDM}/\rho_{CDM} > 1$. However, in these regions the difference between the two models drops to less than 20%.
- **Group 2**: the difference between the two density profiles begins to disappear and the profiles are almost overlapping ($\rho_{SIDM}/\rho_{CDM} \sim 1$).
- **Group 3**: the situation is reversed and the profile of SIDMb has a lower density than the profile of CDMb ($\rho_{SIDM}/\rho_{CDM} < 1$), but also for this Group the difference between the two DM models is less then 20%.

For an easier visualization, Fig. 5.4 shows a zoom of the core regions with the addition of the standard deviation for each point. The profiles follow the trends discussed above even within one standard deviation.
As we already expected, we found that in DM-only simulations all SIDM haloes produce a central core in the density profile that is always below the profiles of CDM haloes in these regions. However, when the average density profiles are calculated by adding the baryon component, the situation changes: only Group 1 exhibits a cored profile, meaning that the SIDM profile lies below the CDM profile; Group 2 has similar profiles in both models; Group 3, on the contrary, has a cuspier profile in SIDM than in CDM, meaning that, in this case, the SIDM profile has higher central densities than CDM. These results are in agreement with what Despali et al. (2019) found. They simulated 9 haloes with virial masses ranging in our mass range and finding that in the central regions:

- SIDM haloes with $M_{vir} > 7 \cdot 10^{12} M_{\odot}$ have higher density profiles than their CDM counterpart, called CORED systems.
- SIDM haloes with $M_{vir} < 5 \cdot 10^{12} M_{\odot}$ have a lower density profiles than their CDM counterpart, called CUSPY systems.

These differences are attributed to different evolutionary histories of the considered haloes: the CORED systems experience a fast accretion phase at low z (late assembly), while the CUSPY systems have a more regular history (early assembly). Therefore, they found a correlation between the mass accretion history and the properties of the final density profile: for CUSPY systems the baryons drive the evolution of the central dark matter core, created at an earlier time (early assembly systems) by the DM self-interaction and then the interplay between baryons and dark matter leads to the final cuspy profile; while the CORED systems were formed at low z (late assembly systems) and thus we see them at the stage in which central core is just established. In Fig. 5.5,

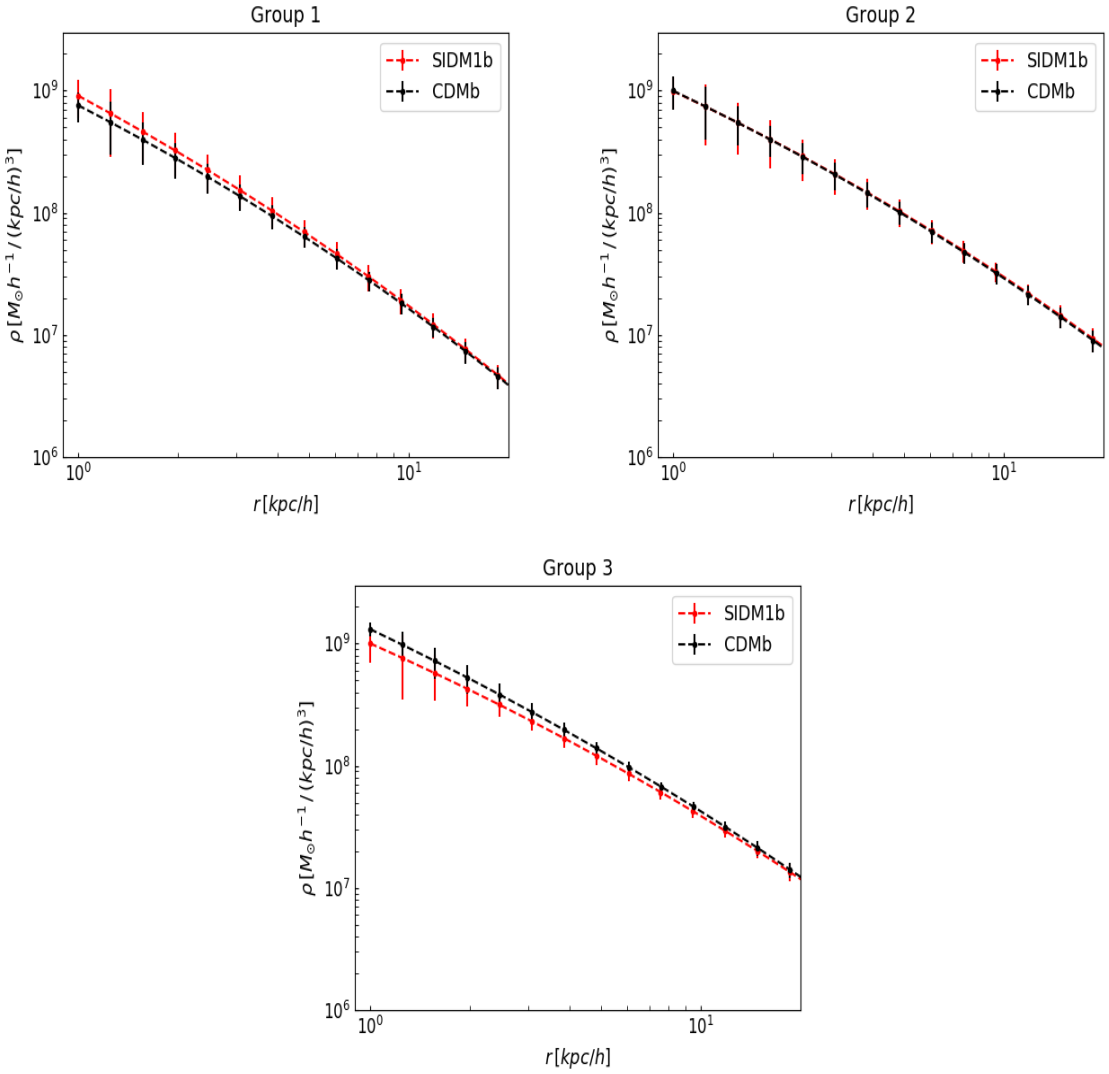

Figure 5.4: *Zoom of the central parts of the density profiles for the three Groups, for both SIDM1b and CDMb. The error bars represent 1 standard deviation for the two models. The dotted lines represent the best fit for the two models (same as in Fig.5.3).*

we plot the density profiles of the DM component of the three Groups both in the DM-only and full-hydrodynamic simulation to understand if the baryons can have an effect also on the DM distribution. The bottom panels show the ratio ρ_{full}/ρ_{only} between DM density in full-hydrodynamic simulations and in DM-only once; in both models the addition of baryons modifies the distribution of dark matter by increasing its central density, but this effect is stronger for SIDM1:

- **CDM**: $\rho_{full}/\rho_{only} < 1.5$ for each Group. (Left panel)

- **SIDM1**: $\rho_{full}/\rho_{only} > 4.0$ for each Group. (Right panel)

This result suggests that a reliable comparison with the data demands accurate baryon distributions in the simulated haloes and that this condition applies not only to the total (DM + baryon) density profile, but also to the DM density, since adiabatic contraction might cause the DM density to rise as the gas cools towards the halo's center (Gnedin et al. 2004). However it remains to be understood how the self-interaction between DM particles can make this effect stronger than in the collisionless case.

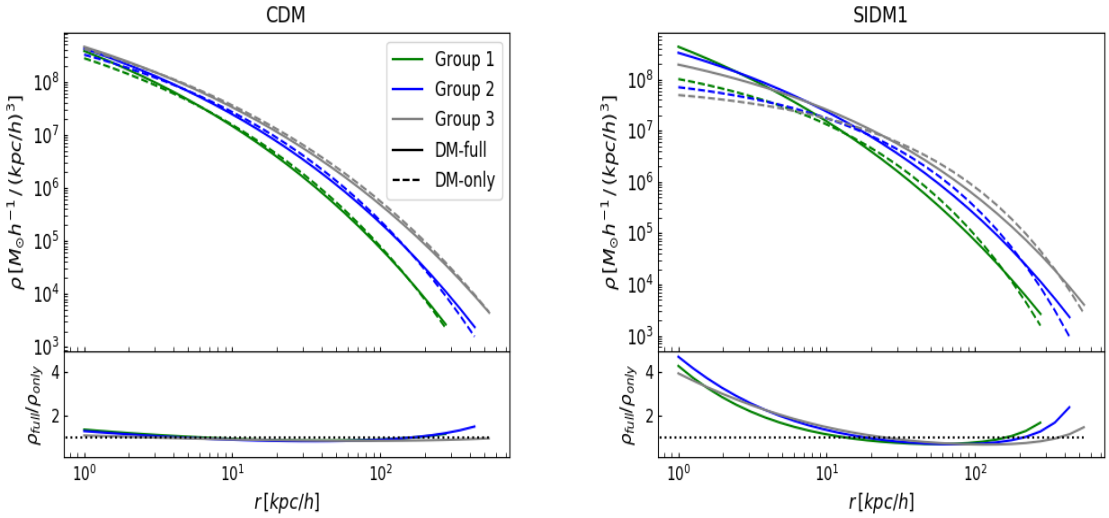

Figure 5.5: *Top: DM density profiles in the three groups both for DM-only(dashed lines) and full-hydrodynamic (solid lines) simulations. Bottom: ratio between DM density in full-hydrodynamic simulations ρ_{full} and density in DM-only simulations ρ_{only}. On the right in the CDM model, on the left in the SIDM1 model.*

5.4 Velocity dependent cross-section

In this section we will analyze the halo density profiles for the SIDM model with a velocity-dependent cross-section (vdSIDM). We follow the same procedures carried out in the case of SIDM with constant cross section: the average profiles of each Group are fitted with an Einasto profile. Tab. 5.5 shows the best fit parameters for these models. In Fig. 5.6 we plot the $z = 0$ spherically-averaged density profiles fitted with the Einasto profile from full-hydrodynamic simulations (vSIDMb and CDMb models) as well as the density profiles from DM-only simulations (vdSIDM and CDM models). Looking at the profiles for the three Groups, we see the same trends as in the case of the SIDM1 model (constant cross section): vdSIDM DM-only simulations have a core in the inner region

		Group 1	Group 2	Group 3
vdSIDM	ρ_{-2}	$(2.04 \pm 0.28) \cdot 10^6$	$(1.61 \pm 0.22) \cdot 10^6$	$(1.12 \pm 0.14) \cdot 10^6$
	r_{-2}	31.09 ± 1.84	52.13 ± 2.88	85.70 ± 3.77
	α	0.43 ± 0.04	0.50 ± 0.04	0.50 ± 0.03
vdSIDMb	ρ_{-2}	$(1.91 \pm 0.67) \cdot 10^7$	$(8.48 \pm 2.84) \cdot 10^6$	$(2.37 \pm 0.67) \cdot 10^6$
	r_{-2}	9.42 ± 1.72	19.66 ± 3.4	45.98 ± 6.00
	α	0.14 ± 0.02	0.16 ± 0.03	0.13 ± 0.02

Table 5.5: *Best fit parameters with an Einasto profile for 3 mass Groups for vdSIDM and vdSIDMb simulations, where ρ_{-2} is expressed in $M_\odot h^{-1}/(kpc/h)^3$, r_{-2} in kpc/h and α is dimensionless. The errors represent 1 standard deviation.*

for every mass Group, meaning that also vdSIDM haloes have lower densities than the CDM counterparts, while with the addition of baryons these differences become much smaller and they vary from one Group to another in the same way as the SIDM1 model. As a final comparison, Fig. 5.7 shows the density profiles for all 6 runs. The three plots on the left show the average profiles in DM-only simulations, while those on the right show the average profiles in full-hydrodynamic simulations for each mass bin. While in the case of DM-only simulations, the average density profiles of the two SIDM models exhibit differences at small radii, with the vdSIDM model having lower densities than the SIDM model, when we study the same average profiles with the addition of the baryons also these differences are canceled and the profiles in the two models overlap, meaning that at these scales the velocity-dependent cross-section with the interplay with baryons acts like the constant one. These results are in agreement with what A. Robertson found on the average profiles on the scale of galaxy clusters (see section 4.2.4). Therefore, also in this case the addition of baryon physics has a strong impact on the properties of the average haloes of SIDM, making the differences between the various models less evident. All results discussed so far are based on profiles averaged across three mass ranges and fitted with an Einasto profile (model dependent), but it is possible that individual haloes may behave differently. For this reasons in section 5.5, we will investigate some single halo to see how the different DM models impact their density profiles.

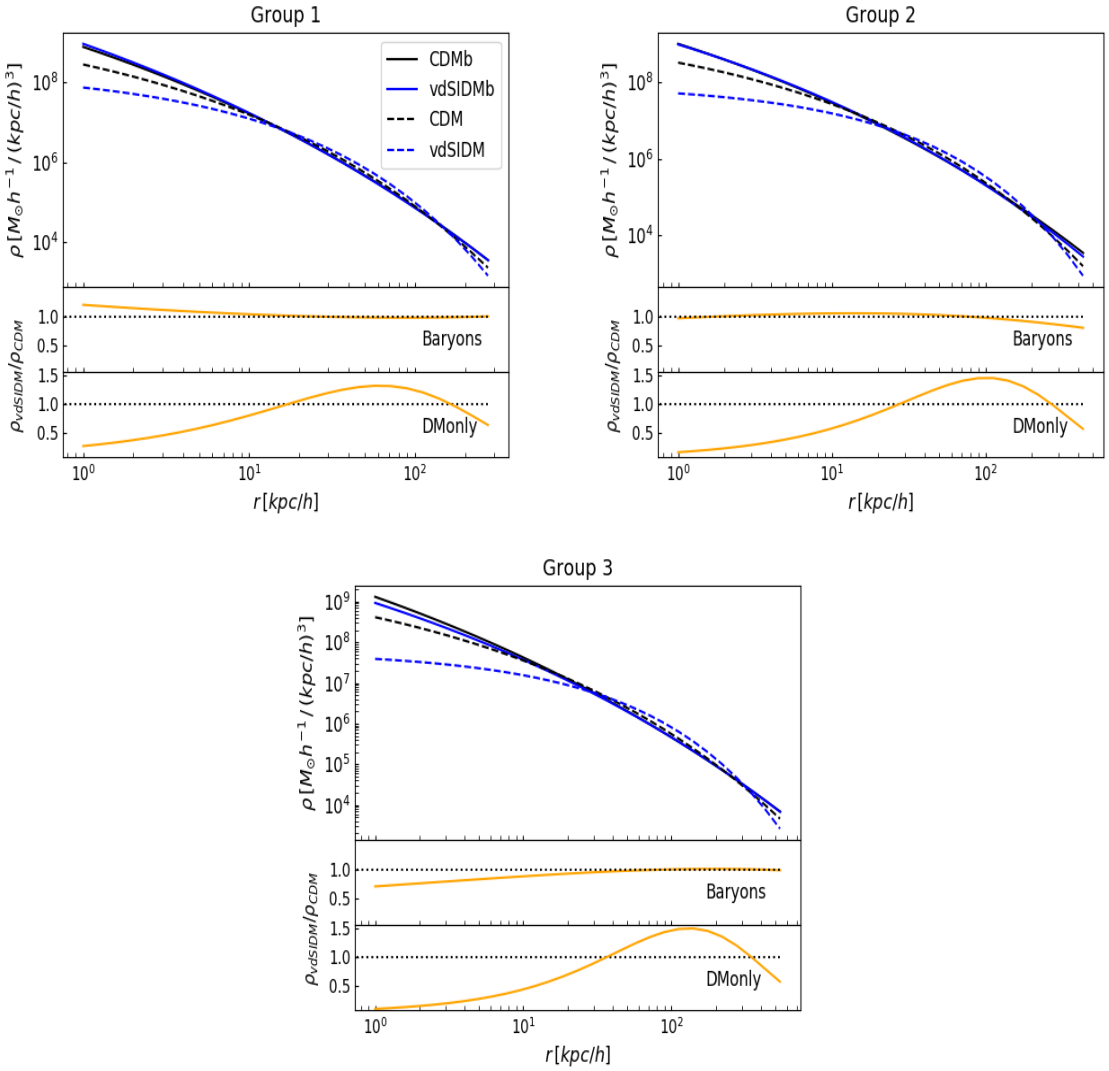

Figure 5.6: *Top: Density profiles with CDM and vdSIDM models for both DM-only and full-hydrodynamic simulations, at $z = 0$. Bottom: ratio between the total and the DM-only profiles in the two models: ρ_{vdSIDM}/ρ_{CDM}. The first density value is calculated at $r = 1\,kpc/h$, therefore above the spatial resolution (softening length $\epsilon = 0.7\,kpc/h$), for this reason this scale is not represented in these plots. Group 1:* $\log(M_{200}/M_{\odot}h^{-1}) \in [12.0, 12.5]$, *Group 2:* $\log(M_{200}/M_{\odot}h^{-1}) \in [12.5, 13.0]$ *and Group 3:* $\log(M_{200}/M_{\odot}h^{-1}) \in [13.0, 13.5]$.

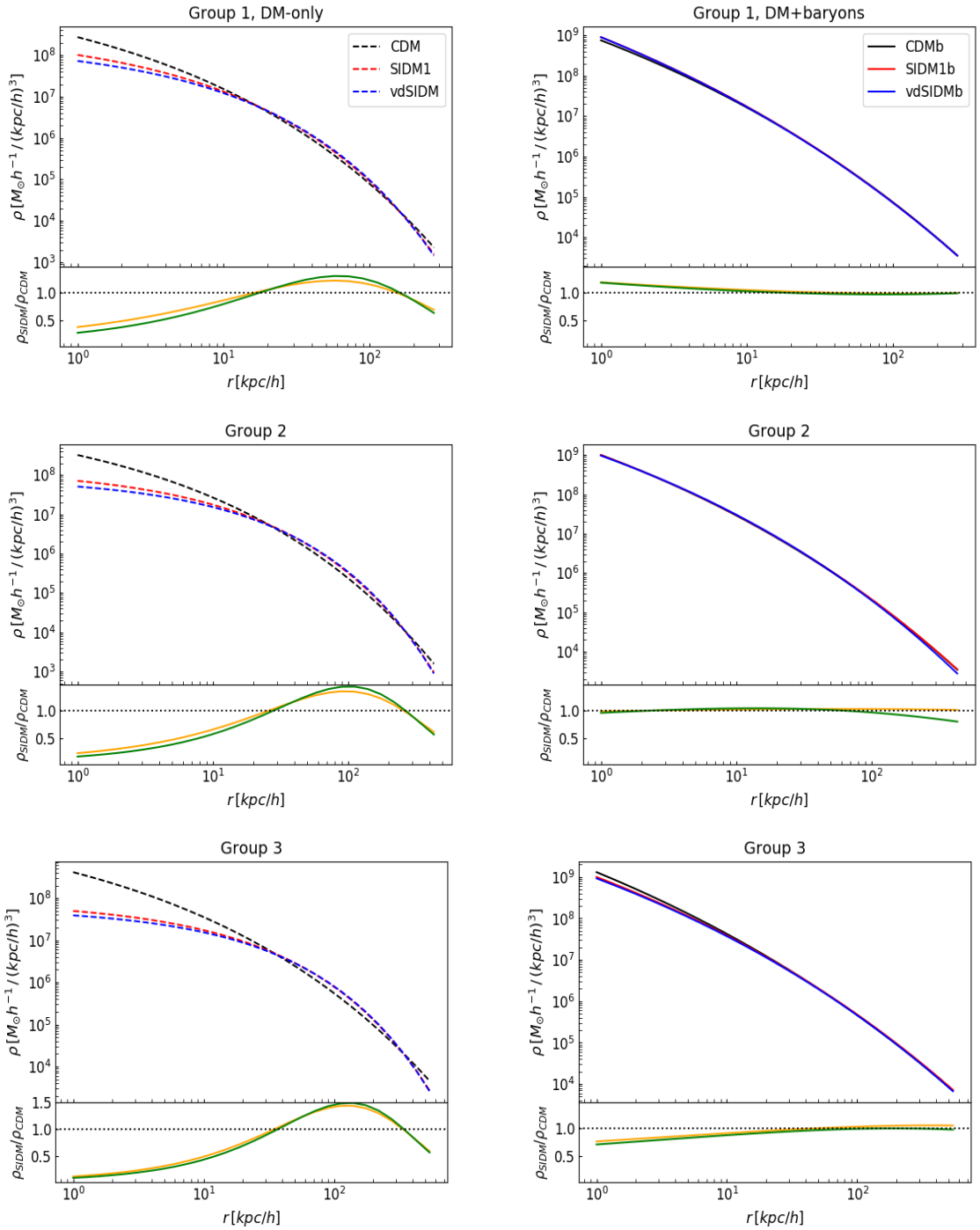

Figure 5.7: *Top: Density profiles for the models considered in each 3 mass Groups. Left: profiles in the DM-only simulations. Right: profiles in the full-hydrodynamic simulations for the corresponding Groups. Bottom: Density ratio between profiles in SIDM and CDM; ρ_{SIDM1}/ρ_{CDM} (orange); ρ_{vdSIDM}/ρ_{CDM} (green).*

5.5 Matched Haloes

In this section, we match the systems between the different runs in order to compare their density profile. This is possible because all the simulations have been run starting from the same initial conditions and thus the large scale perturbations are expected to be the same in all models. To select the matched systems, we use the position of the center of mass. We consider the minimum distance between the haloes centers of mass in the different simulations d_{min} and the virial radius of each halo: haloes are matched if $d_{min}/r_{vir} < 1$. Fig. 5.8 shows the results obtained with this method both in the DM-only case and for the full-hydrodynamic simulations. Most of the halos are distributed on the

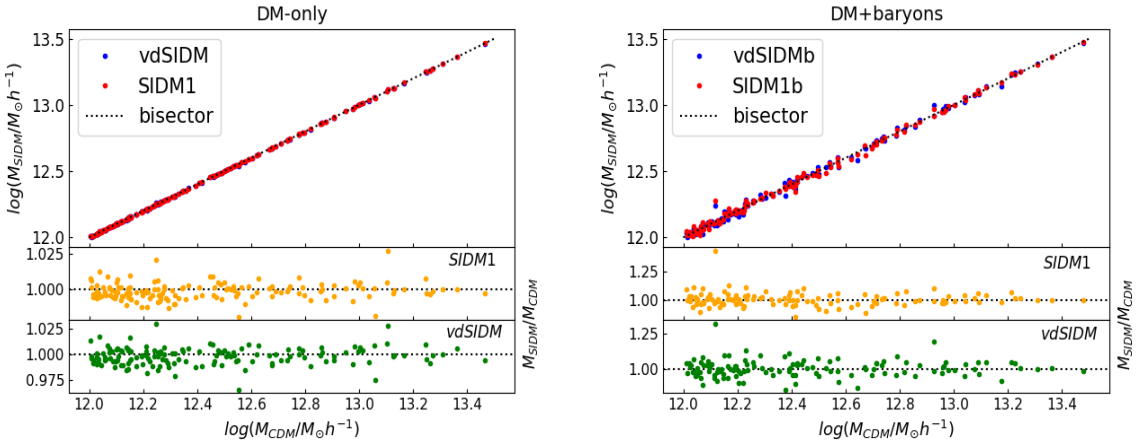

Figure 5.8: *Top: Masses of matched systems in DM-only simulations (left) and full-hydrodynamic simulations (right); in blue matched system between CDM and vdSIDM, in red matched systems between CDM and SIDM. The black dotted line represents the bisector: if the matched systems have the same mass they are distributed on this line. Middle:* M_{SIDM1}/M_{CDM}*. Bottom;* M_{vdSIDM}/M_{CDM}*.*

bisector, with a greater scatter in the case of full-hydrodynamic simulations. Analyzing the ratios (middle and bottom panels), we note that no trend is generated as a function of the halo mass: the haloes in the three models preserve their mass.
Using the matched systems for the three DM models, in Fig. 5.9 we plot a zoom of the central regions of the density profiles of some individual haloes. The haloes are sorted in ascending order of mass and selected so that two haloes belong to each mass Group. We highlight the value of the mass of the matched systems on each figure. The vertical line (twice the value of the softening length) denotes the point below which the influence of the simulation resolutions can affect the density values of single haloes. Moving from the less to the more massive halo, the trend found for the average profiles is confirmed: the less massive haloes tend to be CUSPY, while the more massive ones tend to be

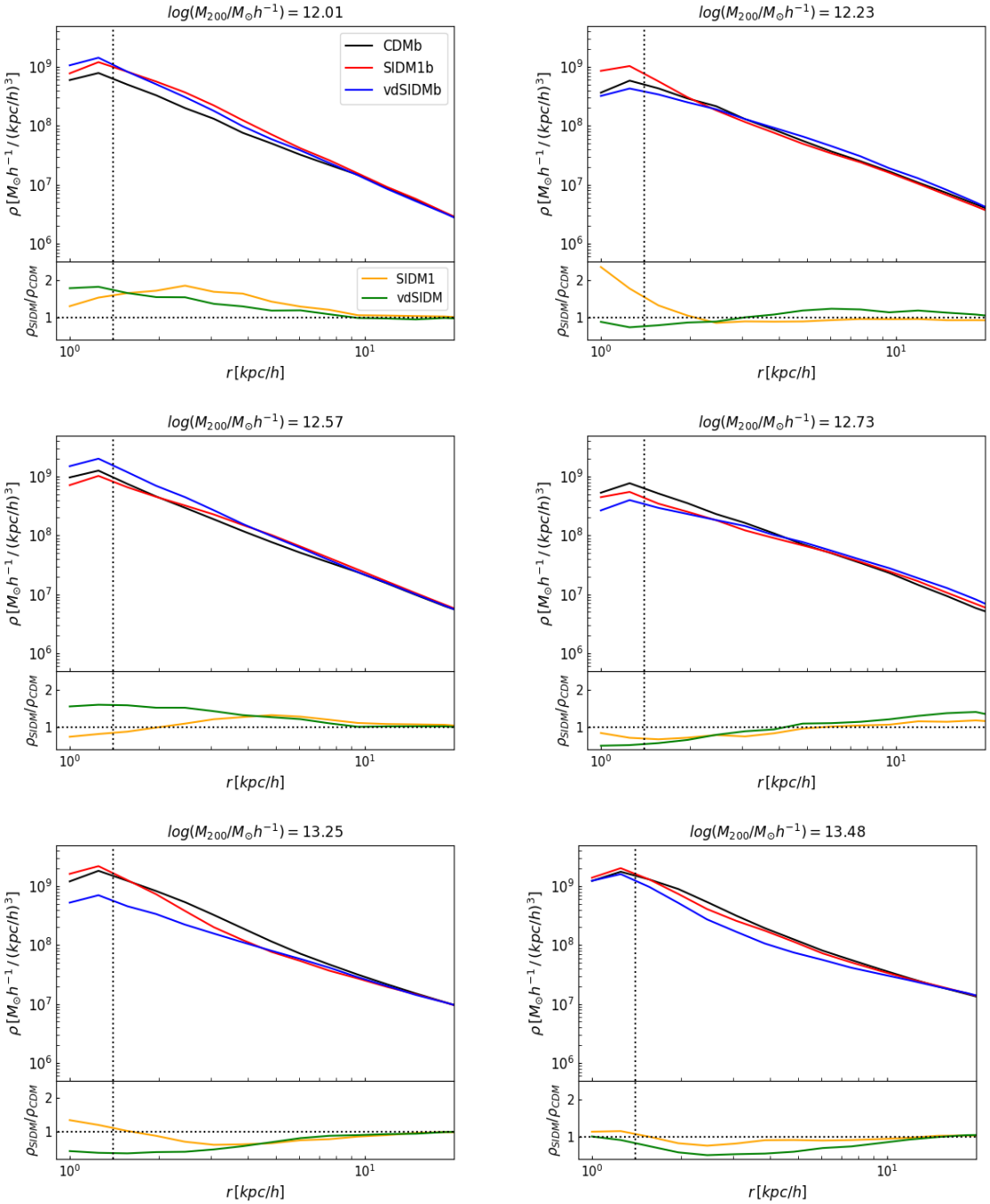

Figure 5.9: *Top: Density profiles of the central regions of single matched haloes in full-hydrodynamic simulations. The vertical line marks* $2\epsilon = 1.4kpc/h$*, within which interpretation requires care. Bottom: Density ratio between profiles in SIDM and CDM;* ρ_{SIDM1}/ρ_{CDM} *(orange);* ρ_{vdSIDM}/ρ_{CDM} *(green). The plots are ordered in increasing order of mass from the least to the most massive of available haloes.*

CORED systems, but the amplitude of the difference between SIDM and CDM does not vary continuously with the mass, but depends on the considered halo. Moreover, while in the average profiles we found no differences between the SIDM1 model and the vdSIDM model of the same mass Group, in the case of single haloes the two models differ from each other and their trend varies moving from one halo to another. These results seem to suggest that in order to obtain more solid results, it is not enough to study the averaged profiles in mass bins, but it is also necessary to analyze some single haloes or a sub-population which in some cases may behave differently, regardless of the mass. At the same time, one should be careful when extending results coming from small samples to the general halo population.

5.6 Mass-concentration relation

We now use the results from the previous sections to study the mass-concentration relation of our simulated sample.
As discussed in section 3.2.1, the equilibrium density profile of CDM haloes is now well known, and it may be well approximated by scaling a simple formula, known as NFW profile

$$\frac{\rho(r)}{\rho_c} = \frac{\delta_c}{(r/r_s)(1+r/r_s)^2}\,. \tag{5.3}$$

This profile is defined by a scale radius, r_s, and a characteristic density , δ_c, where these scaling parameters may also be defined in terms of the halo virial mass, M_{vir}, and a dimensionless concentration parameter, c which is defined as the ratio of a halo's virial and scale radius:

$$c_{vir} = \frac{r_{vir}}{r_s}\,. \tag{5.4}$$

Mass and concentration are correlated: at a given redshift, the concentration drops monotonically with increasing halo mass, implying a connection between a halo's characteristic density and its assembly time. The concentration-mass relation, $c(M)$, is attractive because over a small range of halo masses, concentrations can be well fit by simple power law in M. Because mass and concentration together fully describe the equilibrium mass profile of a halo, there has been a lot of interest in figuring out how such a connection came to be, as well as how it relates to redshift and cosmological parameters. Ludlow et al. (2014), using Millennium Simulations, worked in this direction, studying the mass – concentration – redshift relation for CDM haloes. They found that concentration is a monotonic but weak function of mass, varying by only a factor of four over the six decades in the mass range resolved by these simulations at z = 0, and that concentrations decrease systematically with increasing redshift, even though the magnitude of the decrease is mass dependent (see Fig. 5.10). The results just presented use haloes in CDM only, and the fits are made with an NFW profile. However other works have also

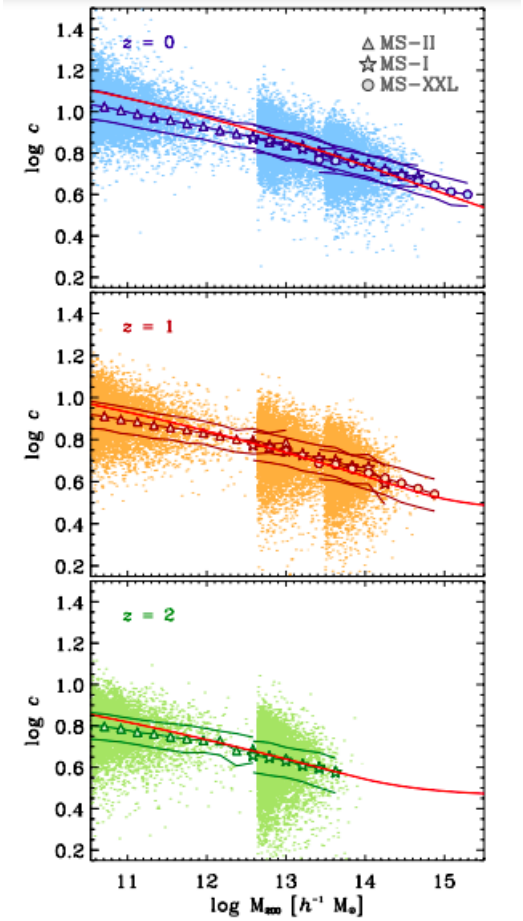

Figure 5.10: *Mass and redshift dependence of the best-fitting NFW concentrations for all relaxed CDM haloes. From top to bottom, panels correspond to haloes identified at* $z = 0, 1, 3$ *respectively. Individual haloes are shown as coloured dots; heavy filled symbols show the median trends for each simulation; 25th and 75th percentiles are shown as thin lines. The solid red line in each panel shows the mass–concentration relation obtained from fitting NFW profiles. Credits : Ludlow et al. (2014)*

calculated Einasto concentrations showing that r_{-2}, the radius at which the density's logarithmic slope is isothermal, is similar to r_s in the NFW profile: as a result, the concentration, $c_{200} = r_{200}/r_{-2}$, approaches the NFW value (eq. (5.4)). In this work we have fitted the profiles with an Einasto profile, defined by eq (5.2), thus here we use the profiles from previous section to calculate the concentration of each and we perform a linear fit to derive the mass-concentration relation for all our models:

$$\log(c_{200}) = A + B\ \log(M_{200})\,, \tag{5.5}$$

where A represents the intercept and B the slope of the relation. Tab. 5.6 shows the best-fit parameters for our models. Fig. 5.11 shows the mass-concentration relation both

	A	**B**
CDM	1.413 ± 0.234	-0.053 ± 0.019
CDMb	1.628 ± 0.447	-0.057 ± 0.036
SIDM1	1.928 ± 0.140	-0.105 ± 0.011
SIDM1b	1.889 ± 0.521	-0.079 ± 0.042
vdSIDM	1.742 ± 0.146	-0.093 ± 0.012
vdSIDMb	1.656 ± 0.492	-0.061 ± 0.040

Table 5.6: *Linear best fit parameters (eq.*(5.5)*), for the mass-concentration relation for the 6 models. The errors represent 1 standard deviation.*

in the case of DM-only simulations (left) and in the case of full-hydrodynamic simulations (right). We recover the typical trend of the relation $c_{200}(M_{200})$: the concentration is a monotonic but weak decreasing function of halo mass. For DM-only simulations, both SIDM models have a steeper slope than the CDM model with vdSIDM lower than SIDM1: over our mass range, SIDM halo concentrations span a wider range of values than CDM concentrations. The solid light blue line, in Fig. 5.11 (left panel), represents the mass-concentration relationship found by Child et al. (2018) for CDM-only haloes ranging between $10^{11}\,M_\odot$ and $10^{15}\,M_\odot$, at $z = 0$. The authors used the same linear equation ((5.5)) and found:

$$\log(c_{200}) = 2.086 + (-0.101)\ \log(M_{200})\,, \tag{5.6}$$

which is consistent within the errors with our results.
Moreover, the concentration increases in the full-hydrodynamic simulations, but this increase is greater for the SIDM models. As a result, when we consider baryon physics in the simulations, the differences between DM models are less pronounced (bottom panels).

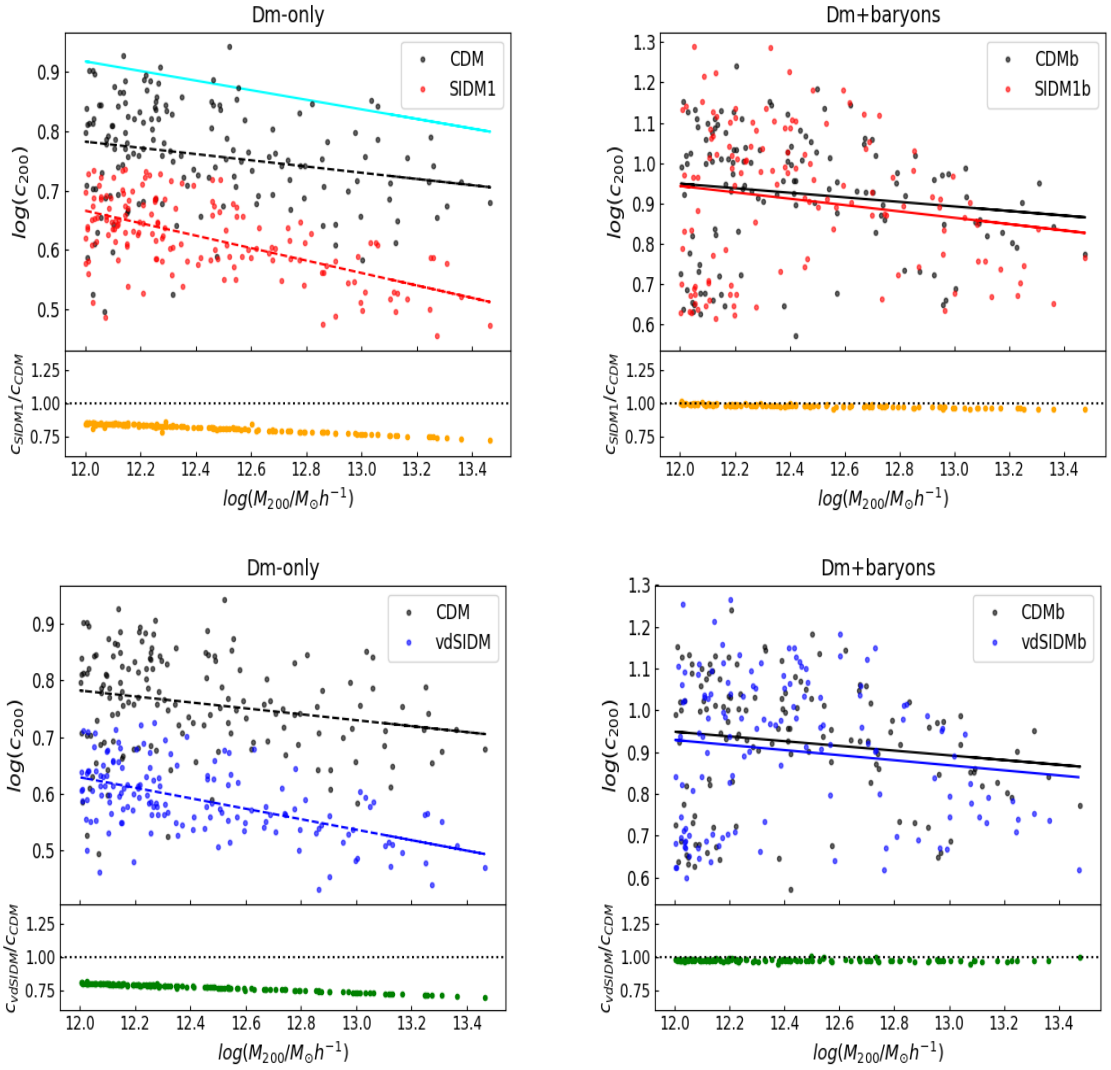

Figure 5.11: *Concentration–mass relation computed at $z = 0$ using the best-fitting parameters from Einasto profile. The best-fitting linear relation for the CDM, SIDM and vdSIDM runs is shown by the black, red and blue lines. Individual haloes are shown as coloured dots. Left: haloes in DM-only simulations. The solid light blue line represents the mass-correlation relationship found by Child et al. (2018), with 'Q Continuum' and 'Outer Rim' simulations. Right: haloes in full-hydrodynamic simulations. Bottom panels: ratio between the linear fit in SIDM models and the one in CDM.*

Chapter 6

Halo Shapes

As discussed in section 4.2, in addition to redistributing energy amongst DM particles, self-interactions modify the orientations of DM particle orbits, resulting in more isotropic velocity distributions. This modifies the DM distribution, changing the shape of the halo. While CDM haloes are usually triaxial, self-interaction can make them more spherical. In comparison to CDM haloes, the minor-to-major axis ratio c/a is expected to be closer to unity in the central regions of SIDM haloes (Spergel and Steinhardt 2000a; Peter et al. 2013). These predictions for the macroscopic effects of SIDM provide an opportunity to use halo shapes as a test of DM self-interactions (Buote et al. 2002; Miralda-Escudé 2002). However, also these results are based on SIDM DM-only simulations, while it is essential to understand if the inclusion of baryonic effects can, as in the case of density profiles, modify and / or mask these differences between DM models. Recently, it has been shown that for both CDM (Chua et al. 2021) and SIDM (Robertson et al. 2019) haloes, the presence of baryons close to the halo centres can have an impact on halo shapes: the formation of a central baryonic mass can modify the orbits of approaching dark matter particles. As a result, DM haloes from full-hydrodynamic simulations present more spherical configurations than their DM-only counterparts.
In this chapter we will analyze the shape properties of our simulated haloes at $z = 0$, comparing the predictions from DM-only simulations with those from full-hydrodynamic simulations.

6.1 Halo shape algorithm

We use the method used in Robertson et al. (2019) to calculate the shapes of the simulated haloes. For each of the 3 DM models, we separate the calculation using the mass bins (Groups) defined in section 5.2. Assuming that dark matter haloes are triaxial, their shapes are determined by the axis ratios: $s \equiv c/a$ and $q \equiv b/a$ where a, b and c are the major, intermediate and minor axes respectively (i.e. $a > b > c$). These parameters

can be found at each radius, using an iterative algorithm with the *reduced inertia tensor* defined as follows:

$$I_{ij}(R) \equiv \sum_{n:r_n<R} \frac{x_{i,n}x_{i,j}m_n}{r_n^2} \Big/ \sum_{n:r_n<R} m_n \,, \tag{6.1}$$

where $(x_{1,n}, x_{2,n}, x_{3,n})$ are the coordinates of the nth particle with mass m_n. For the shape definition we use the location of the center of mass of each halo, with the positions of particles defined with respect to this point and all spherical/ellipsoidal search volumes centred there also. At fixed R we use all particles with $r_n < R$. At the first iteration r_n is the distance of the nth particle from the centre of mass of the halo:

$$r_n = \sqrt{x_{1,n}^2 + x_{2,n}^2 + x_{3,n}^2} \,, \tag{6.2}$$

and the algorithm calculates and diagonalizes the reduced inertia tensor (Eq. (6.1)) to get the first set of eigenvalues and eigenvectors. We label the eigenvalues of $I_{ij}(r)$ as a^2, b^2 and c^2, with corresponding eigenvectors $\vec{e}_1$, $\vec{e}_2$ and $\vec{e}_3$[1]. In the subsequent iterations the algorithm uses the eigenvectors from the previous iteration as a coordinate basis, rotating the reference frame and it redefine r_n as an ellipsoidal radius:

$$r_n = \sqrt{x_{1,n}^2 + x_{2,n}^2/q^2 + x_{3,n}^2/s^2} \,, \tag{6.3}$$

where the sum in equation (6.1) is made over all particles with $r_n < (q\,s)^{-1/3}R$. This requirement corresponds to keeping the volume within which particles contribute to I_{ij} fixed. For each radius R the algorithm continues until both s and q converge; i.e. when fractional differences in successive values differ by less than 1%, meaning when:

$$\left(\frac{q_i - q_{i-1}}{q_{i-1}}\right) \leq 0.01 \qquad and \qquad \left(\frac{s_i - s_{i-1}}{s_{i-1}}\right) \leq 0.01 \tag{6.4}$$

For each halo in each Group we calculate the inertia tensor $I_{ij}(R)$ for 15 bins , with R logarithmically-spaced between $R_{min} \sim 3\,kpc$ (minimum radius to have $N_{particles} > 1000$) and $R_{max} =< r_{vir} >$ (mean virial radius for each Group). Once we have obtained the inertia tensors for each halo at different radii, we calculate the eigenvalues and eigenvectors.

6.2 Halo Shapes

In this section, we will focus on comparing the shape properties in the CDM, SIDM1 and vdSIDM models and analyzing what happens when the baryons are also considered. Fig. 6.1 shows the median minor-to-major axis ratios ($s = c/a$) as a function of radius, for each Group in CDM and SIDM1 models. Fig. 6.2 shows the same analysis in vdSIDM

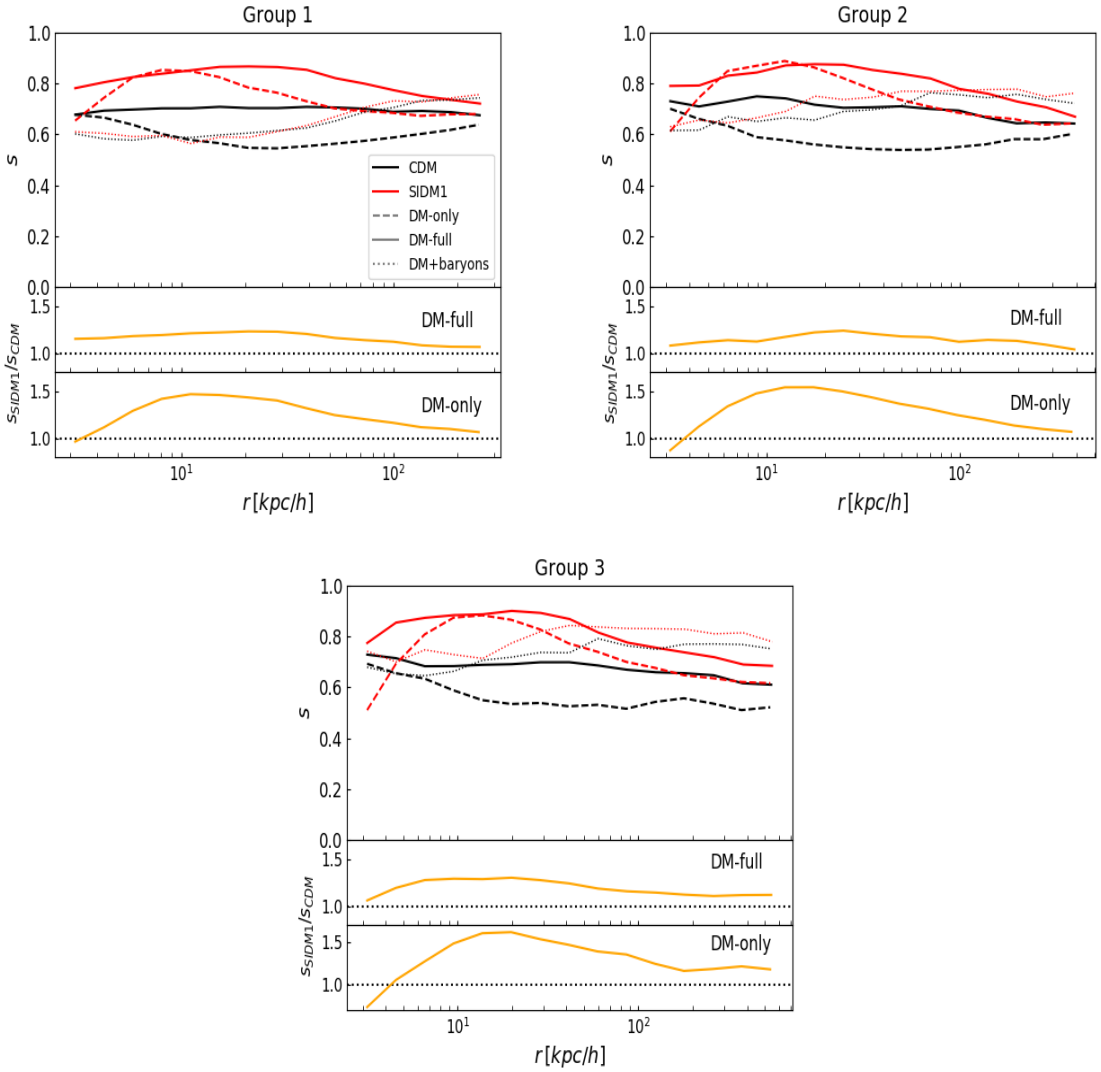

Figure 6.1: *Top: median minor-to-major axis ratios for CDM (black lines) and SIDM1 models (red lines) of haloes at $z = 0$. The solid and dashed lines represent the values for the DM haloes in full-hydrodynamic and DM-only simulations respectively. The dotted lines represent the values for DM+baryons. Bottom: ratio between DM minor-to-major axis ratio in full-hydrodynamic (DM-full) and DM-only simulations (DM-only). Group 1:* $\log(M_{200}/M_{\odot}h^{-1}) \in [12.0, 12.5]$*, Group 2:* $\log(M_{200}/M_{\odot}h^{-1}) \in [12.5, 13.0]$ *and Group 3:* $\log(M_{200}/M_{\odot}h^{-1}) \in [13.0, 13.5]$*.*

model. In agreement with previous work (Peter et al. 2013), we find that in DM-only

[1]The eigenvalues are related to the square-roots of the principal axes lengths, while the eigenvectors represents the directions of the principal axes.

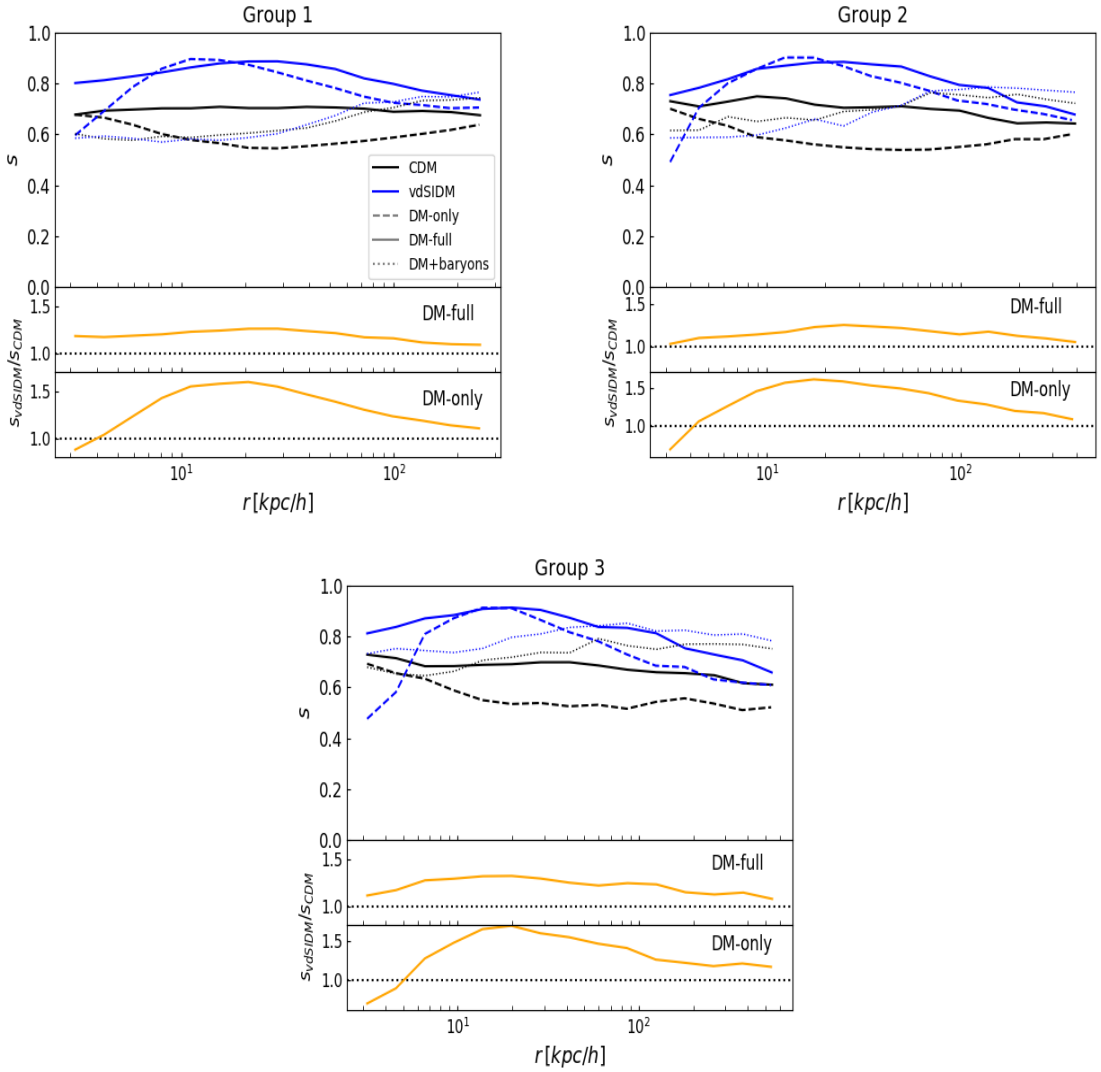

Figure 6.2: *Top: median minor-to-major axis ratios for CDM (black lines) and vdSIDM models (blue lines) of haloes at $z = 0$. The solid and dashed lines represent the values for the DM haloes in full-hydrodynamic and DM-only simulations respectively. The dotted lines rapresent the values for DM+baryons. Bottom: ratio between DM minor-to-major axis ratio in full-hydrodynamic (DM-full) and DM-only simulations(DM-only). Group 1:* $\log(M_{200}/M_{\odot}h^{-1}) \in [12.0, 12.5]$*, Group 2:* $\log(M_{200}/M_{\odot}h^{-1}) \in [12.5, 13.0]$ *and Group 3:* $\log(M_{200}/M_{\odot}h^{-1}) \in [13.0, 13.5]$*.*

simulations (dashed lines) both SIDM1 and vdSIDM models make DM haloes rounder than in CDM counterpart for each mass Group. Looking at the ratio s_{SIDM}/s_{CDM} (bottom panels), it is possible to see that this is true for all the considered radii, but

especially in the inner regions of haloes where the scattering rates are highest. In these regions we find that SIDM haloes are more spherical by more than 50% compared to CDM haloes. The trend, on the other hand, seems to be reversed approaching the minimum radius, but this is due to what Robertson et al. (2019) found on galaxy cluster scales (see Fig. 6.3): at the smallest radii the low number of particles does not allow a robust determination of the halo shape. These resolution effects are stronger for SIDM

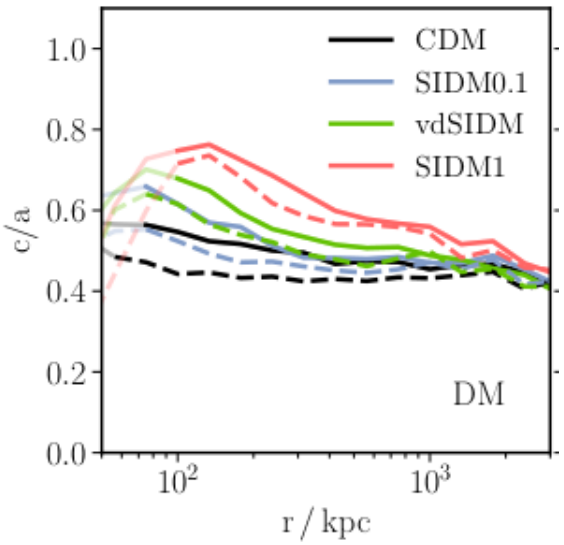

Figure 6.3: *Minor-to-major axis ratios for the DM haloes in the mass range* $10^{14.8} - 10^{15.2}\,M_\odot$ *from different simulations at* $z = 0$*, with the DM-only results represented by dashed lines. The lines become faded at radii where there are an insufficient number of particles to trust the shape measurements. Credits : Robertson et al. (2019)*

models in DM-only simulations, since as we have shown in the previous chapter, these haloes are CORED systems, thus we expect to find fewer particles at these radii than in the CDM counterpart.
In full-hydrodynamic simulations (solid lines), the CDM haloes in each Group are rounder (larger s) at all radii compared to their DM-only counterparts (the solid and dashed black lines are separated at all radii). We find that the amount of "sphericalization" (increase of s) in CDM model depends on the distance to the halo centre: the effect of baryons is the largest near the halo centre but reduces towards the virial radius. These results are in agreement with previous work on the impact of the baryonic feedback on the CDM haloes shape (Bryan et al. 2013; Chua et al. 2021) and they make sense given that the contribution of baryons to the total density decreases with radius.
In the case of the SIDM models this effect is less intense, we find that at the maxima of sphericity, the values of s for SIDM haloes in full-hydrodynamic simulations and in

DM-only simulations are similar (the solid and dashed red/blue lines are overlapped). As shown for the density profiles, this behavior may be due to the fact that SIDM haloes are more strongly affected by the presence of baryons in the inner regions, where the scattering rate is highest and baryons are the dominant component (see Fig. 5.5). In agreement with these results, Sameie et al. (2018a) showed that SIDM haloes shape are more responsive to the presence of the baryonic disk and are more aligned with the disk potential than their CDM counterpart. For this reason we expect that this trend is also true at smallest radii, where it is not possible to trust the measurements of the DM-only SIDM halo shapes due to the resolution effects discussed above. For larger radii, where the scatter rate is lower and and the baryons are no longer dominant, we find the same trend of CDM haloes: SIDM haloes are more spherical in full-hydrodynamic simulations than in their DM-only counterpart and the difference decreases towards the virial radius. Therefore, in full-hydrodynamic simulations we have two different baryonic effects on the DM haloes shape, which depend on the DM model:

- Due to baryon feedback, CDM haloes are rounder at all radii compared to their DM-only counterparts and the difference decreases towards the virial radius.
- The distribution of SIDM particles is strongly affected by the baryon potential. For this reason, in the central parts where the baryons dominate ($r < 30 - 40\,kpc/h$) the SIDM haloes have similar sphericity as their DM-only counterpart. In the outer regions SIDM haloes are more spherical in full-hydrodynamic simulations than in their DM-only counterpart and the difference decreases with the radius.

The two effects described above make the differences between DM models less pronounced in the case of full-hydrodynamic simulation, compared to DM-only simulations. While from DM-only simulations we find that in the central areas the differences in the shapes of the haloes between CDM and SIDM models is about 50% (bottom panels), in the case of full-hydrodynamic simulations these differences drop to 20-25% (middle panels). However, even if the differences are smaller than in DM-only counterparts, in full-hydrodynamic simulations the SIDM haloes are still more spherical than the CDM haloes.
As a final comparison, Fig. 6.4 shows all median minor-to-major axis ratios as a functions of the radius for all 6 runs. The three plots on the left show the ratio in DM-only simulations, while those on the right show the average profiles in full-hydrodynamic simulations for each mass bin. From this figure it is easier to compare the two SIDM models used. We find that even in the case of the haloes shape, the small differences between the two models in DM-only simulations (see Group 1) are canceled in the case of full-hydrodynamic simulations. However, both for DM-only and full-hydrodynamic simulations, the median minor-to-major axis ratios is higher for SIDM haloes than in CDM counterparts.

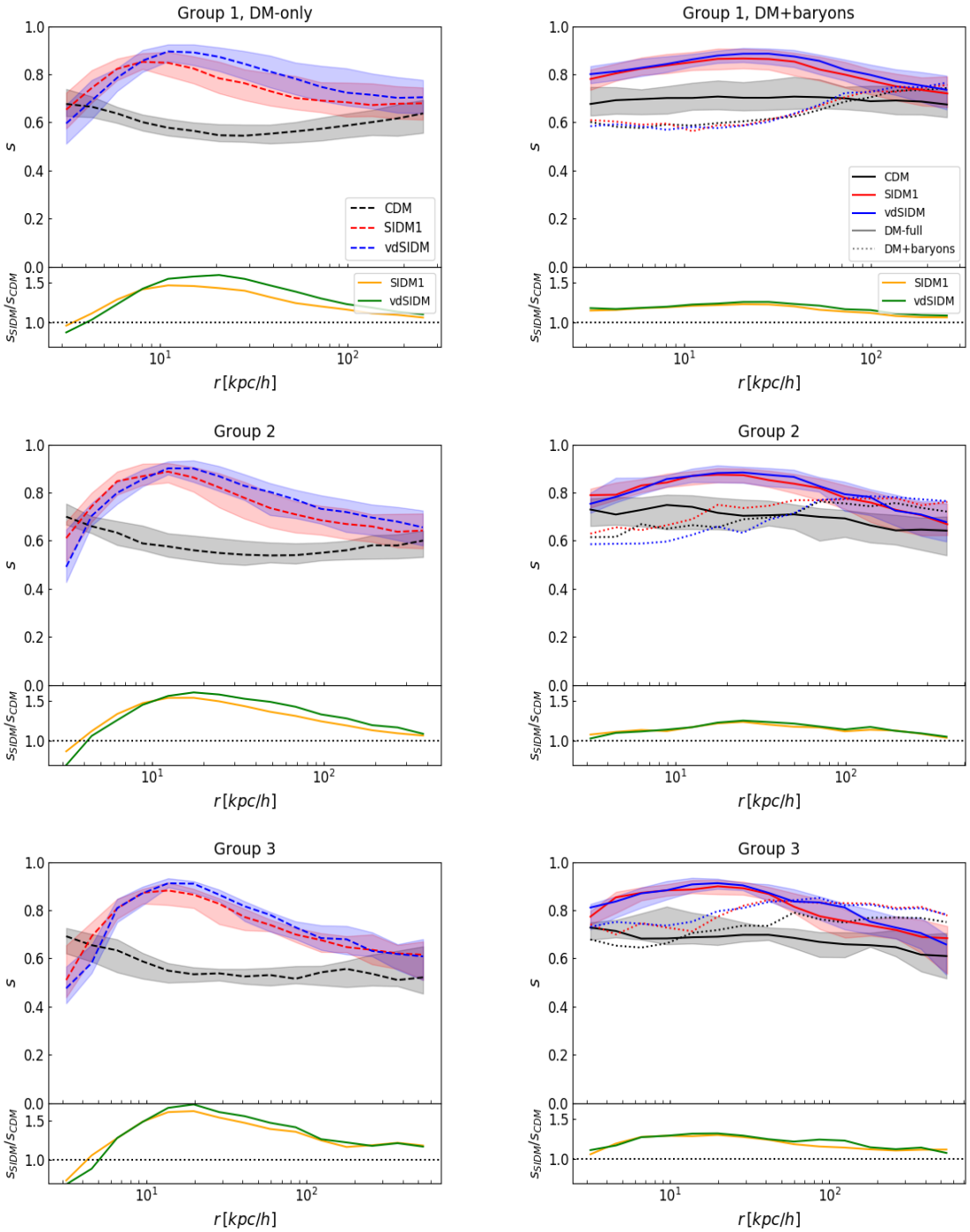

Figure 6.4: *Top: Median minor-to-major axis ratios for the models used in each 3 mass Groups at $z = 0$. Left: profiles in the DM-only simulations. Right: profiles in the full-hydrodynamic simulations for the corresponding Groups. Halo-to-halo variations are represented by shaded regions which enclose the 25th-75th percentiles. Bottom: ratio between profiles in SIDM and CDM.*

6.3 Matched Haloes

In this section, using the matched systems described in section 5.5, we analyze the shape properties for some individual haloes. In Fig. 6.5 we plot the minor-to-major axis ratios for the same individual haloes selected in Fig. 5.9, for our three DM models. Despite the general average behavior, individual haloes can behave differently. For example, we find that in the haloes with $log(M_{200}/M_{\odot}h^{-1}) = 12.01$ and $log(M_{200}/M_{\odot}h^{-1}) = 13.25$, the differences between the models become negligible. This may depend on the evolutionary history of the single halo: AGN feedback, Supernovae feedback, star formation, stellar winds, but also the presence of a more or less compact baryonic disk can alter the distribution of DM, consequently modifying the halo shapes (Sameie et al. 2018a; Chua et al. 2021).
In Fig. 6.6 we plot the minor-to-major axis ratios for all matched haloes as a function of their virial mass, for three different radii. For $r = 14\,kpc/h$, almost all haloes in SIDM models are more spherical than their counterparts in CDM (bottom panels): as shown in Fig 6.5 it is possible that some individual haloes may behave differently due to different evolution histories. This also holds true for $r = 60\,kpc/h$. For the largest considered radius ($r = 260\,kpc/h$), even if the differences between the two models are less pronounced, it is still possible to note that most haloes in SIDM remain more spherical than in the CDM case.
These results suggest that halo shapes are affected by SIDM on larger scales than density profiles where as shown in Fig. 5.3 and Fig. 5.6 the differences between the DM models become visible on small radii ($r < 10\,kpc/h$). Moreover, at each radius, the differences in the halo shapes between DM models are more pronounced than those in the density profiles and this could make halo shapes an excellent test of DM self-interactions. In fact, since the interstellar X-ray emitting gas of elliptical galaxies fills the gravitational potential, it acts as a tracer of the underlying gravitational potential. Therefore, by observing the X-ray shapes of relaxed (i.e. thermal equilibrium) elliptical galaxies, it is possible to infer the DM halo shapes and then compare them with the predictions of CDM and SIDM halo shapes from simulations (McDaniel et al. 2021).

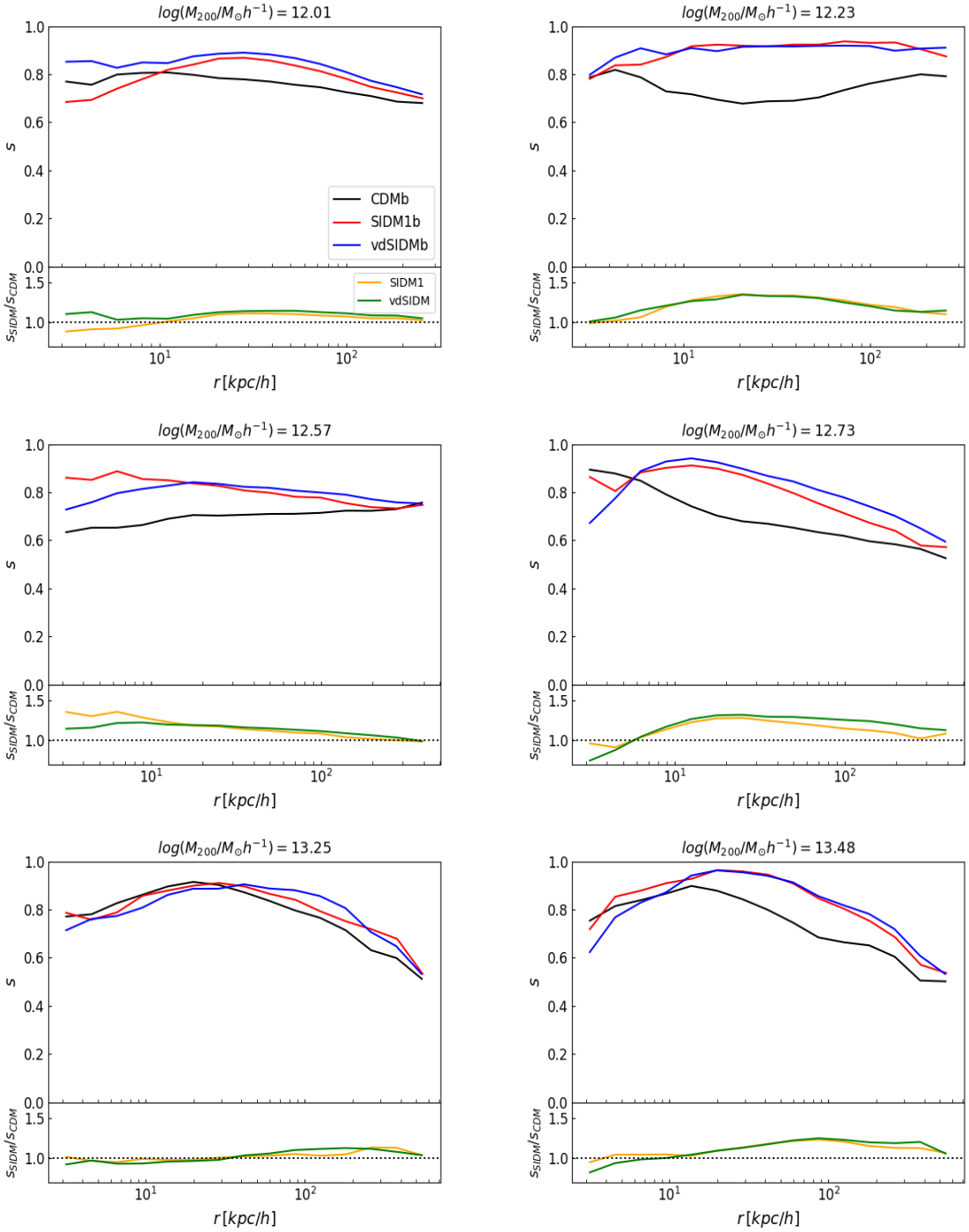

Figure 6.5: *Top: Minor-to-major axis ratios of single matched haloes in full-hydrodynamic simulations at $z = 0$. Bottom: ratio between profiles in SIDM and CDM; s_{SIDM1}/s_{CDM} (orange); s_{vdSIDM}/s_{CDM} (green). The plots are ordered in increasing order of mass from the least to the most massive of available haloes.*

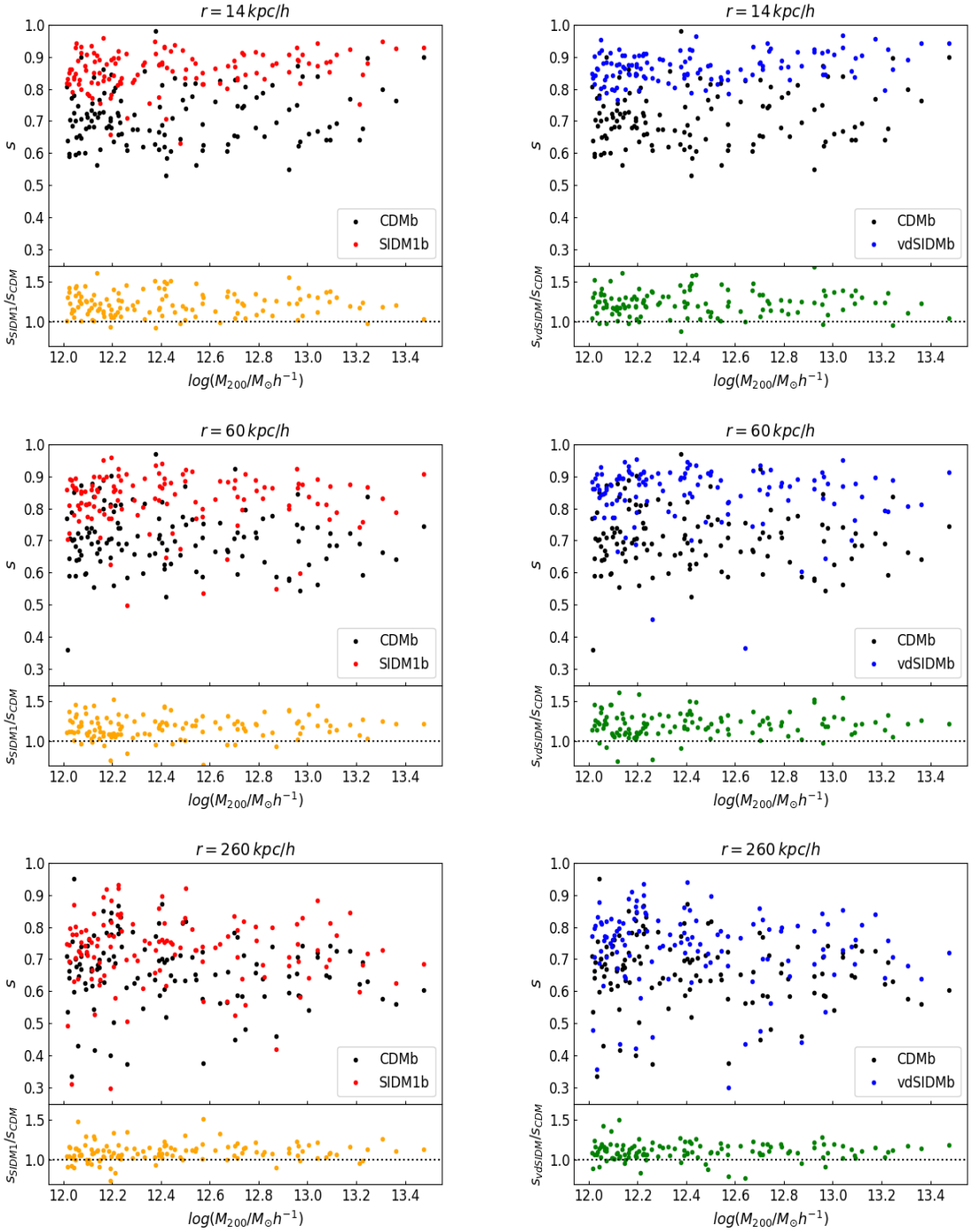

Figure 6.6: *Top: Minor-to-major axis ratios of all matched haloes in full-hydrodynamic simulations at $z = 0$, for three different radii. Bottom: ratio between profiles in SIDM and CDM; s_{SIDM1}/s_{CDM} (orange); s_{vdSIDM}/s_{CDM} (green).*

Chapter 7

Conclusions

SIDM has become an attractive alternative to CDM, due to its ability to produce a wider range of configurations that could solve the small-scale CDM problems, leaving the properties on large scale unchanged. The main signatures of SIDM models are the reduction of the central densities of DM haloes and more spherical halo shapes than the CDM counterparts. However, these predictions have so far been based on DM-only simulations, while it is essential to understand how the interplay between self-interaction and baryonic effects can urther modify the properties of haloes. For this purpose, we use EAGLE cosmological simulations, that simulate the same volume of 50 Mpc^3 , in CDM and the two SIDM models: one with constant cross section ($\sigma/m = 1\,cm^2/g$) and one with a velocity-dependent cross section. For each models a DM-only and a full-hydrodynamic version is available, allowing us to study the effect of baryons and alternative dark matter models at the same time.
We select haloes with masses M_{200} in the range between $10^{12}\,M_{\odot}h^{-1}$ and $10^{14}\,M_{\odot}h^{-1}$, at $z = 0$, for all 6 models available. However, given the volume of the boxes, we do not find haloes with mass $M_{200} > 10^{13.5}\,M_{\odot}h^{-1}$. The mass range is chosen to test and extend the results obtained by Sameie et al. (2018a) and Despali et al. (2019), not in an isolated or zoom-in simulations of individual galaxies, but using a full cosmological box. Moreover, disk and elliptical galaxies are baryon-dominated systems in the central areas. This makes these objects excellent systems for studying the interplay between baryon physics and DM properties. We split our sample into mass bins in order to compare and average the features of haloes of comparable mass. To have a sufficient number of haloes for each bin, we divide our sample into 3 groups: $12.0 < \log(M_{200}/M_{\odot}h^{-1}) < 12.5$ (Group 1), $12.5 < \log(M_{200}/M_{\odot}h^{-1}) < 13.0$ (Group 2) and $13.0 < \log(M_{200}/M_{\odot}h^{-1}) < 13.5$ (Group 3). Tab. 5.3 shows the relative number of haloes for each bin and for each model.
We calculate the average profile in every mass Groups and we use the Einasto profile to fit the mean radial density distribution. In DM-only simulations we find that SIDM haloes are systematically less dense in the central regions ($r < 10\,kpc/h$) than their CDM counterparts. For each Group the density in these regions can be lower by more

than 50% in SIDM compared to the CDM profiles. However, when we calculate the average density profiles in full-hydrodynamic simulations we find the final properties of the central regions depend on the considered mass bin:

- **Group 1**: SIDM has a higher density than that in CMB;
- **Group 2**: there are no differences in the density profile between the models:
- **Group 3**: SIDM has a lower density than that in CMB.

Moreover, we find that also in full-hydrodynamic simulations the differences between the DM models are visible only at small radii ($r < 10\,kpc/h$), but they drop from $\sim 50-60\%$ in DM-only simulations to $\sim\ 15-20\%$ with the addition of baryonic physics (see Fig. 5.3 and Fig. 5.6). In agreement with Despali et al. (2019) we show that the interplay between DM self-interaction and baryons can induce a complex evolution of the halo properties, which depends on the halo mass and morphological type. However, we show that the baryonic effects can in part mask the differences in the density profiles between the DM models, making them less pronounced than in the DM-only case. The results presented above hold true for both SIDM models. In the considered mass range, we find that, on average, there are no differences between the SIDM model with constant cross section and the SIDM model with velocity dependent cross section (see Fig. 5.7).
In Chapter 6 we employ the method used in Robertson et al. (2019) to calculate the shapes of the simulated haloes. This method is described in section 5.2. We use the minor-to-major axis ratios ($s = c/a$) as a proxy of the halo shapes. In agreement with previous work (Peter et al. 2013), we find that in DM-only simulations both SIDM models make DM haloes rounder than their CDM counterpart for each mass Group and we show that this is true for all the considered radii, but especially in the inner regions where the scattering rates are highest. In these regions we find that SIDM haloes are more spherical by more than 50% compared to CDM haloes. The trend, on the other hand, seems to be reversed approaching the minimum radius, but this is due to resolution effects of our method: at these radii there are an insufficient number of particles to trust the shape measurement.
In agreement with Bryan et al. (2013) and Chua et al. (2021) we find that in full-hydrodynamic simulations the CDM haloes are rounder at all radii compared to their DM-only counterparts, but this effect is larger near the halo centre and decreases towards the virial radius. This holds true for SIDM models, but only in the outer parts of the haloes ($r > 30 - 40\,kpc/h$), while at smaller radii the values of s for SIDM haloes in full-hydrodynamic simulations and in DM-only simulations are similar (see Fig. 6.1 and Fig. 6.2). This behavior may be due to the fact that SIDM haloes shape are more responsive to the presence of the baryonic disk potential in the inner part than their CDM counterpart (Sameie et al. 2018a).
These effects described above make the differences between DM models less pronounced

in full-hydrodynamic simulation, compared to DM-only simulations. Also for the halo shapes we find that these differences drop from $\sim 50-60\%$ in DM-only simulations to $\sim\ 25-20\%$ with the addition of baryonic physics. However, we show that also with the inclusion of the baryonic effects the haloes in the SIDM models are more spherical than in the CDM counterpart and that this is true not only at small radii, but even in more external regions ($r \sim 60-100\,kpc/h$). Such results suggest that the comparison between the predictions on the DM halo shapes from simulations and the ones inferred from observations can offer us a way to discriminate between DM models.
Finally, we match systems between the different runs using the minimum distance between the haloes centers of mass in the different simulations (see 5.8). Despite the general average behavior on the properties of the density profiles and on the shapes, we show that individual haloes can behave differently (see 5.9 and 6.6). This may depend on the evolutionary history of the single halo: systems with comparable mass can belong to distinct categories, and their behavior can be explained in terms of different accretion history (Sameie et al. 2018a; Despali et al. 2019). For these reason, we aim to analyze the mass accretion history of these systems from higher z up to $z = 0$ in order to understand how the haloes final properties found in this work, can be linked to different evolutionary histories.
As we have seen in sections 3.4.1 and 4.2.2 strong gravitational lensing allows us to measure the total projected mass distribution of the lens directly. Thus, different halo properties between DM models may have direct consequences on the distribution of the main lensing observables. Therefore, a step forward for this work will be to generate realistic mock lensed images to calculate the strong lensing properties of our simulated systems, such as the Einstein radii and convergence maps. In this way, it will be possible to test the differences (if any) in the lensing signal between our DM models. The comparison between these predictions and observational data could offer us a way, independent from X-ray observations, to discriminate between DM models.

Appendix A

Meszaros effect and Free-streaming

The dark matter component inside the horizon grows as in equation (3.2). From this equation it is possible to calculate how much the DM density contrast has increased, from when the perturbations enter the horizon until the time of equivalence, i.e. we calculate the ratio

$$\frac{\delta_{k,DM}(t_{eq})}{\delta_{k,DM}(t_{or})} = \frac{1+\frac{3}{2}\frac{a_{eq}}{a_{eq}}}{1+\frac{3}{2}\frac{a_{or}}{a_{eq}}} = \frac{\frac{5}{2}}{1+\frac{3}{2}\frac{a_{or}}{a_{eq}}}\,, \tag{A.1}$$

so if the perturbation enters the horizon immediately after the Big-bang, $a_{or} = 0$:

$$\left(\frac{\delta_{eq}}{\delta_{or}}\right)_{max} = \frac{5}{2}\,, \tag{A.2}$$

while if the perturbation enters the horizon at $t = t_{eq}$:

$$\left(\frac{\delta_{eq}}{\delta_{or}}\right)_{min} = 1\,, \tag{A.3}$$

i.e. the perturbation does not have sufficient time to grow inside the horizon. The first case is the extreme case, that is, where we would have greater growth, this means that the perturbations of DM before the equivalence can grow inside the horizon at least than a factor of 5/2 which is absolutely negligible. This effect is called stagnation or Meszaros effect and essentially tells us that if a perturbation enters the horizon before the equivalence it will stop growing. Therefore, perturbations started with the same amplitude will end up having different amplitudes (those outside the horizon will continue to grow). Once the equivalence has been overcome, all the perturbations will start growing again in the same way.
Another fundamental characteristics of DM must be that it interacts weakly with the baryonic matter, therefore it does not emit radiation and that it must decouple from the radiation much earlier than the baryons $a_{dec,DM} < a_{eq}$, to allow the so-called baryon

catch up. But given these fundamental characteristics, several models of DM can be built. To carry out a first classification, we introduce the time scale of non-relativization $a_{NR,DM}$, that is, the time scale at which the DM particles stop being relativistic, which is essentially the same as knowing the mass of the particles because this happens when:

$$kT < m_{DM}c^2\,, \tag{A.4}$$

therefore the most massive particles are those that stop being relativistic first, since T is a function that decreases over time. Having defined this time scale, we can classify the particles as:

- **Hot Dark Matter**(HDM) if they are still relativistic at the moment of decoupling: $a_{NR,DM} > a_{dec,DM}$.
- **Cold Dark Matter**(CDM) if they stop being relativistic before the moment of decoupling: $a_{NR,DM} < a_{dec,DM}$.
- **Warm Dark Matter**(WDM) it is an intermediate case between HDM and CDM.

This classification results in a difference in the masses of the particles, and from equation (A.4) we derive that CDM and WDM candidates will be heavier than HDM ones. To study the effects due to free-streaming, it is useful to introduce the Jeans mass for the DM pertrurbations. The typical trend for the Jeans scale is

$$\lambda_J \propto v\ \rho_{dom}^{-1/2}\,, \tag{A.5}$$

where ρ_{dom} represents the density of the dominant component. Or similarly we can define the Jeans Mass:

$$M_J \propto \lambda_J^3 < \rho_M >\,, \tag{A.6}$$

where $< \rho_M > \propto a^{-3}$ represents the average density of matter. This scale varies during the cosmic epochs, depending on the trends of v and ρ_{dom}:

1. $a < a_{NR,DM}$

   Radiative era $\rho_{dom} = \rho_R \propto a^{-4}$, and the particles are still relativistic $v \sim c = const$:

   $$\lambda_J \propto cost\ \rho_R^{-1/2} \propto a^2 \longrightarrow M_J \propto a^3\,. \tag{A.7}$$

2. $a_{NR,DM} < a < a_{dec,DM}$

   Radiative era, then the velocity of the particles will also be affected by being coupled to the radiation: $v^2 \propto T_R \propto a^{-1}$, so $v \propto a^{-1/2}$:

   $$\lambda_J \propto a^{3/2} \longrightarrow M_J \propto a^{3/2}\,. \tag{A.8}$$

3. $a_{dec,DM} < a < a_{eq}$

   After decoupling, the particles will begin to propagate freely following the expansion of the Universe $v \propto a^{-1}$:

$$\lambda_J \propto a \longrightarrow M_J = const\,. \tag{A.9}$$

4. $a > a_{eq}$

   Matter era $\rho_{dom} = \rho_M \propto a^{-3}$ and the speed always remains of free motion, so

$$\lambda_J \propto a^{-1/2} \longrightarrow M_J \propto a^{-3/2}\,. \tag{A.10}$$

In general we will have that a perturbation with a mass greater than the mass of Jeans will be able to grow, while if its mass is smaller than the Jeans mass, we must consider the phenomena of cancellation due to free streaming. Looking at the trends of the mass of Jeans in the various eras, we notice that after a_{dec} this scale stops growing and remains constant up to a_{eq} and then starts to decrease. We conclude that any scale that has a mass $M > M_J(a_{dec}) = M_J(a_{eq})$ will always be able to grow and will not undergo any phenomenon of free streaming. Using the dispersion equation, the functional trend of the Jeans mass can be found more accurately and therefore this maximum value can be calculated, which in the case of CDM is typically:

$$M_{J,CDM}(a_{eq}) = 10^5 - 10^6 M_\odot\,, \tag{A.11}$$

but the exact value depends on the mass of the specific candidate. Fig. A.1 shows schematically the trends of the Jeans Mass. For comparison, both CDM and HDM trends are shown. As we have defined the Jeans scale, it is also possible to define a free streaming scale under which free-streaming acts, canceling the perturbation: the particles respond to the average potential of the Universe, which tends to level the density contrasts.

$$\lambda_{FS} = a(t)\int_0^t \frac{v_{DM}dt'}{a(t')} \rightarrow M_{FS} = \frac{4}{3}\pi\lambda_{FS}^3 < \rho_M > \ . \tag{A.12}$$

In this case, we know that $a(t)$ changes at $z = z_{eq}$:

$$\begin{cases} a \propto t^{1/2} \rightarrow dt \propto a\,da & if\ a < a_{eq} \\ a \propto t^{2/3} \rightarrow dt \propto a^{1/2}da & if\, a > a_{eq} \end{cases} \tag{A.13}$$

Rewriting the free-streaming scale in a more useful way:

$$\lambda_{FS}(t) = a(t)\int_0^{a(t)} \frac{v_{DM}}{a}\frac{dt}{da}da\,, \tag{A.14}$$

it is possible to calculate its trend in the different cosmic eras:

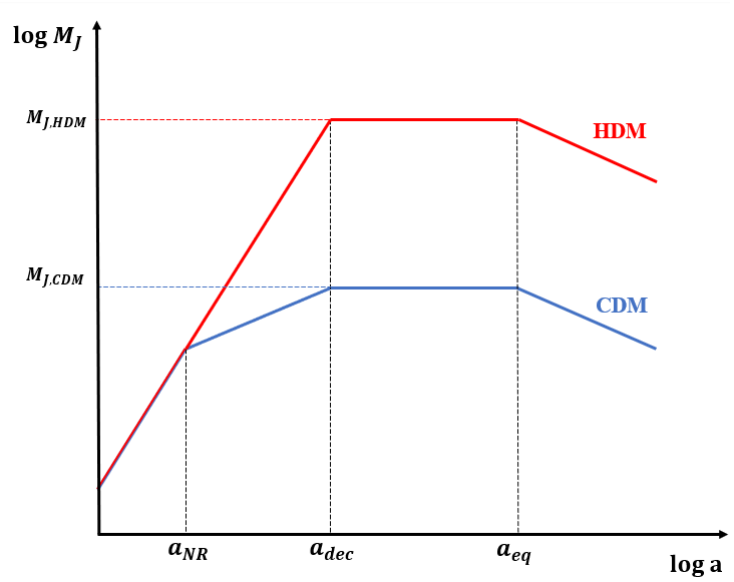

Figure A.1: *Trends in the Jeans mass during the various cosmic eras for CDM (blue) and HDM (red). The dotted horizontal lines represent the scale above which the collapse occurs without experiencing the free streaming, for the two models.*

- $a < a_{NR} \longrightarrow M_{FS} \propto a^3$;
- $a_{NR} < a < a_{dec,DM} \longrightarrow M_{FS} \propto a^{3/2}$;
- $a_{dec,DM} < a < a_{eq} \longrightarrow M_{FS} \propto (ln\, a)^3$;
- $a > a_{eq} \longrightarrow M_{FS} = const$.

By substituting the exact values, it can be shown that the free-streaming mass scale follows similar trends to those of the Jeans mass scale, meaning that all perturbations with mass $M < M_{FS} \sim M_J$ will be canceled from free-streaming. Then, the only perturbations that can grow (i.e. they will never be under M_{FS}) are those with $M > M_J(a_{eq})$.

Appendix B

Spherical collapse model

Linear perturbation theory has a limited range of applicability $\delta \ll 1$; in particular, the evolution of structures like clusters of galaxies cannot be treated within the framework of linear perturbation theory, since we know that for these structures $\delta \sim 10^{2-3}$. In general, numerical approaches are required to analyze the development of non-linear structures. However, analytical descriptions exist for certain relevant limiting situations that can reflect the non-linear development of the mass distribution in the Universe. The spherical collapse model follows the simplest approach to non-linear development, which is to examine fluctuations with a basic geometric symmetry. The idea is to consider the perturbations as perfectly spherical closed Universes ($\Omega_P > 1$), immersed in a background Universe, which for simplicity we consider EdS ($\Omega_U = 1$). Moreover, we consider that these perturbations are stationary with respect to the Hubble flux, that is, that they have zero peculiar velocity. Equation (1.46) for the perturbation ($W = 0$), seen as a closed Universe is

$$\left(\frac{\dot{a}}{a_i}\right)^2 = H_i^2 \left[1 - \Omega_P + \Omega_P \left(\frac{a_i}{a}\right)\right] . \tag{B.1}$$

In this model, there is a t_{max} whereby the Universe stops expanding and starts collapsing. The density perturbation at this time will be:

$$\rho_P(t_{max}) = \rho_P(t_i) \left(\frac{a_i}{a_{max}}\right)^3 , \tag{B.2}$$

where $a_{max} = a(t_{max})$ as we have said, it is the point where the perturbation stops expanding, i.e. $\dot{a}_{max} = 0$. From this moment on, the self-gravity will be such that it starts the collapse. Then we take the equation (B.1) for $t = t_{max}$:

$$0 = \Omega_P \left(\frac{a_i}{a_{max}}\right) + (1 - \Omega_P) \qquad \longrightarrow \qquad \frac{a_{max}}{a_i} = \frac{\Omega_P}{\Omega_P - 1} \tag{B.3}$$

and replacing this last relation in the equation (B.2)

$$\rho_P(t_{max}) = \rho_c(t_i)\, \Omega_P \left(\frac{\Omega_P - 1}{\Omega_P}\right)^3 . \tag{B.4}$$

Now to derive $\rho_P(t_{max})$, we need to use parametric solutions obtained for curved Universes:

$$\begin{cases} a(\theta) = a_0 \frac{\Omega_0}{2(\Omega_0-1)}(1-\cos\theta) \\ \\ t(\theta) = \frac{1}{2H_0}\frac{\Omega_0}{(\Omega_0-1)^{2/3}}(\theta-\sin\theta) \end{cases} \tag{B.5}$$

and for $\theta_{max} = \pi$ we obtain

$$\begin{cases} a(\pi) = a_{max} = a_0 \frac{\Omega_0}{\Omega_0-1} \\ \\ t(\pi) = t_{max} = \frac{\pi}{2H_0}\frac{\Omega_0}{(\Omega_0-1)^{2/3}} \end{cases} \tag{B.6}$$

We can rewrite the equation for t also at time t_i

$$t_{max} = \frac{\pi}{2H_i}\frac{\Omega_P}{(\Omega_P-1)^{2/3}}\,. \tag{B.7}$$

Now we can get $(\Omega_P - 1)$ from equation (B.4)

$$\Omega_P(t_i) - 1 = \Omega_P(t_i)\left[\frac{\rho_P(t_{max})}{\rho_c(t_i)\Omega_P}\right]^{1/3}\,, \tag{B.8}$$

then

$$t_{max} = \frac{\pi}{2H_i}\left(\frac{\rho_c(t_i)}{\rho_P(t_{max})}\right)^{1/2}\,, \tag{B.9}$$

but $\rho_c(t_i) = 3H_i^2/8\pi G$, so

$$\rho_P(t_{max}) = \frac{3\pi}{32\,G\,t_{max}^2}\,. \tag{B.10}$$

For an EdS background Universe, the density trend is $t = t_{max}$ is

$$< \rho > (t_{max}) = \frac{1}{6\pi G}\frac{1}{t_{max}^2}\,. \tag{B.11}$$

Then we can define the excess density of the perturbation with respect to the background:

$$\chi(t_{max}) = \frac{\rho_P(t_{max})}{< \rho > (t_{max})} = \left(\frac{3\pi}{4}\right)^2 \sim 5.6\,, \tag{B.12}$$

then

$$\delta(t_{max}) = \frac{\rho_P(t_{max}) - < \rho > (t_{max})}{< \rho > (t_{max})} \sim 4.6\,. \tag{B.13}$$

We notice that already at the moment of maximum expansion we are no longer linear theory $\delta > 1$.

After t_{max}, the pertrubation, assumed as a closed Universe, is expected to collapse on itself in a time $t_{coll} = 2t_{max}$, however the perturbations of matter cannot collapse in one point, then it is necessary to find a radius at which the perturbation stabilizes and subsequently virializes; therefore we use the virial theorem

$$K = -\frac{U}{2}\,, \tag{B.14}$$

while the total energy $E_{tot} = K + U$, so $E_{tot} = -V/2 + V = V/2$ and we calculate it at t_{vir} and at t_{max}

$$E_{tot}(t_{vir}) = -\frac{1}{2}\frac{3}{5}\frac{GM^2}{R_{vir}}\,, \qquad\qquad E_{tot}(t_{max}) = -\frac{3}{5}\frac{GM^2}{R_{max}}\,, \tag{B.15}$$

where at $t = t_{max}$, we have zero expansion speed, so energy is all potential energy. For the conservation of energy $E_{tot}(t_{vir}) = E_{tot}(t_{max}) \rightarrow R_{vir} = R_{max}/2$ and assuming that the mass is conserved during collapse, we can calculate the density contrast at $t = t_{coll}$

$$\chi(t_{coll}) = \frac{\rho_P(t_{coll})}{<\rho>(t_{coll})} = 8\frac{\rho_P(t_{max})}{<\rho>(t_{max})}\left(\frac{t_{coll}}{t_{max}}\right)^2\,, \tag{B.16}$$

but $t_{coll} = 2t_{max}$ so

$$\chi(t_{coll}) = 32\,\chi(t_{max}) \sim 180\,. \tag{B.17}$$

Also the simulations show that the perturbation ceases to collapse, reaching a physical dimension of equilibrium R_{vir} , at the time $t = 2t_{max}$. After this moment, the overdensity begins to stabilize, until it is virialized to $t_{vir} = 3t_{max}$ and at this time $\chi(t_{vir}) \sim 400$. This approach to the non-linear theory rightly predicts high values for the density of the perturbations, closer to those observed in the formed structures (if we had used linear theories we would have been wrong by more than two orders of magnitude), but this theory, despite being simple, has two fundamental problems: it assumes perfectly spherical perturbations (the probability of having perfectly spherical perturbations is very low) and furthermore this theory strongly depends on cosmology, in fact to derive the density contrast we have assumed an Eds background. In any case, this theory predicts that the perturbation first proceeds following the Hubble expansion, then begins to slow down until it stops at t_{max}, after which it begins to collapse until $R_{vir} = R_{max}/2$, with $\chi(t_{coll}) \sim 180$ and $\chi(t_{vir}) \sim 400$.

Acknowledgements

We thank Andrew Robertson (Durham University) for sharing and providing access to the simulations and the halo catalogues used in thesis and the DiRAC Data Centric system at Durham university, operated by the Institute for computational Cosmology, where the data are stored.

Bibliography

Aghanim et al. (2020). "Planck 2018 results-VI. Cosmological parameters". In: *Astronomy & Astrophysics* 641, A6. URL: https://doi.org/10.1051/0004-6361/201833910.

Arcadi et al. (2018). "The waning of the WIMP? A review of models, searches, and constraints". In: *The European Physical Journal C* 78.3, pp. 1–57. URL: https://doi.org/10.1140/epjc/s10052-018-5662-y.

Babcock, Horace W (1939). "The rotation of the Andromeda Nebula". In: *Lick Observatory Bulletin* 19, pp. 41–51.

Balberg et al. (2002). "Self-interacting dark matter halos and the gravothermal catastrophe". In: *The Astrophysical Journal* 568.2, p. 475.

Bondarenko, Kyrylo et al. (2021). "From dwarf galaxies to galaxy clusters: Self-Interacting Dark Matter over 7 orders of magnitude in halo mass". In: *Journal of Cosmology and Astroparticle Physics* 2021.01, p. 043. URL: https://doi.org/10.1088/1475-7516/2021/01/043.

Boylan-Kolchin, Michael et al. (2009). "Resolving cosmic structure formation with the Millennium-II Simulation". In: *Monthly Notices of the Royal Astronomical Society* 398.3, pp. 1150–1164. URL: https://doi.org/10.1111/j.1365-2966.2009.15191.x.

Boylan-Kolchin et al. (2011). "Too big to fail? The puzzling darkness of massive Milky Way subhaloes". In: *Monthly Notices of the Royal Astronomical Society: Letters* 415.1, pp. L40–L44. URL: https://doi.org/10.1111/j.1745-3933.2011.01074.x.

Bryan, SE et al. (2013). "The impact of baryons on the spins and shapes of dark matter haloes". In: *Monthly Notices of the Royal Astronomical Society* 429.4, pp. 3316–3329.

Buote, David A et al. (2002). "Chandra evidence of a flattened, triaxial dark matter halo in the elliptical galaxy NGC 720". In: *The Astrophysical Journal* 577.1, p. 183.

Carucci, Isabella P et al. (2015). "Warm dark matter signatures on the 21cm power spectrum: intensity mapping forecasts for SKA". In: *Journal of Cosmology and Astroparticle Physics* 2015.07, p. 047.

Child, Hillary L et al. (2018). "Halo profiles and the concentration–mass relation for a ΛCDM universe". In: *The Astrophysical Journal* 859.1, p. 55.

Chua, Kun Ting Eddie et al. (2021). "The impact of galactic feedback on the shapes of dark-matter haloes". In: *arXiv preprint arXiv:2109.00012*.

Coles et al. (2003). *Cosmology: The origin and evolution of cosmic structure*. John Wiley & Sons.

Cui, Weiguang et al. (2012). "The effects of baryons on the halo mass function". In: *Monthly Notices of the Royal Astronomical Society* 423.3, pp. 2279–2287. URL: https://doi.org/10.1111/j.1365-2966.2012.21037.x.

David (2017). *Advanced Octrees 1: preliminaries, insertion strategies and maximum tree depth*. URL: https://geidav.wordpress.com/2014/07/18/advanced-octrees-1-preliminaries-insertion-strategies-and-max-tree-depth/.

Davis, Marc et al. (1985). "The evolution of large-scale structure in a universe dominated by cold dark matter". In: *The Astrophysical Journal* 292, pp. 371–394.

Dekel, Avishai and Joseph Silk (1986). "The origin of dwarf galaxies, cold dark matter, and biased galaxy formation". In: *The Astrophysical Journal* 303, pp. 39–55. URL: https://doi.org/10.1086/164050.

Despali, Giulia et al. (2019). "The interplay of self-interacting dark matter and baryons in shaping the halo evolution". In: *Monthly Notices of the Royal Astronomical Society* 484.4, pp. 4563–4573. URL: https://doi.org/10.1093/mnras/stz273.

Diamanti, Roberta et al. (2017). "Cold dark matter plus not-so-clumpy dark relics". In: *Journal of Cosmology and Astroparticle Physics* 2017.06, p. 008.

Dunstan, Robyn M et al. (2011). "The halo model of large scale structure for warm dark matter". In: *arXiv preprint arXiv:1109.6291*.

Einasto, Jaan (1965). "On the Construction of a Composite Model for the Galaxy and on the Determination of the System of Galactic Parameters". In: *Trudy Astrofizicheskogo Instituta Alma-Ata* 5, pp. 87–100.

Elbert et al. (2015a). "Core formation in dwarf haloes with self-interacting dark matter: no fine-tuning necessary". In: *Monthly Notices of the Royal Astronomical Society* 453.1, pp. 29–37. URL: https://arxiv.org/pdf/1412.1477.pdf.

— (2018). "A testable conspiracy: simulating baryonic effects on self-interacting dark matter halos". In: *The Astrophysical Journal* 853.2, p. 109.

Elbert et al. (2015b). "Core formation in dwarf haloes with self-interacting dark matter: no fine-tuning necessary". In: *Monthly Notices of the Royal Astronomical Society* 453.1, pp. 29–37. URL: https://doi.org/10.1093/mnras/stv1470.

Enzi, Wolfgang et al. (2021). "Joint constraints on thermal relic dark matter from strong gravitational lensing, the Ly α forest, and Milky Way satellites". In: *Monthly Notices of the Royal Astronomical Society* 506.4, pp. 5848–5862.

Frenk et al. (2012). "Dark matter and cosmic structure". In: *Annalen der Physik* 524.9-10, pp. 507–534. URL: https://doi.org/10.1002/andp.201200212.

Fry, A Bastidas et al. (2015). "All about baryons: revisiting SIDM predictions at small halo masses". In: *Monthly Notices of the Royal Astronomical Society* 452.2, pp. 1468–1479.

Garrison-Kimmel, Shea et al. (2014). "Too big to fail in the local group". In: *Monthly Notices of the Royal Astronomical Society* 444.1, pp. 222–236. URL: https://doi.org/10.1093/mnras/stu1477.

Gnedin, Oleg Y et al. (2004). "Response of dark matter halos to condensation of baryons: cosmological simulations and improved adiabatic contraction model". In: *The Astrophysical Journal* 616.1, p. 16. URL: https://doi.org/10.1086/424914.

Hellwing, Wojciech A et al. (2016). "The Copernicus Complexio: a high-resolution view of the small-scale Universe". In: *Monthly Notices of the Royal Astronomical Society* 457.4, pp. 3492–3509.

Hopkins, Philip F et al. (2014). "Galaxies on FIRE (Feedback In Realistic Environments): stellar feedback explains cosmologically inefficient star formation". In: *Monthly Notices of the Royal Astronomical Society* 445.1, pp. 581–603. URL: https://doi.org/10.1093/mnras/stu1738.

Kahlhoefer, Felix (2017). "Review of LHC dark matter searches". In: *International Journal of Modern Physics A* 32.13, p. 1730006. URL: https://doi.org/10.1142/S0217751X1730006X.

Kamada, Ayuki et al. (2017). "Self-interacting dark matter can explain diverse galactic rotation curves". In: *Physical review letters* 119.11, p. 111102.

Kaplinghat, Manoj et al. (2014a). "Tying dark matter to baryons with self-interactions". In: *Physical Review Letters* 113.2, p. 021302. URL: https://doi.org/10.1103/PhysRevLett.113.021302.

— (2014b). "Tying dark matter to baryons with self-interactions". In: *Physical Review Letters* 113.2, p. 021302.

Kauffmann et al. (1993). "The formation and evolution of galaxies within merging dark matter haloes". In: *Monthly Notices of the Royal Astronomical Society* 264.1, pp. 201–218. URL: https://doi.org/10.1093/mnras/264.1.201.

Klypin et al. (1999). "Where are the missing galactic satellites?" In: *The Astrophysical Journal* 522.1, p. 82. URL: https://doi.org/10.1086/307643.

Koda et al. (2011). "Gravothermal collapse of isolated self-interacting dark matter haloes: N-body simulation versus the fluid model". In: *Monthly Notices of the Royal Astronomical Society* 415.2, pp. 1125–1137. URL: https://doi.org/10.1111/j.1365-2966.2011.18684.x.

Li, Ran et al. (2017). "Projection effects in the strong lensing study of subhaloes". In: *Monthly Notices of the Royal Astronomical Society* 468.2, pp. 1426–1432.

Ludlow, Aaron D et al. (2014). "The mass–concentration–redshift relation of cold dark matter haloes". In: *Monthly Notices of the Royal Astronomical Society* 441.1, pp. 378–388. URL: https://doi.org/10.1093/mnras/stu483.

McDaniel et al. (2021). "X-ray shapes of elliptical galaxies and implications for self-interacting dark matter". In: *Journal of Cosmology and Astroparticle Physics* 2021.05, p. 020.

Meneghetti, Massimo et al. (2001). "Giant cluster arcs as a constraint on the scattering cross-section of dark matter". In: *Monthly Notices of the Royal Astronomical Society* 325.1, pp. 435–442. URL: https://doi.org/10.1046/j.1365-8711.2001.04477.x.

Miralda-Escudé, Jordi (2002). "A test of the collisional dark matter hypothesis from cluster lensing". In: *The Astrophysical Journal* 564.1, p. 60.

Moore, Ben (1994). "Evidence against dissipation-less dark matter from observations of galaxy haloes". In: *Nature* 370.6491, pp. 629–631. URL: https://doi.org/10.1038/370629a0.

Murgia et al. (2018). "Novel constraints on noncold, nonthermal dark matter from Lyman-alpha forest data". In: *Physical Review D* 98.8, p. 083540. URL: https://doi.org/10.1103/PhysRevD.98.083540.

Navarro et al. (1996). "The cores of dwarf galaxy haloes". In: *Monthly Notices of the Royal Astronomical Society* 283.3, pp. L72–L78. URL: https://doi.org/10.1093/mnras/283.3.L72.

— (1997). "A universal density profile from hierarchical clustering". In: *The Astrophysical Journal* 490.2, p. 493. URL: https://doi.org/10.1086/304888.

Newton, Oliver et al. (2021). "Constraints on the properties of warm dark matter using the satellite galaxies of the Milky Way". In: *Journal of Cosmology and Astroparticle Physics* 2021.08, p. 062. URL: https://doi.org/10.1088/1475-7516/2021/08/062.

Ocvirk, P et al. (2014). "The reionization of galactic satellite populations". In: *The Astrophysical Journal* 794.1, p. 20. URL: https://doi.org/10.1088/0004-637X/794/1/20.

Oman et al. (2015). "The unexpected diversity of dwarf galaxy rotation curves". In: *Monthly Notices of the Royal Astronomical Society* 452.4, pp. 3650–3665. URL: https://doi.org/10.1093/mnras/stv1504.

Persic, Massimo, Paolo Salucci, and Fulvio Stel (1996). "The universal rotation curve of spiral galaxies—I. The dark matter connection". In: *Monthly Notices of the Royal Astronomical Society* 281.1, pp. 27–47. URL: https://doi.org/10.1093/mnras/281.1.27.

Peter, Annika HG et al. (2013). "Cosmological simulations with self-interacting dark matter–II. Halo shapes versus observations". In: *Monthly Notices of the Royal Astronomical Society* 430.1, pp. 105–120. URL: https://doi.org/10.1093/mnras/sts535.

Postman, Marc et al. (2012). "The cluster lensing and supernova survey with Hubble: an overview". In: *The Astrophysical Journal Supplement Series* 199.2, p. 25.

Press, William H and Paul Schechter (1974). "Formation of galaxies and clusters of galaxies by self-similar gravitational condensation". In: *The Astrophysical Journal* 187, pp. 425–438. URL: https://doi.org/10.1086/152650.

Robertson (2017). "The cosmological implications of self-interacting dark matter". PhD thesis. Durham University. URL: http://etheses.dur.ac.uk/12305/.

Robertson et al. (2019). "Observable tests of self-interacting dark matter in galaxy clusters: cosmological simulations with SIDM and baryons". In: *Monthly Notices of the Royal Astronomical Society* 488.3, pp. 3646–3662. URL: https://doi.org/%2010.1093/mnras/stz1815.

Robertson et al. (2018). "The diverse density profiles of galaxy clusters with self-interacting dark matter plus baryons". In: *Monthly Notices of the Royal Astronomical Society: Letters* 476.1, pp. L20–L24. URL: https://doi.org/10.1093/mnrasl/sly024.

Robles, Victor H et al. (2017). "SIDM on FIRE: Hydrodynamical Self-Interacting Dark Matter simulations of low-mass dwarf galaxies". In: *Monthly Notices of the Royal Astronomical Society* 472.3, pp. 2945–2954. URL: https://doi.org/10.1093/mnras/stx2253.

Rocha, Miguel et al. (2013). "Cosmological simulations with self-interacting dark matter–I. Constant-density cores and substructure". In: *Monthly Notices of the Royal Astronomical Society* 430.1, pp. 81–104. URL: https://doi.org/10.1093/mnras/sts514.

Sameie, Omid et al. (2018a). "The impact of baryonic discs on the shapes and profiles of self-interacting dark matter haloes". In: *Monthly Notices of the Royal Astronomical Society* 479.1, pp. 359–367. URL: https://doi.org/10.1093/mnras/sty1516.

— (2018b). "The impact of baryonic discs on the shapes and profiles of self-interacting dark matter haloes". In: *Monthly Notices of the Royal Astronomical Society* 479.1, pp. 359–367. URL: https://doi.org/10.1093/mnras/sty1516.

Sawala, Till et al. (2016). "The APOSTLE simulations: solutions to the Local Group's cosmic puzzles". In: *Monthly Notices of the Royal Astronomical Society* 457.2, pp. 1931–1943. URL: https://doi.org/10.1093/mnras/stw145.

Sawala et al. (2013). "The abundance of (not just) dark matter haloes". In: *Monthly Notices of the Royal Astronomical Society* 431.2, pp. 1366–1382. URL: https://doi.org/10.1093/mnras/stt259.

Schaller, Matthieu et al. (June 2015). "Baryon effects on the internal structure of CDM haloes in the EAGLE simulations". In: *Monthly Notices of the Royal Astronomical Society* 451.2, pp. 1247–1267. ISSN: 0035-8711. URL: https://doi.org/10.1093/mnras/stv1067.

Schaye, Joop et al. (2015). "The EAGLE project: simulating the evolution and assembly of galaxies and their environments". In: *Monthly Notices of the Royal Astronomical Society* 446.1, pp. 521–554. URL: https://doi.org/10.1093/mnras/stu2058.

Sheth, Ravi K and Giuseppe Tormen (2002). "An excursion set model of hierarchical clustering: ellipsoidal collapse and the moving barrier". In: *Monthly Notices of the Royal Astronomical Society* 329.1, pp. 61–75. URL: https://doi.org/10.1046/j.1365-8711.2002.04950.x.

Spergel, David N and Paul J Steinhardt (2000a). "Observational evidence for self-interacting cold dark matter". In: *Physical review letters* 84.17, p. 3760. URL: https://doi.org/10.1103/PhysRevLett.84.3760.

Spergel, David N and Paul J Steinhardt (2000b). "Observational evidence for self-interacting cold dark matter". In: *Physical review letters* 84.17, p. 3760. URL: https://doi.org/10.1103/PhysRevLett.84.3760.

Springel, Volker (2005). "User guide for GADGET-2". In: *Max-Plank-Institute for Astrophysics, Garching, Germany*. URL: https://wwwmpa.mpa-garching.mpg.de/gadget/users-guide.pdf.

Tegmark, Max et al. (2004). "The three-dimensional power spectrum of galaxies from the sloan digital sky survey". In: *The Astrophysical Journal* 606.2, p. 702. URL: https://doi.org/10.1086/382125.

Thoul, Anne A and David H Weinberg (1995). "Hydrodynamic Simulations of Galaxy Formation. II. Photoionization and the Formation of Low Mass Galaxies". In: *arXiv preprint astro-ph/9510154*. URL: https://doi.org/10.1086/177446.

Trujillo-Gomez, Sebastian et al. (2015). "Low-mass galaxy assembly in simulations: regulation of early star formation by radiation from massive stars". In: *Monthly Notices of the Royal Astronomical Society* 446.2, pp. 1140–1162.

Tulin, Sean and Hai-Bo Yu (2018). "Dark matter self-interactions and small scale structure". In: *Physics Reports* 730, pp. 1–57. URL: https://doi.org/10.1016/j.physrep.2017.11.004.

Vegetti, Simona and Léon VE Koopmans (2009). "Bayesian strong gravitational-lens modelling on adaptive grids: objective detection of mass substructure in Galaxies". In: *Monthly Notices of the Royal Astronomical Society* 392.3, pp. 945–963. URL: https://doi.org/10.1111/j.1365-2966.2008.14005.x.

Vogelsberger et al. (2012). "Subhaloes in self-interacting galactic dark matter haloes". In: *Monthly Notices of the Royal Astronomical Society* 423.4, pp. 3740–3752.

— (2016). "ETHOS–an effective theory of structure formation: dark matter physics as a possible explanation of the small-scale CDM problems". In: *Monthly Notices of the Royal Astronomical Society* 460.2, pp. 1399–1416.

Vogelsberger, Mark and Jesus Zavala (2013). "Direct detection of self-interacting dark matter". In: *Monthly Notices of the Royal Astronomical Society* 430.3, pp. 1722–1735. URL: https://doi.org/10.1093/mnras/sts712.

Vogelsberger et al. (Aug. 2014). "Introducing the Illustris Project: simulating the coevolution of dark and visible matter in the Universe". In: *Monthly Notices of the Royal Astronomical Society* 444.2, pp. 1518–1547. ISSN: 0035-8711. URL: https://doi.org/10.1093/mnras/stu1536.

White, Martin (2001). "The mass of a halo". In: *Astronomy & Astrophysics* 367.1, pp. 27–32. URL: https://doi.org/10.1051/0004-6361:20000357.

Yoshida, Naoki et al. (2000). "Weakly self-interacting dark matter and the structure of dark halos". In: *The Astrophysical Journal Letters* 544.2, p. L87. URL: https://doi.org/10.1086/317306.

Zavala et al. (2013). “Constraining self-interacting dark matter with the Milky Way’s dwarf spheroidals”. In: *Monthly Notices of the Royal Astronomical Society: Letters* 431.1, pp. L20–L24. URL: https://doi.org/10.1093/mnrasl/sls053.

Zavala, Jesús and Carlos S Frenk (2019). “Dark matter haloes and subhaloes”. In: *Galaxies* 7.4, p. 81.

Zeldovich, Ya B (1972). “A hypothesis, unifying the structure and the entropy of the Universe”. In: *Monthly Notices of the Royal Astronomical Society* 160.1, 1P–3P.

Zwicky, Fritz (1933). “Die rotverschiebung von extragalaktischen nebeln”. In: *Helvetica physica acta* 6, pp. 110–127.